This thesis was supervised by Prof. Pere Colet and Dr. Damià Gomilla at the Institute for Cross-Disciplinary Physics and Complex Systems and Universitat de les Illes Balears. In Palma de Mallorca, between 2004 and 2009.

Aquesta tesi va a ser dirigida pel Prof. Pere Colet i el Dr. Damià Gomilla al Institut de Fìsica Interdisciplinària i Sistemes Complexos i a la Universitat de les Illes Balears. A Palma de Mallorca, entre 2004 and 2009.

A. Jacobo
Spatial structures and Information Processing in Nonlinear Optical Cavities

PhD Thesis

Spatial structures and Information Processing in Nonlinear Optical Cavities

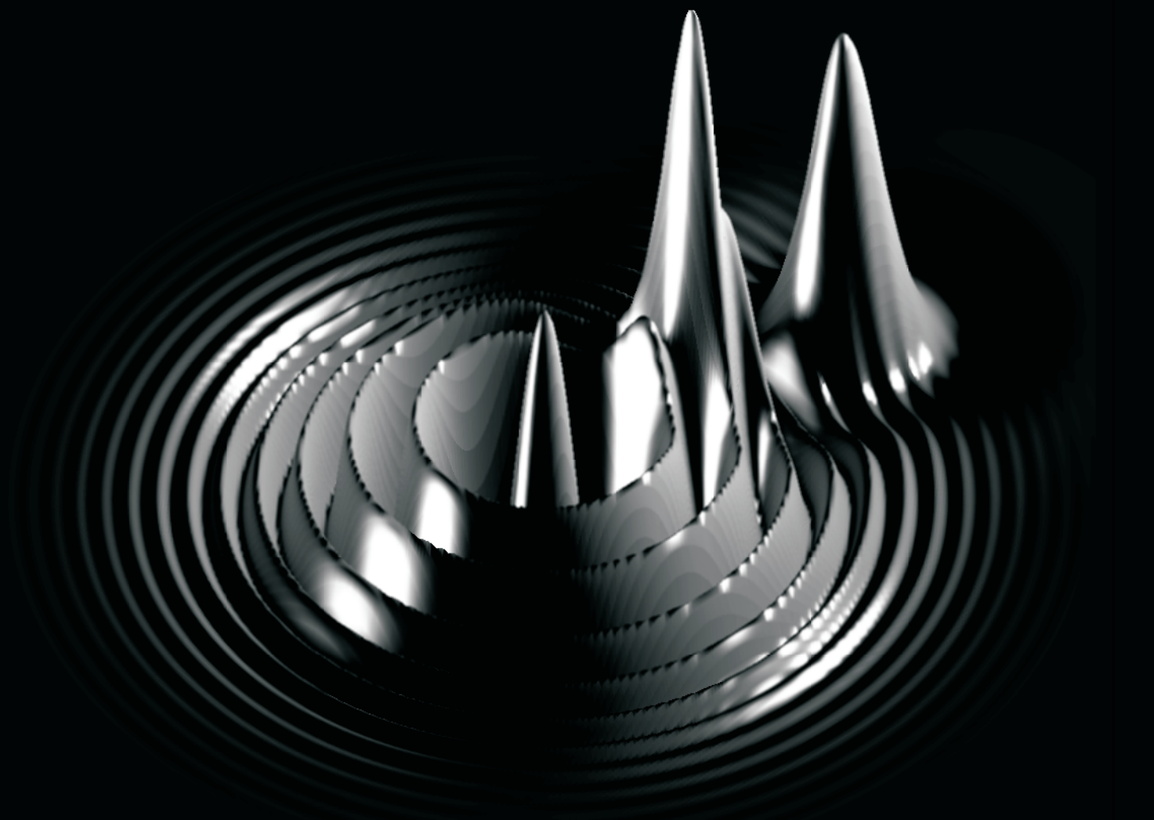

Adrian Jacobo

TESI DOCTORAL

Spatial structures and Information Processing in Nonlinear Optical Cavities

Tesi presentada per Adrian Jacobo, al Departament de Física de la Universitat de les Illes Balears, per optar al grau de Doctor en Física

Adrian Jacobo

Palma de Mallorca, February 2008

Spatial structures and Information Processing in Nonlinear Optical Cavities

Adrian Jacobo
Instituto de Fisica Interdisciplinar y Sistemas Complejos
IFISC (UIB-CSIC)

PhD Thesis

Directors: Prof. Pere Colet and Dr. Damià Gomila

This document was typeset with LaTeX 2_ε

Pere Colet Rafecas, Profesor de Investigació del Consejo Superior de Investigaciones Científicas, y Damià Gomila Contratat Doctor I3P

CERTIFICA

que aquesta tesi doctoral ha estat realitzada pel Sr. *Adrian Jacobo* sota la seva direcciò a l'Instituto de Fisica Interdisciplinar y Sistemas Complejos i, per a què consti, firma la present

a Palma de Mallorca, 5 de Febrer de 2008

Pere Colet Rafecas Damià Gomila

"We must not forget that when radium was discovered no one knew that it would prove useful in hospitals. The work was one of pure science. And this is a proof that scientific work must not be considered from the point of view of the direct usefulness of it. It must be done for itself, for the beauty of science, and then there is always the chance that a scientific discovery may become like the radium a benefit for humanity." — Marie Curie

Acknowledgments

Esta tesis fué realizada en el Instituto de Fisica Interdisciplinar y Sistemas Complejos (IFISC, CSIC-UIB) y financiada por una beca FPU del Ministerio de Ciencia e Innovación.

En primer lugar quisiera agradecer al Prof. Pere Colet por haberme dado la oportunidad de realizar esta tesis, por todo el tiempo dedicado y también por su amabilidad y su interés permanente en que las cosas fueran bien tanto en el plano académico como humano. Gracias también al Dr. Damià Gomila, codirector de esta tesis, que con su llegada le aportó nuevas ideas a este trabajo y de quien aprendí muchas cosas, además de haber encontrado en él un amigo. Y al Prof. Manuel Matías por su colaboración en los artículos que componen la segunda parte de esta tesis, por su entera disposición y amabilidad y las enriquecedoras charlas que contribuyeron a mi formación.

Además quisiera agradecer a la Dr^{a}. Roberta Zambrini por haberme ayudado con la introducción de esta tesis y a la Dr^{a}. Lucía Loureiro Porto por su ayuda con la corrección de la misma.

Quisiera tambíen mencionar al Prof. Emilio Hernandez García por su colaboración en el Capítulo 3 de esta tesis. Y al Prof. Claudio Mirasso y el Dr. Miguel Cornelles por su colaboración en el Capítulo 4. También quisiera agradecer a todos los investigadores y miembros del IFISC, por su ayuda y por crear un ambiente de trabajo cordial y motivador.

I would like to thank also to Prof. Giampaolo D' Alessandro for his invaluable lessons and for his hospitality during my stay in University of Southampton. I regret that the results of those stays couldn't make it to become part of this thesis,

mainly for time reasons, but I hope that we can continue working on them in the future.

En el plano personal, quisiera agradecer a mi familia y amigos en Argentina, a quienes siempre extraño y tengo presentes, por haber sabido llevar la distancia y por haberme apoyado incondicionalmente cuando tome la decisión de venir aquí. Y también a los amigos que conocí durante mis cuatro años de estadía en Palma, especialmente a aquellos a quienes considero mi segunda familia.

Finalmente, un agradecimiento muy especial a Laura, por todo su apoyo incluso en los momentos difíciles y por haber elegido compartir su vida conmigo.

Contents

Chapter 1

Introduction

Nonlinear optics is the study of phenomena that occur as a consequence of the modification of the optical properties of a material by the presence of light. Such nonlinear effects usually occur with high intensities of light, that can only be achieved with lasers. In fact, the beginning of nonlinear optics is often considered to be the experiment of Second Harmonic Generation by Franken and coworkers in 1961, shortly after the demonstration of the first working laser by Maiman in 1960.

To enhance the interaction between the light and the nonlinear material, it is usually placed inside an optical cavity. This nonlinear optical cavities exhibit various kinds of interesting phenomena such as bistability, pattern formation, localized structures (also called cavity solitons) and chaos. The study of some of those effects in nonlinear optical cavities and its possible application to information processing is the main topic of this thesis. We will focus in two different types of nonlinear optical systems: the *Second Harmonic Generation* and the *Kerr cavity*, which constitute two of the most relevant nonlinear optical systems. Thus, in Sections 1.6 and 1.7 respectively, we will derive the equations that describe this two systems.

In the first part of the thesis we will give an introduction to the most relevant concepts that we will encounter along the rest of the thesis. We will first give a brief introduction to the subject of *image processing* which is then studied in relation with the process of second harmonic generation in Chapter 2. One of this image processing operations is the enhancement of an image's contrast, this procedure is based in the bistability displayed by the equations for the Second Harmonic Generation process. In Chapter 3 we will introduce a technique based on the contrast enhancement process, and use it to filter data from ecological

time series and detect changes on its mean value. Therefore, in Sec. 1.2 we will give a brief summary of methods available in the literature to detect such changes. In Chapter 4 we will apply the same filtering method to decode chaos encrypted messages.

In Sec. 1.3 we will introduce the concept of *localized structures* which is the main topic of Part II. There we will study the dynamics of localized structures in a Kerr cavity. In particular, in Chapters 5, 6 and 8 we will study the bifurcations that give rise to the different dynamical behaviors displayed by these structures. That is why, in Sect. 1.4 we give a brief summary of the bifurcations that we will encounter, and its main properties.

The most interesting dynamical behavior of these localized structures is *excitability*, this concept will be introduced in Sect. 5.4. Once we have characterized the excitable localized structures we will show, in Chapter 7, how they can be used to construct logic gates by coupling several of them. This gates perform basic logic operations and constitute the primary units of information processing, as they can be coupled to perform more complicated operations.

In Chapter 8 we will study oscillatory localized structures. In particular we will focus in the study of the interaction of such structures as a model of interacting nonlocal oscillators.

Finally in Chapter 9 we will summarize the obtained results, and give some concluding remarks.

1.1 Image processing

An image is a representation of a real-world scene, described by two a two dimensional field. This field is a scalar in the case of gray scale images, or a vector (usually of three components) for color images.

Image processing is any form of information processing for which the input is an image, such as photographs or frames of video, and the output is usually the same image with some of its properties altered, or some of its features enhanced. From a more general point of view, the output of an image processing technique is not necessarily an image, but can be for instance a set of features of the image. This type of image processing is also called image analysis. In short, we can say that image processing is an operation done over the image with the objective of restoring, enhancing or understanding it.

The amount of image processing operations is very large, and grows every day. Without trying to give a comprehensive list we cite some of them as an example, some of which are illustrated in Fig. 1.1:

- Geometric transformations such as enlargement, reduction, and rotation.
- Color corrections such as brightness and contrast adjustments, quantization, or conversion to a different color space.
- Combination of two or more images, e.g. into an average, blend, difference, or image composite
- Visual effects such as edge enhancement, embossing, sharpening, noise addition or substraction, blurring or focusing, etc.
- Segmentation of the image into regions.
- Extending dynamic range by combining differently exposed images.
- Image restoration to increase the quality of a digital image, such as deconvolution to reduce blur, restoration of faded color, removal of scratches, etc.

Most image processing techniques involve treating the image as a two dimensional signal and applying standard signal-processing techniques to it [2]. This techniques usually consist of applying some computational algorithms to the image. The first image processing algorithms were developed many years ago, and its complexity and versatility is always increasing as more computational power is available. The list of image processing software is endless and we can cite as an example Adobe Photoshop [3], Corel Paint Shop Pro [1], VIPS [4], Gimp [5], ImageMagick [6], etc.

Far from being a closed field, the research on new image processing techniques is very active and there are hundreds of conferences, workshops and congresses every year covering several topics. Some of the major conferences are the "International Congress on Image and Signal Processing" [7], "IEEE International Conference on Image Processing" [8], "European Conference on Computer Vision" [9], "International Conference on Pattern Recognition" [10], "IEEE Conference on Computer Vision and Pattern Recognition" [11], etc.

In the 60's, another type of image processing techniques started to develop. This approach consists of the use of Partial Differential Equations (PDE's) for image processing. In this scheme, the image to be treated is used as the initial condition of a partial differential equation with x, y and t as variables, and letting the equation evolve for some time [13].

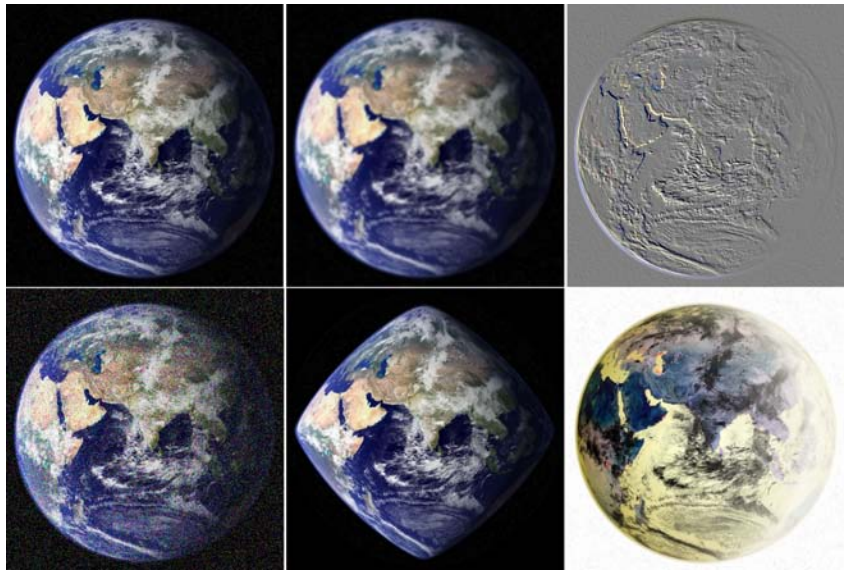

Figure 1.1: Several examples of processed images. From left to right, top to bottom: Original image, blurred image, embossed image, image with added noise, geometric transformation over the original image, negative of the original image. Image created using Paint Shop Pro software [1].

An example of such an approach is the use of the heat equation

$$\frac{\partial u}{\partial t} = \nabla^2 u \tag{1.1}$$

to smooth or denoise images. By letting evolve some image as the initial condition of this equation the image is more and more blurred (Fig. 1.2). The opposite effect can be achieved by using the same equation with the time reversed i.e

$$\frac{\partial u}{\partial t} = -\nabla^2 u \tag{1.2}$$

Applying this equation, an image can be deblurred to some extent until the intrinsic instabilities of the method start to act.

This smoothing process obtained with Eq. (1.1) is isotropic, i.e. it smooths with equal strength in all spatial directions. This means that edges in the image will soon become blurred. The introduction of nonlinear PDE's allows to obtain dif-

Figure 1.2: Progressive smoothing of an image using the heat equation. From left to right time is further increased in the equation (After [12]).

Figure 1.3: Progressive smoothing of an image using Eq. (1.3). From left to right time is further increased in the equation (After [12]).

ferent processing possibilities and to overcome the limitation of linear methods. An example is the anisotropic filtering obtained applying the equation:

$$\frac{\partial u}{\partial t} = \nabla \cdot \left(\frac{\nabla^2 u}{|\nabla^2 u|} \right) \tag{1.3}$$

In this case, the edges in the image are well preserved for a long time, regions gradually merge with each other, and the intermediate images take on a segmentation-like appearance, as can be seen in Fig. 1.3.

A step further beyond linear PDE's was the pioneering work of Perona and Malik [14], in the early 90's, on anisotropic diffusion. A wide variety of processing effects using nonlinear PDE's have been introduced, not only limited to image blurring and deblurring but for noise filtering, edge and shape recognition, image segmentation, etc [15–17].

The algorithm-based techniques of image processing are digital techniques. This means that the processed image is a digital representation of some real world scene or image. This digital representation consist of set of points or *pixels* that form the image, which are stored in a matrix. PDE based techniques can be also applied to the digital representation of an image, by numerically integrating the

PDE using a computer. But for PDE techniques there is also the possibility to represent the image using a continuous physical field which avoids pixelation. Therefore, in principle, it is possible to apply it to the field the dynamics described by the PDE, and do the processing without need of digitalization or a computer.

The idea of avoiding pixelation is also behind all-optical image processing, but instead of using an arbitrary PDE, we consider one describing a real optical device. The image is represented in the transverse plane of a light beam and processed by means of the interaction of light with different elements.

All optical image processing methods have been around since the '50s [18], always closely related with all-optical computing methods. Optical computing developed as a very broad subject that comprehends pattern recognition [19], acousto optic signal processing [20], optical neural networks [21], optical switching [22], etc. In the field of all optical image processing, a large amount of work has been performed in photorefractive media [23], including edge enhancement [24–26], image inversion, division, differentiation, and deblurring, [27–30], noise suppression [31], and contrast enhancement [32].

Although image processing by all-optical methods is by far less common than its digital counterpart, it provides some interesting advantages. As previously discussed, in order for an image to be processed by digital means, first it has to be digitized by means of an array of photodetectors. In an all-optical scheme this step is avoided or postponed to the end of the information processing chain, reducing possible errors to imperfect calibration of photodetectors and subsequent electronic transmission. An additional advantage is that the maximal resolution achievable is limited by diffraction, and not by the number of pixels in the detector. Finally, an all-optical processor takes advantage of the intrinsic parallelism of optics.

As previously stated, many all-optical processing methods can be computer simulated. This simulation is usually done by integrating a PDE that describes the all optical device. Therefore, PDE methods and all optical methods are closely related and work as inspiration for each other. The work presented in Chapter 2 lies in the zone between PDE methods and all-optical methods, since we propose an all optical scheme for image processing by writing the PDE's that describe the system and integrating them.

The proposed processing scheme is sketched in Fig. 1.4: the image is inserted in an optical cavity filled with a nonlinear medium. Inside the cavity, the image processing occurs because of the interaction of the light with the nonlinear medium. Finally the processed image is obtained at the output of the cavity.

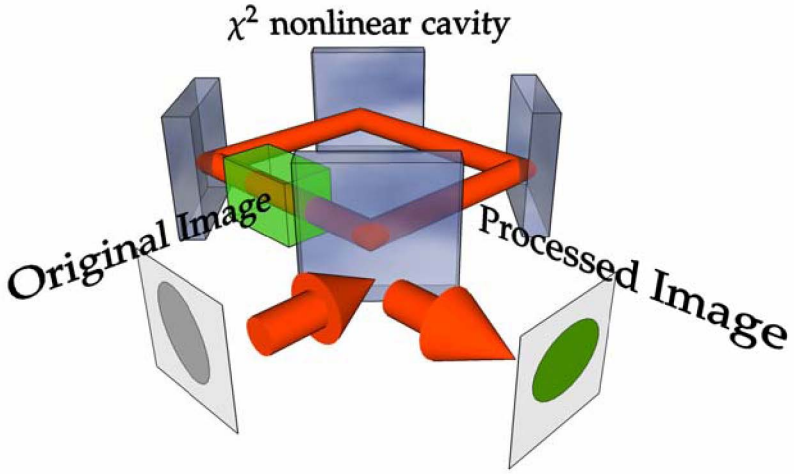

Figure 1.4: Sketch of the image processing scheme. The image is inserted in a cavity filled with a nonlinear medium and processed inside it.

Traditional all-optical processing techniques consist of light propagating trough some medium or device. The difference with the system studied in Chapter 2 is that we use a nonlinear optical cavity which introduces a nonlinear treatment of the image along with the possibility to tune the processing effects by means of the control of the thresholds introduced by the cavity.

1.2 Detection of change points in time series

The analysis of time series is a very active topic of mathematics, with a broad spectrum of applications ranging from astronomy [33] to social sciences [34] passing through economy [35], medicine [36], etc. Among the different aspects that can be analyzed, in many cases, it is particularly important to detect points in which there is a sudden change in some property of the series. These points are called *change points* and methods to detect them are widely used in climatology [37] and ecology [38] among other areas.

In the context of ecology, those changes represent regime shifts [39] in the ecosystem and can have profound implications for the life of the species in it. Change

points may indicate the presence of an ecological threshold. An ecological threshold refer to the forcing that a driver can maximally exert on a given resource while maintaining acceptable levels of environmental quality. When such thresholds are exceeded, the resources, services or functions may suddenly shift status at a change point. Examples include excessive algal growth, reproductive failures of organisms and depleted fish stocks. These new states cannot easily be reverted to acceptable levels. In some cases the changes are practically irreversible. When a system reaches such state the change point is called *point of no return*. Points of no return are critical for sustainable policies. Such points have been observed in shifts from macrophyteto plankton-dominated coastal ecosystems, and in shifts from oxic to anoxic conditions following increased organic inputs to coastal sediments.

Sometimes change points cannot be detected by measuring relevant variables of an ecosystem until the change becomes very evident and the system is endangered. This is because this changes can be masked by the noise in the measured variables. Therefore, there is a growing interest in developing methods to detect change points from the time series of the relevant variables of an ecosystem. The interest in this field has motivated the creation of the European Project *Thresholds* [40] which has, as one of its objectives, the development of new methods of detection of change points.

A change point can be determined by changes in the mean value of the time series, its variance, power spectrum, or other properties. The changes in the mean value are the most relevant and studied case. There are many methods described in the literature to detect such changes, some of them are [41]:

- Parametric methods, such as the classical t-test [37, 42, 43].
- Non-parametric methods, such as the Mann-Whitney U-test [44], Wilcoxon rank sum [37, 45], or Mann-Kendall test [46, 47].
- Curve-fitting methods
- Bayesian analysis and its variations [48, 49], such as the Markov chain Monte Carlo method [50]
- Regression-based methods [51–54]
- Cumulative sum (CUSUM) methods [43, 55, 56]
- Sequential methods [37, 47]

For example, in Fig. 1.5 we illustrate the application of the method described in Ref. [43]. This algorithm is based on the sequential application of the Student's

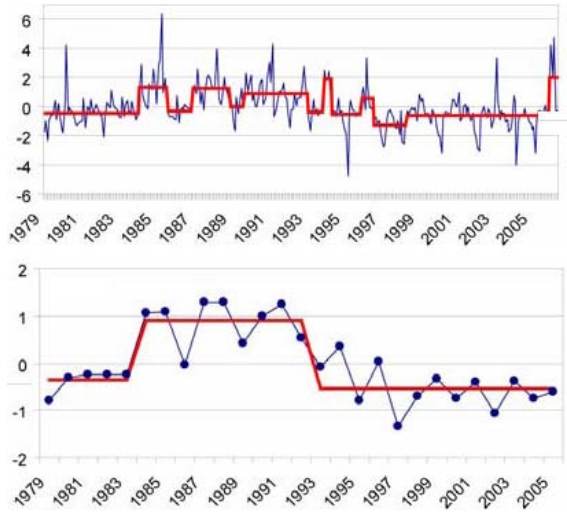

Figure 1.5: Sequential t-test change point detection method [43] applied to monthly (left panel) and annually averaged (right panel) anomalies in the dissolved inorganic nitrogen in the Baltic Sea (Ref. [57]).

t-test on a sliding window of length L. A new observation x_i is compared to the mean of the last L observations $\bar{x}_{i,L}$ using the average standard error S_L of all L step periods in the whole data sets as scaling factor. In other words, the method assumes that the change on the time series occurs in the mean value, while the variance stays constant. If the scaled difference $(x_i - \bar{x}_{i,L})/S_L)$ is within the $(1-p)$% confidence limits of a t distribution with $2(L-1)$ degrees of freedom, then this is taken as indication that no regime shift happened at time i, and the sliding widow is advanced to time $i+1$. If the value x_i fails the t-test at rejection probability p, then the point is marked as a potential change point and subsequent data are used to reject or accept the hypothesis.

All of the previously indicated methods present advantages and disadvantages. Some, like the parametric and non-parametric methods have a strong theoretical basis but many of them require to make assumptions over the data (e.g. the probability distribution of noise). This makes them sometimes hard to use, and in most of the cases is necessary to have information on the origin of the data and on how it was acquired. Some methods are only able to detect a single change point or require that the change points are separated by many data points to be detected.

In Chapter 3 we will introduce a different method to detect change points in the mean value of a time series, based on the use of a partial differential equation. This method was inspired by the one for image processing in nonlinear optical cavities described in Sec. 1.1 and studied in Chapter 2. The image processing scheme is capable of detecting sudden jumps in the intensity of an image and enhance its contrast. To simplify its application to ecological data we use the Ginzburg Landau equation which is probably the simplest PDE that provides those contrast enhancement properties. While our method does not have the strong theoretical basis of some of the other methods, it has the advantage that is easy to use and does not require additional information on the data.

In Chapter 4 we will show how this same method can be applied to the decoding of chaos encrypted messages. The encoding of messages using chaos is a technique that have become very popular in the past decade. In some chaos encoding schemes the message is codified in such a way that the mean value of the carrier with the message is different for bits “0" and bits “1". One can interpret that going from bit “0" to bit “1" is a change point which is masked by the chaotic carrier. Therefore, we can apply our detection method in this case. Furthermore, to solve this drawback, we will introduce a new message encoding scheme for which the mean value of the chaotic carrier plus the message is constant.

1.3 Localized Structures

Localized Structures (LS), or dissipative solitons, are states in extended media that consist of one (or more) regions in one state surrounded by a region in a qualitatively different state (from now onwards this *surrounding* state is an area in a stable stationary state). These structures were first suggested in Refs. [58, 59] and then described in a variety of systems, such as chemical reactions [60], semiconductors [61], granular media [62], binary-fluid convection [63, 64], vegetation patterns [65], and also in nonlinear optical cavities where they are usually referred to as Cavity Solitons (CS) [66–71] (see Ref. [72–74] for recent surveys) (Fig. 1.6).

Owing to the property of localized structures of remaining stable in a system once they are created, their potential for optical storage and information processing has been stressed [75]. Other applications, like the realization of an optical delay line combining LS and phase gradients [76] or the mapping of inhomogeneities in photonic devices [77] have been shown. In Chapter 7 we will show

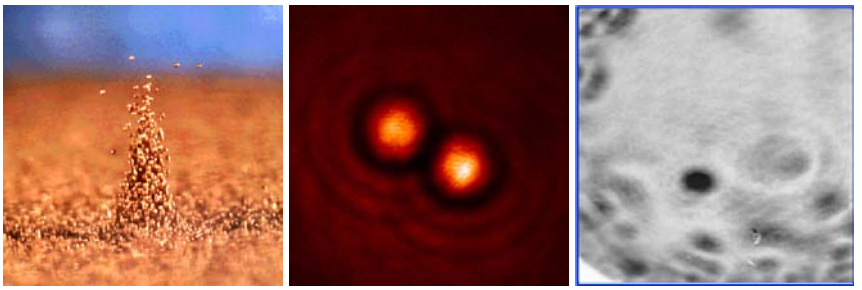

Figure 1.6: Localized structures in several experimental setups. From left to right: oscillon in a vibrated layer of sand (Ref. [62]), soliton in sodium metal vapor (Ref. [71]) and soliton in a Vertical Cavity Emitting Laser (Ref. [69]).

how dynamical properties of LS can also allow for new possible applications in information processing.

There are several mechanisms that allow for the existence of LS, one of such mechanisms is the appearance of LS as a single spot of a localized pattern. In a system which presents a subcritical pattern there is a parameter region in which this pattern coexists with the homogeneous solution (Figs. 1.7 and 1.8). For instance, this is the most common situation when, in a system with two spatial dimensions (2D), the arising patterns are hexagons. In this region, LS may appear as a single spot of the localized pattern on top of the homogeneous background [68, 78–80] (Fig. 1.7). The appearance of LS through this mechanism was first reported in a Swift-Hohenberg equation in the weak dispersion limit [81], and were also found in the degenerate [82–84] and non degenerate [85] models for Optical Parametric Oscillator and the self-focusing Kerr Cavity [86] (this is the type of LS that will be studied in Part II). Experimentally localized structures arising through this mechanism have been observed in sodium vapor with single feedback mirror [71], semiconductor lasers [61], fluids [87], granular media [62] and chemical reactions [88]. This kind of LS, that appear as a single spot of a subcritical pattern have been described by means of generic Ginzburg-Landau [89] and Swift-Hogenberg [90] models.

A sufficient condition for existence of this type of LS in a system with one spatial dimension (1D) is based on the existence of a stable stationary front between a stable homogeneous solution and a stable periodic pattern [92]. Localized structures formed by one to infinite pattern cells exist around the boundaries of the region of existence of the stationary fronts in parameter space. A 1D system

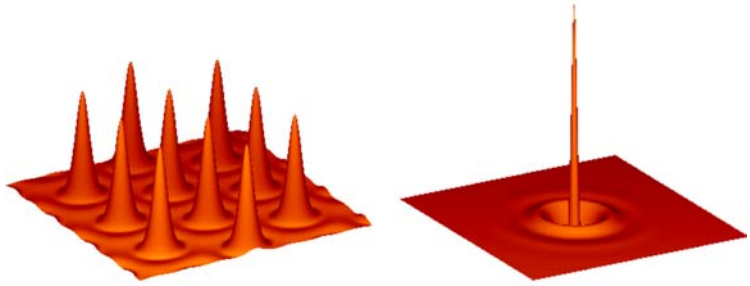

Figure 1.7: Left: Hexagonal pattern in a Kerr cavity (After [91]). Right: Localized structure in a Kerr cavity.

described by a PDE can be described as an ordinary differential equation if we only consider the stationary solutions. In this context, Localized structures can be understood as heteroclinic orbits connecting the homogeneous and pattern solutions. Despite the demonstration is, strictly speaking, valid for 1D systems, this phenomena is also observed in 2D systems with cellular patterns.

Another possibility for the existence of LS both in one and two dimensions, is that in systems in which two homogeneous states coexist (Fig. 1.9). In this case the LS appear as a domain of one of the homogeneous steady state coexisting with a background of the other. These two states are connected by fronts, if the fronts are non monotonous the interaction between its tails can lead to pinning, that stabilizes the LS [93–96]. In two dimensional systems this domain walls can be also stabilized by curvature nonlinear dynamics [97].

In general, LS may develop a number of instabilities like start moving, breathing, or oscillating. In the latter case, they would oscillate in time while remaining stationary in space, like the oscillons (oscillating localized structures) found in a vibrated layer of sand [62] (Fig. 1.6). The occurrence of these oscillons in autonomous systems has been reported both in optical [98, 99] and chemical systems [100].

In particular, LS in Kerr cavities can become unstable leading to an oscillatory regime, and further instabilities can make LS become excitable. This type of dynamical behavior will be the subject of study in Chapters 5 and 6. Once the

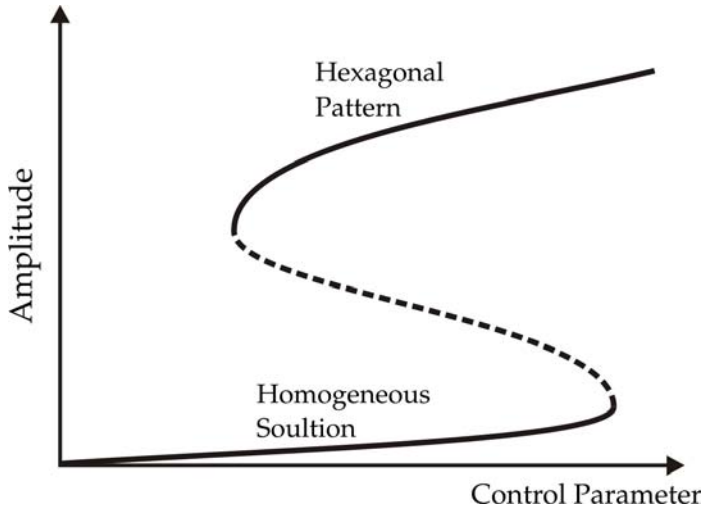

Figure 1.8: Schematic bifurcation diagram of a system with a homogeneous state coexisting with a hexagonal pattern.

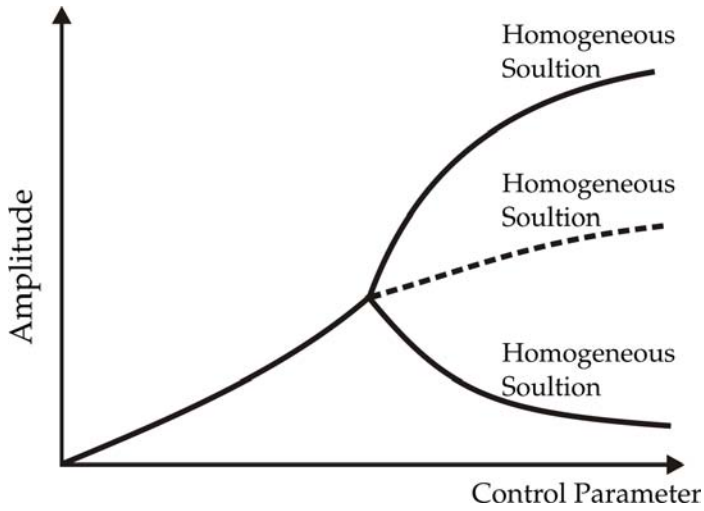

Figure 1.9: Schematic bifurcation diagram of a system with two coexisting stable homogeneous states.

main properties of this excitable behavior are shown we will study, in Chapter 7 how this excitable localized structures can be used to process information.

Moreover, the oscillatory localized structures constitute an interesting model of a nonlocal oscillator. The properties and interaction of such oscillators have not been widely studied in the literature; therefore, in Chapter 8, we present some of the most important features of these phenomena. We will find that the interacting LS present new behaviors that are not found for nonextended oscillators.

1.4 Bifurcations

Bifurcations are qualitative changes in the dynamics of a system as its parameters are varied, and the parameter values at which they occur are called bifurcation points. Bifurcations can be classified in two categories: if the bifurcation is caused only by changes in the local stability properties of fixed points, periodic orbits or other invariant sets, it is called a *local* bifurcation. If, instead, the bifurcation occurs when invariant sets of the system collide with each other the bifurcation is called *global* (excluding the collision of two fixed points, which is a local bifurcation). Global bifurcations can not be detected purely by a stability analysis of the equilibria.

Another important classification of bifurcations is based on its codimension. This term refers to the number of parameters that need to be tuned to reach the bifurcation. If the bifurcation can be reached by tuning only one parameter it receives the name of *codimension-1*, if the tuning of two parameters is needed then the bifurcation is called of *codimension-2*.

In the remainder of this chapter we will do a brief review of the codimension-1 bifurcations and some of the codimension-2 bifurcations that we will find in Chapters 5 and 6 in our study of the dynamics of localized structures. This does not pretend to be an extensive review on the subject but only a reference for the reader, as an aid for the reading of those chapters. The study of bifurcations is a widespread subject on the literature of dynamical systems, and we refer the reader to Refs. [101–103] for a deeper treatment of the subject.

1.4.1 Codimension-1 Bifurcations

Saddle-Node Bifurcation

The saddle-node bifurcation is the basic mechanism by which fixed points are created and destroyed. As a parameter is varied, two fixed points collide and mutually annihilate.

The normal form of this bifurcation is

$$\dot{x} = r + x^2 \tag{1.4}$$

where $\dot{x}$ is the derivative of x respect to the independent variable t, and r is the control parameter. If r is negative there are two fixed points, a stable one at $x = -\sqrt{-r}$ and an unstable one at $x = \sqrt{-r}$ (see Figure 1.10).

Here we say that the bifurcation occurs at $r = 0$: at this point the two fixed points that exist for $r < 0$ annihilate each other and therefore the phase space for $r < 0$ and $r > 0$ is qualitatively different. This situation can be also illustrated by the *bifurcation diagram* of the system, as shown in Figure 1.11. In this diagram we show the stationary solutions of the system ($\dot{x} = 0$, i.e. $r = -x^2$), as a function of the control parameter r.

A linear stability analysis of the stationary fixed points shows that the eigenvalue of this solution becomes 0 at the bifurcation point [*]. Therefore the linearization around the fixed point vanishes and the decay of solutions to the equilibrium is slower than an exponential decay. This is called *critical slowing down* (in analogy

[*]In this case, since we considered here the normal form of the system, which is one dimensional, there is only one eigenvalue.

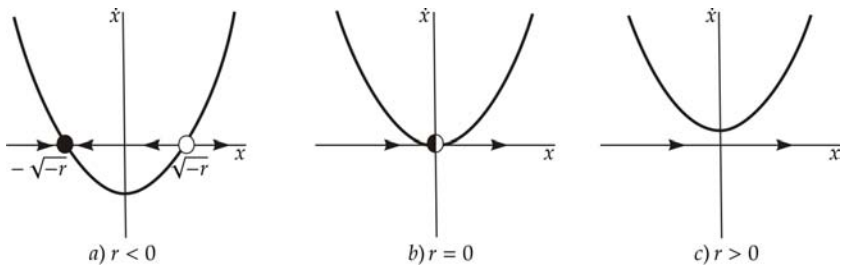

Figure 1.10: Phase space for a saddle-node bifurcation.

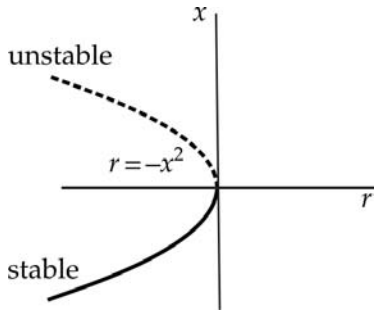

Figure 1.11: Bifurcation diagram for a saddle-node bifurcation. The filled circle corresponds to a stationary fixed point, while the empty circle is a unstable fixed point.

to critical points in equilibrium and nonequilibrium statistical mechanics as these also exhibit critical slowing down) and is a shared feature of all the local bifurcations, since in all of them there is an eigenvalue (or its real part) that becomes 0.

It is also important to note that here we only consider the one dimensional case of the bifurcation. In this case the only possibility for the bifurcation to occur is that a stable fixed point collides with a unstable one. In more than one dimension the unstable fixed point is generically a saddle, this is why this bifurcation gets its name. This bifurcation can also occur between two saddles provided that a stable direction of one of the saddles coincides with an unstable direction of the other.

Transcritical Bifurcation

In the transcritical bifurcation two fixed points collide, but, unlike the saddle-node bifurcation they do not mutually annihilate. Instead, they exchange their stability. The normal form for a transcritical bifurcation is

$$\dot{x} = rx - x^2 \tag{1.5}$$

In Fig. 1.12 we show the phase space as r varies. Here it can be seen that there is always at least one fixed point in the system and that the stability of the fixed points at $r < 0$ is exchanged for $r > 0$. As in the saddle-node bifurcation, here there is also an eigenvalue of the system that becomes 0 for $r = 0$.

If we look now at the bifurcation diagram (Fig. 1.13) we see that for $r < 0$ there are two fixed points in the system, for $x = 0$ and $x = r$. These two fixed points converge at $r = 0$ and then exchange the stability for $r > 0$.

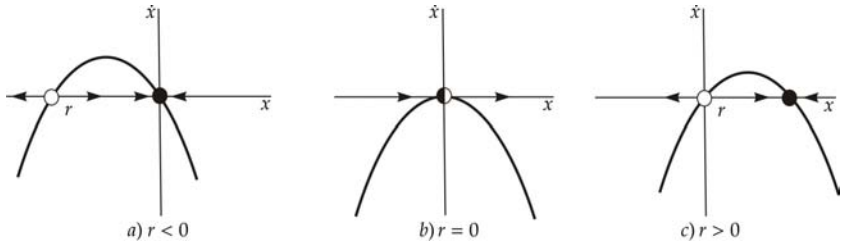

Figure 1.12: Phase space for a transcritical bifurcation.

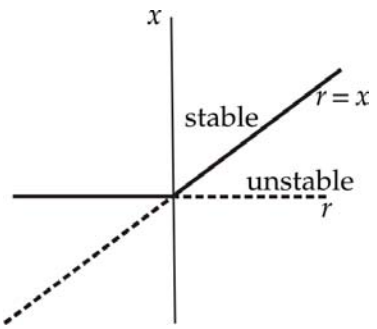

Figure 1.13: Bifurcation diagram for a transcritical bifurcation.

Pitchfork Bifurcation

This bifurcation appears in problems that have a certain symmetry. For example, in problems with parity (eg. spatial symmetry between left and right). In such cases, fixed points tend to appear and disappear in symmetrical pairs and, as in the previous two bifurcations, there is an eigenvalue of the solution that becomes 0 at the bifurcation point.

The pitchfork bifurcations can occur in two different ways, supercritical and subcritical.

- **Supercritical Pitchfork Bifurcation**

In this case, a stable fixed point gives rise to an unstable fixed point and a symmetrical pair of stable solutions, as shown in Fig. 1.14. The normal form of this bifurcation is

$$\dot{x} = rx - x^3 \tag{1.6}$$

Note that this normal form is symmetric under changes $x \to -x$, this is the parity (left-right symmetry) that we mentioned before.

Then, for $r > 0$ there are three fixed points, one at $x = 0$ that now is unstable, and two stable fixed points at $x = \pm\sqrt{r}$. This is illustrated in Fig. 1.15, where becomes obvious why this bifurcation receives its name.

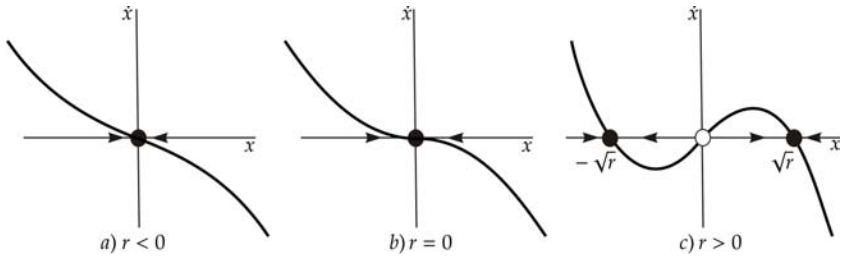

Figure 1.14: Phase space for a supercritical pitchfork bifurcation.

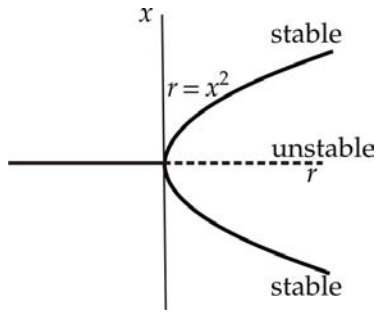

Figure 1.15: Bifurcation diagram for a supercritical pitchfork bifurcation.

- **Subcritical Pitchfork Bifurcation**

The normal form of the subcritical pitchfork bifurcation is similar to that of the supercritical case, but with the opposite sign for the nonlinear term,

$$\dot{x} = rx + x^3 \tag{1.7}$$

This term has now a *destabilizing* effect. For $r < 0$ there are two unstable fixed points at $x = \pm\sqrt{r}$ and a stable fixed point at $x = 0$ (Fig. 1.16). For $r = 0$ the linearization also vanishes in this case, and for $r > 0$ there is only a fixed point at $r = 0$, which is stable. The existence of the two unstable fixed points for $r < 0$ motivates the name "subcritical" of the bifurcation.

In Fig. 1.17 we show the bifurcation diagram where it can be seen that it is the mirror image of the one for the supercritical case, with the stability of the lines exchanged.

In real physical systems the instability introduced by the positive x^3 term is usually stabilized by higher order nonlinearities.

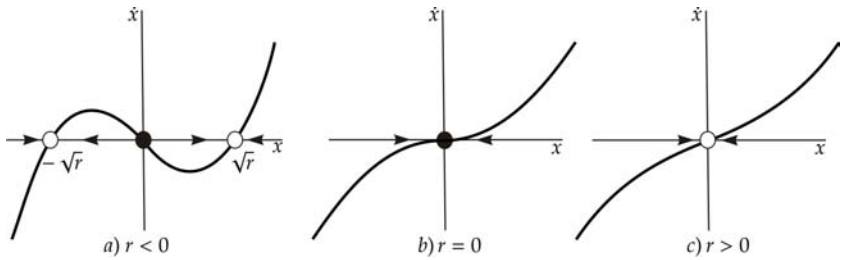

Figure 1.16: Phase space for a subcritical pitchfork bifurcation.

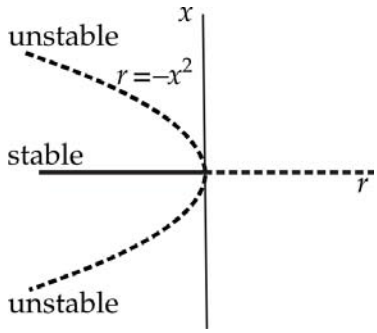

Figure 1.17: Bifurcation diagram for a subcritical pitchfork bifurcation.

Hopf Bifurcation

So far we have studied bifurcations that involve the collision of two or more fixed points and which occur when an eigenvalue of the system becomes 0. Despite the fact that these bifurcations are possible in systems of any dimension, they are the only possible ones for one dimensional systems.

In two dimensions there is another possibility for a fixed point to loose its stability. If we consider a stable fixed point, its eigenvalues λ_1 and λ_2 must both lie in the plane $Re(\lambda) < 0$. Since the eigenvalues satisfy a quadratic equation with real coefficients there are two possibilities, either the eigenvalues are both real and negative or they are complex conjugates. Since we have already dealt with the case of the eigenvalues passing through $\lambda = 0$ the only other possibility for a stable fixed point to become unstable is a complex conjugate pair of eigenvalues whose real part becomes positive. This is called a *Hopf Bifurcation* (or Andronov-Hopf bifurcation). Like the pitchfork bifurcation, Hopf bifurcations also can be subcritical or supercritical.

- **Supercritical Hopf Bifurcation**

In the *Supercritical Hopf Bifurcation*, a stable fixed point becomes unstable to a stable limit cycle. The normal form of this bifurcation is

$$\begin{aligned} \dot{x}_1 &= rx_1 - \omega x_2 - x_1(x_1^2 + x_2^2) \\ \dot{x}_2 &= \omega x_1 - rx_2 - x_2(x_1^2 + x_2^2) \end{aligned} \tag{1.8}$$

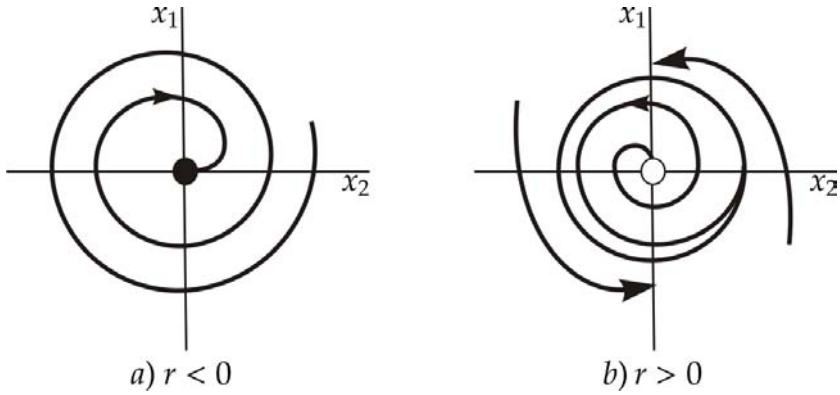

Figure 1.18: Phase space for a supercritical Hopf bifurcation.

This bifurcation is easier to study if we convert Eqs. (1.8) to polar coordinates,

$$\begin{aligned} \dot{\rho} &= r\rho - \rho^3 \\ \dot{\theta} &= \omega \end{aligned} \tag{1.9}$$

From this equation can be easily seen that, for $\omega \neq 0$, the only fixed point of the system is $\rho = 0$. If $r < 0$ this fixed point is stable, and becomes unstable for $r > 0$. However, for $r > 0$ there is a stable periodic orbit (given by $\dot{\rho} = 0$) at $\rho = \sqrt{r}$. This is illustrated in Fig. 1.18.

In Fig. 1.19(a) we plot the bifurcation diagram for this system, here we can see how the radio of the stable periodic orbits grows as $\sqrt{r}$. In Fig. 1.19(b) we sketch the pair of complex conjugate eigenvalues that cross the imaginary axis, as r becomes positive.

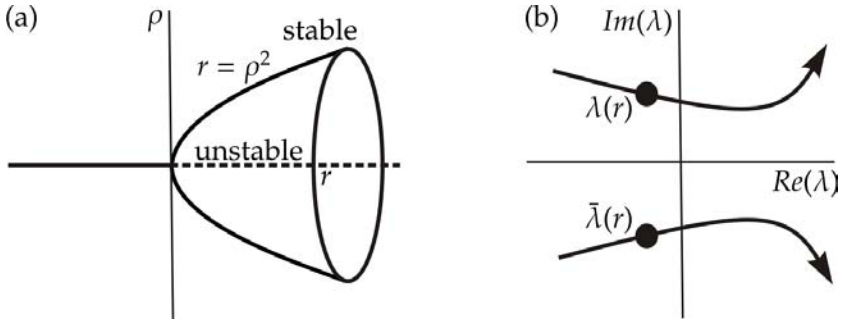

Figure 1.19: (a) Bifurcation diagram for a supercritical Hopf bifurcation. (b) Sketch of the complex conjugate pair of eigenvalues as they cross the imaginary axis in a Hopf bifurcation.

- **Subcritical Hopf Bifurcation**

As in the pitchfork bifurcation, the subcritical Hopf appears when we change the sign of the nonlinear term in the normal form. Therefore, it reads

$$\begin{aligned} \dot{x}_1 &= rx_1 - \omega x_2 + x_1(x_1^2 + x_2^2) \\ \dot{x}_2 &= \omega x_1 - rx_2 + x_2(x_1^2 + x_2^2) \end{aligned} \tag{1.10}$$

which in in polar coordinates yields

$$\begin{aligned} \dot{\rho} &= r\rho + \rho^3 \\ \dot{\theta} &= \omega \end{aligned} \tag{1.11}$$

For $r < 0$ there is a unstable limit cycle at $\rho = \sqrt{r}$ and a stable fixed point at $\rho = 0$. For $r > 0$ the unstable limit cycle disappears and the zero solution becomes unstable (Fig. 1.20). Since for $r > 0$ there are no stable invariant sets or fixed points, all the solutions explode to infinity. In physical systems there are usually higher order terms that stop the growth of the solution, creating stable invariant sets for the solution to converge to.

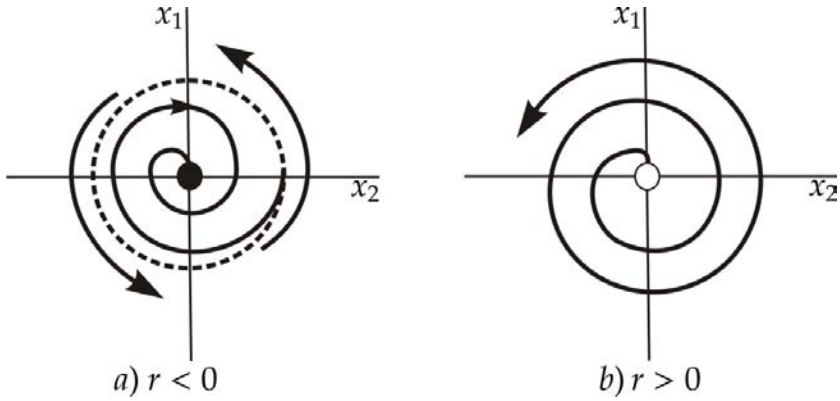

Figure 1.20: Phase space for a subcritical Hopf bifurcation.

This can be also seen in the bifurcation diagram shown in Fig. 1.21. Analog to the case of the pitchfork bifurcation, this bifurcation diagram is the mirror image of the supercritical Hopf bifurcation with the stability of the lines exchanged.

As in the supercritical case, there is a pair of complex conjugate eigenvalues that cross the imaginary axis at the bifurcation point. In fact, the linearization of the problem does not provide a distinction between the subcritical and the supercritical case. This distinction can be made in some cases analytically (by means of a weakly nonlinear analysis), but a quick way to do it is numerically. If a small attracting limit cycle appears right after the bifurcation, and shrink back to zero when the control parameter is reversed, then the bifurcation is supercritical. Otherwise the bifurcation is most probably subcritical.

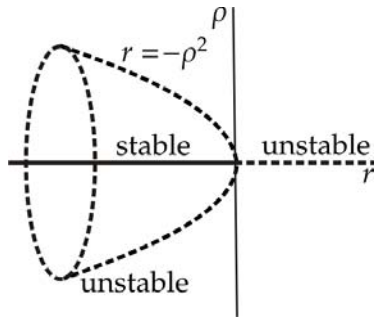

Figure 1.21: Bifurcation diagram for a subcritical Hopf bifurcation.

Saddle-Node on Invariant Circle Bifurcation

The *saddle-node on invariant circle bifurcation* (SNIC), also known as saddle-node infinite-period (SNIPER), or as saddle-node central homoclinic bifurcation, is a particular case of the saddle-node in two dimensions. It appears when a stable and unstable fixed points that collide at the bifurcation point are located on a limit cycle. Therefore, the normal form can be written in one dimension provided that the variable is the position inside the circle

$$\dot{\theta} = \omega - r \sin \theta \tag{1.12}$$

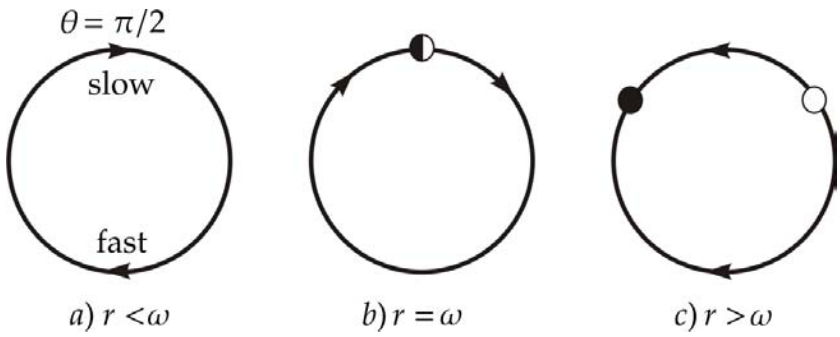

Figure 1.22: Bifurcation diagram for a saddle node in invariant circle bifurcation.

If $r = 0$ this equation reduces to a uniform oscillator. The control parameter r introduces a nonuniformity in the flow around the cycle, the flow is faster at $\theta = -\pi/2$ and slower at $\theta = \pi/2$. Since r increases this nonuniformity becomes more pronounced. When r is slightly less than ω the phase takes a long time to pass through the point $\theta = \pi/2$ (this is called a *bottleneck*), after which it completes the rest of the cycle very fast (Fig. 1.22). At $r = \omega$ the system no longer oscillates and a fixed point appears at $\theta = \pi/2$. Finally, for $r > \omega$ this fixed point splits in a stable and an unstable fixed points (as in the saddle-node bifurcation), the limit cycle is *broken*, and all the trajectories end at the stable fixed point. Since this is a special case of the saddle-node bifurcation there is also an eigenvalue that becomes 0 at the bifurcation point.

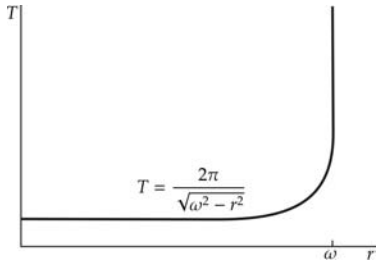

Figure 1.23: Period of oscillation as a function of the control parameter near a SNIC bifurcation.

Beyond the bifurcation point the system is said to be *excitable*, while resting on the stable fixed point, if the system undergoes a small perturbation it decays back to the resting state. But, if the system is perturbed beyond the saddle, it will make a long excursion on what remains of the limit cycle. We will go back to the concept of excitability in Sec. 5.4, since it will be a key behavior in the study of the dynamics of localized structures in Chapters 5 and 6.

An important signature of this bifurcation is how the period of the oscillations scales as r tends to ω. It can be shown that the period depends on r as [101]

$$T = \frac{2\pi}{\sqrt{\omega^2 - r^2}} \tag{1.13}$$

Due to this dependence this bifurcation is also called *infinite period bifurcation*, given that the period tends to infinity at the bifurcation point. In Fig. 1.23 we plot this dependence of the period T with r.

Saddle-Loop Bifurcation

In this bifurcation, an unstable fixed point collides with a limit cycle becoming a homoclinic orbit (that is why this bifurcation is also known as homoclinic or saddle-homoclinic)[102, 104]. Unlike the previous bifurcations discussed, in this bifurcation there is no change of sign of the real part of an eigenvalue at the bifurcation point. This is because the bifurcation involve changes of large portions of the phase space instead of changes on the stability of fixed points. At a difference with the previous cases, this is a global bifurcation.

The lowest number of dimensions in which this bifurcation can occur is two (since it requires the presence of a limit cycle). Therefore, the lower dimensional normal form that can be written for this bifurcation is

$$\begin{aligned} \dot{x}_1 &= x_2 \\ \dot{x}_2 &= rx_2 + x_1 - x_1^2 + x_1 x_2 \end{aligned} \tag{1.14}$$

Here the bifurcation occurs at $r_c \simeq -0.8645$. For $r < r_c$ the system has a stable limit cycle and a unstable fixed point at the origin (Fig. 1.24). When r tends to r_c the limit cycle approaches to the saddle, and for $r = r_c$ the limit cycle and the saddle collide, creating a homoclinic orbit. Then, for $r > r_c$ the saddle connection breaks, and the loop is destroyed.

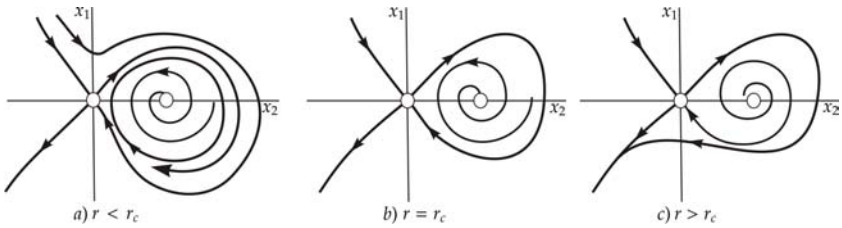

Figure 1.24: Bifurcation diagram for a saddle loop bifurcation.

In this bifurcation the period of the oscillations also tends to infinity as r tends to r_c, as in the SNIC bifurcation. In this case, however, the period of the oscillations scales as $\ln(r - r_c)$ [101].

If there is a fixed point close to the saddle, beyond the bifurcation the system also behaves in an excitable way as it happens with the SNIC bifurcation. This route to excitability is found and analyzed in more detail in Chapter 5.

1.4.2 Codimension-2 Bifurcations

Codimension-2 points are the intersections of two or more codimension-1 bifurcations, and can be seen as the point where these codimension-1 bifurcations are originated.

In this section we will summarize the codimension-2 bifurcations that we will find in Chapters 5 and 6, and its main properties. There are many more

codimension-2 bifurcations and the literature about the subject is wide, so we refer the reader to Refs. [103, 105] for a more extensive treatment.

Takens-Bogdanov Bifurcation

The Takens-Bogdanov (or double-zero) bifurcation occurs when a fixed point has two eigenvalues that become 0 simultaneously. Three codimension-1 bifurcations occur nearby the Takens-Bogdanov; a saddle-node, a Hopf and a saddle-loop bifurcation.

The presence of a Takens-Bogdanov bifurcation implies the presence of a Hopf bifurcation, therefore it can occur only for systems of dimension two or more. Hence, the lowest dimensional normal form that can be written is in two dimensions, and yields

$$\begin{aligned} \dot{x}_1 &= x_2 \\ \dot{x}_2 &= r_1 + r_2 x_1 + x_1^2 + \sigma x_1 x_2 \end{aligned} \tag{1.15}$$

We will show here the case for $\sigma = -1$ for which the Hopf bifurcation is supercritical. The case $\sigma = 1$ can be reduced to the case $\sigma = -1$ by the substitution $t \to -t$, $x_2 \to -x_2$. This does not affect the bifurcation curves but the limit cycle becomes unstable.

The bifurcation diagram is plotted in Fig. 1.25. The lines SN corresponds to the saddle-node bifurcation and is given by $r_1 = 1/4 r_2^2$. The Hopf bifurcation occurs along the line H, given by $r_1 = 0$ and $r_2 < 0$. The line SL corresponds to the saddle-loop bifurcation, and is given by $r_1 = -6/25 r_2^2 + O(r_2^3)$ and $r_2 < 0$.

The Takens-Bogdanov bifurcation occurs at the origin where there is a fixed point with two zero eigenvalues. Nearby the bifurcation the system has two fixed points, a saddle and a nonsaddle stationary point. For $r_2 > 0$ the nonsaddle is an unstable fixed point and for $r_2 < 0$ is a stable fixed point. The saddle and the nonsaddle collide and disappear in a saddle-node bifurcation that occurs along the SN line. For $r_2 < 0$ the stable fixed point undergoes a Hopf bifurcation generating a limit cycle (line H in Fig. 1.25). This limit cycle then degenerates into a homoclinic orbit to the saddle, and disappears in the saddle-loop bifurcation along the SL line.

This bifurcation can also be seen as the point in which a saddle-node bifurcation between a stable fixed point and a saddle (SN line for $r_2 < 0$) becomes a saddle-node bifurcation between a saddle and a unstable fixed point. Therefore from the unfolding of this critical point a Hopf and a saddle-loop bifurcation emerge.

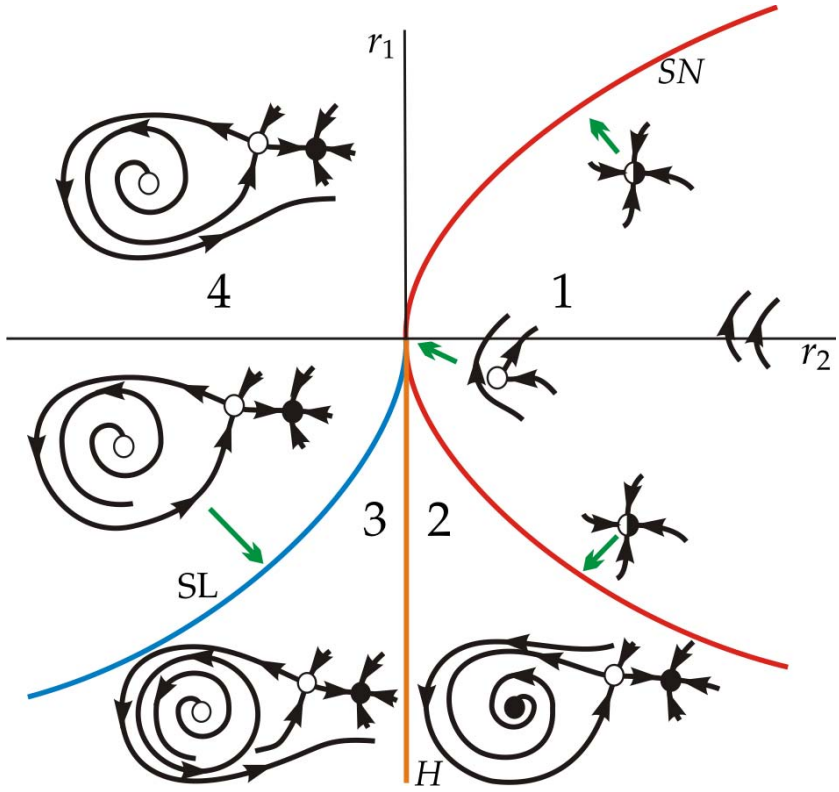

Figure 1.25: Bifurcation diagram for a Takens-Bogdanov.

Cusp Bifurcation

A *cusp bifurcation* is the point where two branches of saddle-node bifurcation curve meet tangentially. For nearby parameter values, the system can have three fixed points which collide and disappear pairwise via the saddle-node bifurcations.

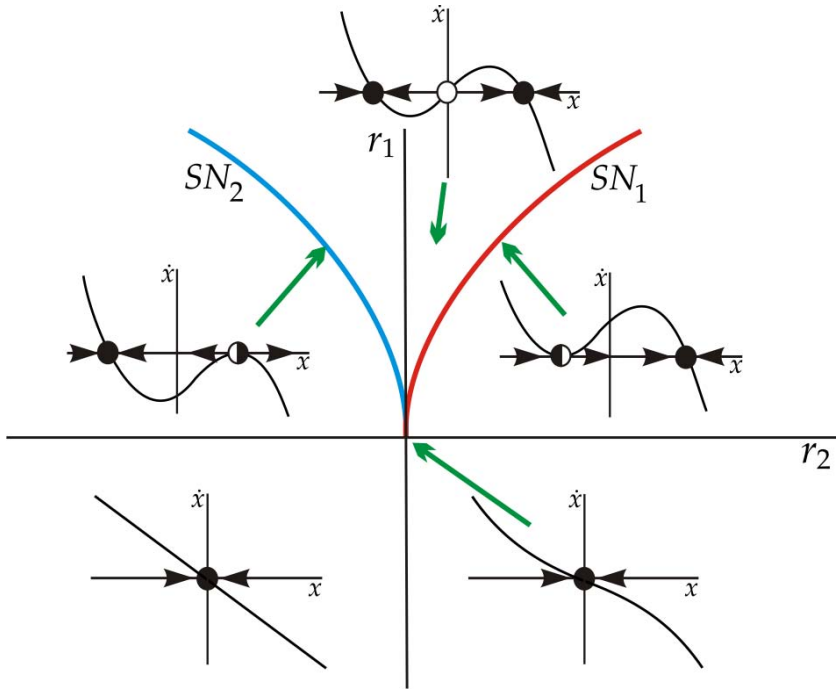

Figure 1.26: Bifurcation diagram for a cusp bifurcation.

Since this bifurcation involves two saddle-nodes, the lowest dimension needed for it to occur is one. Therefore, in one dimension, the normal form of this bifurcation is

$$\dot{x} = r_1 + r_2 x - x^3 \tag{1.16}$$

In Fig. 1.26 we plot the bifurcation diagram. The lines $SN1$ and $SN2$ correspond to the two saddle node bifurcations, and are given by $r_1 = \pm 2/(2\sqrt{3}) r_2^{3/2}$ for $r_2 > 0$ (the plus sign corresponds to the $SN1$ line and the minus to the $SN2$). In the region between the two lines there are three fixed points, two stable and a unstable fixed point. At the bifurcation lines one of the stable fixed points collides with the unstable one and therefore outside the wedge only a stable fixed point remains.

As we already stated for the saddle-node bifurcation, in more than one dimension the saddle-nodes that collide at the Cusp bifurcation can occur between a stable fixed point and a saddle, or two saddles.

Saddle-Node Separatrix Loop Bifurcation

A *saddle-node separatrix loop bifurcation* (SNSL) is the point where a saddle-node bifurcation (off limit cycle) becomes a saddle-node on invariant circle [106, 107]. It is also called called saddle-node noncentral homoclinic bifurcation or saddle-node homoclinic orbit bifurcation [108]).

Three codimension-1 occur nearby the SNSL point; a saddle-node, a saddle-loop and a saddle-node on invariant circle bifurcation. Hence, the presence of a SNSL bifurcation implies the nearby presence of a limit cycle, and therefore the minimum dimension in which this bifurcation can occur is two. In this case we choose to take a normal form in one dimension with a reset condition which defines a closed manifold. This normal form is

$$\dot{x} = r_1 + x^2 \quad \text{if } x \to \infty, \text{ then } x = r_2 \tag{1.17}$$

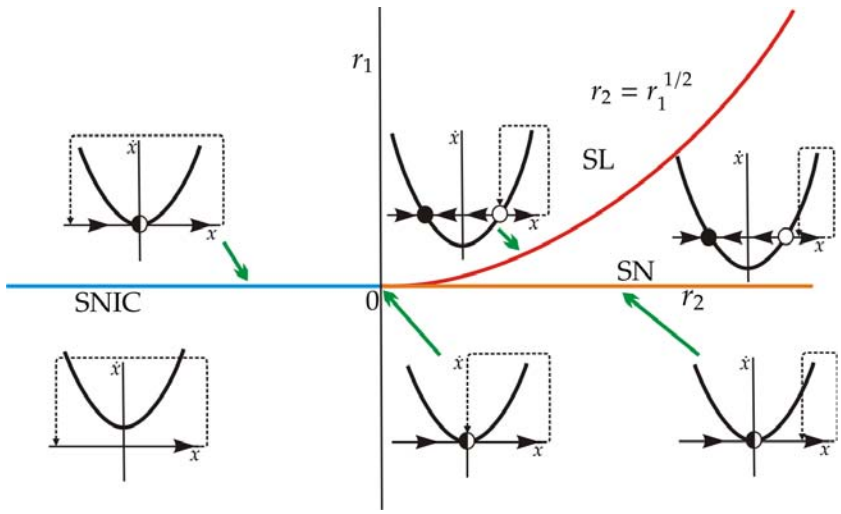

Figure 1.27: Bifurcation diagram for saddle-node separatrix loop bifurcation.

The bifurcation diagram is shown in Fig. 1.27. The line *SN* corresponds to the saddle-node (off limit cycle) bifurcation given by $r_1 = 0$ for $r_2 > 0$. The saddle-node on invariant circle occurs along the line *SNIC*, given by $r_1 = 0$ for $r_2 < 0$. The line *SL* is corresponds to the saddle-loop bifurcation and is given by $r_2 = r_1^{1/2}$.

The SNSL bifurcation occurs at the origin, where the three lines meet. In the plane $r_1 < 0$ the system behaves as if a limit cycle where present; x grows to infinity and then is reinjected to a finite value r_2. Crossing the *SNIC* line, a stable and unstable fixed point appear, while x is reinjected before these two fixed points. As we have already explained for the *SNIC* bifurcation in section 1.4.1 this creates an excitable behavior.

If we now cross the $r_1 = 0$ axis through the *SN* line, a stable and unstable fixed point also appear. For large values of r_2 the reinjection point of x now is beyond the pair of fixed points a *limit cycle* is created and the system is bistable. For initial conditions above the saddle the system will end at the fixed point, and for initial conditions beyond the saddle x will grow to infinity and then be reinjected again beyond the saddle staying always in this region of the phase space.

Crossing the *SL* line the system undergoes a saddle-loop bifurcation, in this case the reinjection point coincides with the saddle. Crossing this line coming from the bistability region (that is, decreasing r_2) the *limit cycle* is destroyed, and we are back to the region of excitable behavior.

Finally at the SNSL point the saddle-node bifurcation occurs at the same time as the *limit cycle* collides with the saddle.

1.5 Excitability

A system is said to be excitable if while it sits at a stable fixed point, perturbations above a certain threshold decay back to the rest state and beyond it induce a large response before coming back to it. Furthermore, after a large response the system cannot be excited again within a refractory period of time. In phase space [109, 110] excitability occurs for parameter regions where a stable fixed point is close to a bifurcation in which an oscillation is created. However the existence of such bifurcation is not a sufficient condition for excitability. A threshold, above which perturbations can drive the system to an excitable excursion, is also needed (a supercritical Hopf bifurcation does not produce an excitable regime by itself).

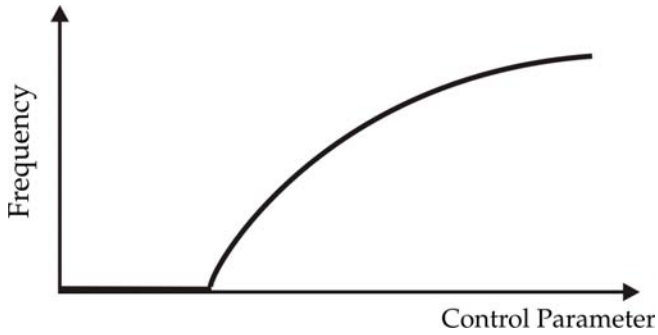

Figure 1.28: Schematic representation of the frequency of oscillations near a bifurcation leading to a Class I excitable system.

Excitable systems are widespread in nature, especially in biological systems. The most paradigmatic examples are of neurons [111, 112], and also cardiac tissue [113] and pancreatic β cells [114]. The first mathematical model to present excitable behavior was the one introduced by A. Hodgkin, and A. Huxley in 1952 to describe the voltage dynamics of the axon of the giant squid. A paradigmatic example of an excitable chemical system is the Belousov-Zhabotinskii reaction [115]. Both this system and the cardiac tissue constitute examples of excitable media, that is, an extended medium in which each point of the space is excitable.

As stated before, excitable behavior appears when the system considered is close to a bifurcation that gives birth to, for example, an oscillatory regime. Depending on the type of bifurcation present, the excitability can be classified in two types: Class I or Class II. This classification was first proposed by Hodgkin [116] when studying the response of neurons to an external stimulus and then formalized by Rinzel and Ermentrout [109] by means of bifurcation theory.

Class I excitability is characterized by the fact that the oscillatory regime created at the bifurcation exhibits frequencies with arbitrary low values (Figure 1.28). This kind of excitability arises through, for example, a saddle-node on invariant circle bifurcation or through saddle loop bifurcation. Among the systems that display this class of excitability, we can find the Hodgkin-Huxley model [111, 116] for certain parameters, and the Adler equation (Eq.1.13).

Class II excitability is characterized by the fact that the oscillations at the bifurcation point that creates the oscillatory regime start at nonzero frequency (Figure 1.29). This is the case for a Hopf bifurcation. In fact, systems close a subcritical Hopf, or a supercritical Hopf with a *Canard process* providing the excitability

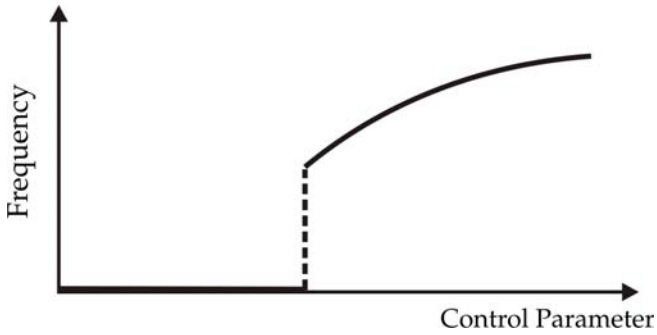

Figure 1.29: Schematic representation of the frequency of oscillations near a bifurcation leading to a Class II excitable system.

threshold [117] (systems with fast-slow dynamics) are excitable. Some examples of this class of excitability are the Hodgkin-Huxley model [111, 116] for some parameter regions, the FitzHug-Nagumo equation [112], the Morris-Lecar model for nervous cells [118] and the Belousov-Zhabotinskii reaction [119, 120].

There are also many other optical systems that display excitable behavior. Some examples are: systems with thermal effects (slow variable) that interplay with a hysteresis cycle of a fast variable like the cavity with T-dependent absorption [121] and the semiconductor optical amplifier [122] (Class II). There are also many systems in which excitability arises through a saddle-node in an invariant circle (Class I), like: lasers with saturable absorber [123], lasers with optical feedback [124, 125] and lasers with injected signal [126, 127]. Excitability trough a saddle-loop bifurcation appear in lasers with intracavity saturable absorber [128].

Excitability in optical systems was proposed for applications such as optical switching (responding to sufficiently high optical input signals) and pulse reshaping for optical communications, among other possibilities.

In Chapters 5 and 6 we show localized structures that display Class I excitable behavior. Remarkably enough, this excitable behavior is an emergent property of the LS itself, since the local dynamics of the system is not excitable.

1.6 Second Harmonic Generation

Second Harmonic Generation (SHG) is the process by which two photons of frequency ω combine to produce a photon at frequency 2ω. This effect, that was first demonstrated in 1961 [129], is mediated by crystal materials lacking inversion symmetry that exhibits a quadratic $\chi^{(2)}$ nonlinearity. Examples of these types of crystals are lithium niobate ($LiNbO_3$), potassium titanyl phosphate (KTP = $KTiOPO_4$), and lithium triborate (LBO = LiB_3O_5).

The physical mechanism behind the SHG can be understood as follows. The pump wave at frequency ω generates a nonlinear polarization which oscillates at twice this frequency because of the $\chi^{(2)}$ nonlinearity. According to Maxwell's equations, the nonlinear polarization radiates an electromagnetic field with this doubled frequency.

The second harmonic generation process occurs in two different ways of phase matching, denoted as Type I and Type II, depending on the polarizations of the incident and radiated waves. These two types will be explained in detail later.

In order to derive the equations that describe the SHG, we will proceed in the following way: first we will define the relevant reference frames with respect to the crystal axis, then we will write Maxwell equations and, from there, the wave equation in a nonlinear medium. Later, we will calculate the direction of propagation of ordinary and extraordinary waves in a birefringent medium, and write the corresponding wave equations. These equations will be simplified by means of the paraxial and slowly varying envelope approximations. Finally we will write the specific nonlinear term for second harmonic generation and further simplify the equation by means of the mean field approximation.

With the aim to keep this deduction as simple as possible, in this chapter we will skip the full calculations made to apply the Paraxial, Slolwy Varying Envelope and Mean Field approximations. The full procedure of these approximations will be detailed in Section 1.7 for the case of the Kerr Cavity, and the reader can refer to this section to have a deeper insight on these procedures, since they are analogous to those applied in this case.

1.6.1 Reference frames and birefringence

In the case of linear optics, the induced polarization depends linearly on the applied field by the well known relation $\vec{p}(\vec{E}) = \chi^{(1)}\vec{E}(t)$. In nonlinear optics, we can instead generalize this relation by expressing $\vec{p}$ as a power series:

$$\vec{p}(t) = \chi^{(1)}\vec{E}(t) + \chi^{(2)}\vec{E}(t) : \vec{E}(t) + \chi^{(3)}\vec{E}(t) : \vec{E}(t) : \vec{E}(t) + ... \tag{1.18}$$

The quantities $\chi^{(2)}$ and $\chi^{(3)}$ are second and third order tensors and are called second and third order nonlinear susceptibilities respectively. We have assumed here that the response of the medium to the field is instantaneous, i.e. that the polarization at time t only depends on the field at time t. This assumption implies -trough the Kramers-Kroning relations- that the medium must be lossless and dispersionless [130].

The second harmonic generation is a process that occurs with quadratic nonlinearity, described by the $\chi^{(2)}$ susceptibility. This coefficient is different from zero only in noncentrosymmetric crystals, which lack inversion symmetry. In materials with inversion symmetry $\chi^{(2)}$ is identically zero as, for instance, in gases. This implies that a material exhibiting second-order nonlinear interactions should be also anisotropic, i.e. the optical properties of the material are not the same in all the direction of the space. The case that we will study, is the one of a birefringent material, which is the simplest one. This type of material has a direction (called the optical axis) in which the refractive index is different to that of the other two directions.

When dealing with a wave propagating in a birefringent crystal, two different reference frames come into play, one given by wave propagation and another one given by the crystal axes. The wave propagates in the reference frame (x, y, z) along the z direction (Fig. 1.30). The axes of the anisotropic nonlinear crystal define the reference frame (X, Y, Z) where the Z is the optical axis of the crystal [131]. Without losing generality, we have chosen the x axis in the wave frame to coincide with the Y axis in the crystal frame as shown in Fig. 1.30. The plane ZY is called the *principal plane* (x and z also lie on this plane). If the incident light is polarized in the X direction perpendicular to the principal plane this wave will be affected by the ordinary refractive index n_o. This wave will travel inside the medium as it would do in a regular isotropic medium (that is it why is called *ordinary wave*). But if the wave is polarized in a direction which is inside the principal plane, forming an angle θ with the Z axis, it will be affected by a refractive index $n(\theta)$. In this case, the propagation vector $\vec{k}$ is no longer parallel to the direction of the pointing vector $\vec{S}$ so this is called an *extraordinary wave*.

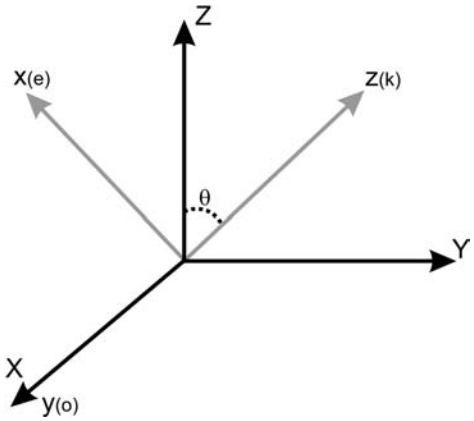

Figure 1.30: Crystallographic coordinate system (X,Y,Z) and wave propagation system (x,y,z). θ indicates the phase matching angle between the crystal optical axis Z and the wave propagation direction **k**. (o) and (e) stand for extraordinary and ordinary axis respectively.

The direction of extraordinary polarization is obtained by projecting the optical axis of the crystal Z onto the plane orthogonal to the propagation direction z. This direction coincides with the x direction, so we can identify the unitary vector of extraordinary polarization $\vec{e}$ with the x axis. The ordinary polarization is the one perpendicular to the principal plane so it coincides with the y axis, which can be identified with the unitary vector of ordinary polarization $\vec{o}$.

The transformation from the crystal frame to the wave frame is given by:

$$\begin{pmatrix} x \\ y \\ z \end{pmatrix} = \begin{pmatrix} 0 & -\cos\theta & \sin\theta \\ 1 & 0 & 0 \\ 0 & \sin\theta & \cos\theta \end{pmatrix} \begin{pmatrix} X \\ Y \\ Z \end{pmatrix} \tag{1.19}$$

1.6.2 Nonlinear wave equation

Now we write the Maxwell's equations for the electromagnetic field inside the nonlinear crystal:

$$\begin{aligned} \nabla \cdot \vec{D} = 0 \qquad & \nabla \times \vec{E} = -\partial_t \vec{B} \\ \nabla \cdot \vec{B} = 0 \qquad & \nabla \times \vec{H} = \vec{j} + \partial_t \vec{D} = \sigma \vec{E} + \partial_t (\epsilon_{\mathbf{r}} \cdot \vec{E} + \vec{P}_{NL}) \end{aligned} \tag{1.20}$$

where $\vec{E}$ and $\vec{B}$ are the electric and magnetic fields of the light beam. σ is the medium conductivity and $\vec{j}$ is the current density due to free charges. The electric field is related with the current density by Ohm's Law: $\vec{j} = \sigma\vec{E}$. Here we consider a nonconducting material, and therefore $\sigma = 0$. The magnetic field strength is related with the magnetic field by $\vec{B} = \mu\vec{H}$. For optical frequencies the material is non magnetic so we can consider that $\mu = \mu_0$, where μ_0 is the permeability of vacuum.

The medium response to the electric field is given by the electric displacement $\vec{D} = (\epsilon_{\mathbf{r}} \cdot \vec{E} + \vec{P}_{NL})$. $\epsilon_{\mathbf{r}}$ is the order 2 tensor of linear permittivity. In the crystal reference frame it takes diagonal form, and for an uniaxial crystal as the one we are considering is written as:

$$\epsilon_{\mathbf{r}}^{(X,Y,Z)} = \begin{pmatrix} \epsilon_o & & \\ & \epsilon_o & \\ & & \epsilon_e \end{pmatrix} \tag{1.21}$$

where ϵ_o is the permittivity along the ordinary axes of the crystal (X and Y) and ϵ_e is the permittivity along the extraordinary direction (Z) (the (X, Y, Z) superindex indicates that $\epsilon_{\mathbf{r}}$ is written in the crystal reference frame). The permittivity tensor can be written as $\epsilon_{\mathbf{r}} = \epsilon_\emptyset \epsilon_{\mathbf{r}r}$ where $\epsilon_\emptyset$ is the permittivity of the vacuum (we have chosen this nonstandard notation to avoid confusion with the permittivity along the ordinary direction ϵ_o), and $\epsilon_{\mathbf{r}r}$ is given by:

$$\epsilon_{\mathbf{r}r} = \begin{pmatrix} n_o^2 & & \\ & n_o^2 & \\ & & n_e^2 \end{pmatrix} \tag{1.22}$$

being n_o and n_e the ordinary and extraordinary refractive indices respectively.

From Maxwell's Equations (1.20) we can write:

$$\nabla \times \nabla \times \vec{E} = \nabla(\nabla \cdot \vec{E}) - \nabla^2\vec{E} = -\mu_0\partial_t^2\vec{D} \tag{1.23}$$

Using the equation for $\nabla \cdot \vec{D}$ and the relation between $\vec{D}$ and $\vec{E}$ we write, in the crystal reference frame:

$$\nabla \cdot \vec{E} = (1 - \epsilon_e/\epsilon_o)\partial_Z E_Z - \nabla \cdot \vec{P}_{NL}/\epsilon_o \tag{1.24}$$

The first term of the right hand side measures the deviation of the material from isotropy, if the three components of the permittivity tensor are equal this term vanishes. The second term is the effective charge density due to macroscopic properties of the material like the rearrangement of charges. Combining Eq. (1.24) with Eq. (1.23), we obtain the equation for the spatio-temporal evolution of the electric field in the crystal reference frame. This equation has the form of a wave equation (left hand side), with the added nonlinear terms (right hand side):

$$\nabla^2\vec{E} - (1-\gamma^2)\nabla(\partial_Z E_3) - \frac{1}{c^2}\partial_t^2(\epsilon_{\mathbf{r}r}\cdot\vec{E}) = -(\frac{1}{\epsilon_\emptyset n_o^2}\nabla\nabla\cdot - \mu_0\partial_t^2)\vec{P}_{NL} \tag{1.25}$$

where $\epsilon_o = \epsilon_\emptyset n_o^2$, $c = \omega/k_0$ is the speed of light in vacuum, and ω and k_0 are the wavelength and wavenumber in the vacuum also. We have written this equation in the reference frame of the crystal (X, Y, Z). We have also introduced the coefficient γ which is the ratio between the ordinary and extraordinary refractive indices: $\gamma^2 = \epsilon_e/\epsilon_o = n_e^2/n_o^2$.

1.6.3 Propagation directions inside the crystal

As we already stated, inside a birefringent crystal, light polarized in the ordinary and extraordinary directions will be affected by different refractive indices. With this in mind we want to calculate the polarization directions of the ordinary and extraordinary waves inside the medium, as a function of $n(\theta)$.

These directions are mainly determined by the linear part of Eq. (1.25). We consider a solution in the form of plane waves: $\vec{E} = \vec{p}e^{-\imath(\omega t - k_0 nz)}$ and introduce it in the linearized Eq. (1.25). Being $\partial_Z\vec{E}$ the only not vanishing gradient component, we obtain

$$\begin{aligned}
\frac{\partial\vec{E}}{\partial X} &= \frac{\partial\vec{E}}{\partial z}\frac{\partial z}{\partial X} = 0 \\
\frac{\partial\vec{E}}{\partial Y} &= \frac{\partial\vec{E}}{\partial z}\frac{\partial z}{\partial Y} = \sin(\theta)\frac{\partial\vec{E}}{\partial z} \\
\frac{\partial\vec{E}}{\partial Z} &= \frac{\partial\vec{E}}{\partial z}\frac{\partial z}{\partial Z} = \cos(\theta)\frac{\partial\vec{E}}{\partial z}
\end{aligned} \tag{1.26}$$

then, in the crystal reference frame (X, Y, Z):

$$\begin{pmatrix} n_o^2 - n^2 & 0 & 0 \\ 0 & n_o^2 - n^2 & (1-\gamma^2)n^2\cos(\theta)\sin(\theta) \\ 0 & 0 & (1-\gamma^2)n^2\cos^2(\theta) + n_e^2 - n^2 \end{pmatrix} \begin{pmatrix} p_1 \\ p_2 \\ p_3 \end{pmatrix} = \begin{pmatrix} 0 \\ 0 \\ 0 \end{pmatrix} \tag{1.27}$$

Solving this system is equivalent to solve an eigenvalue problem for n^2. The resolution of the system gives two values for n:

$$n = n_0 \qquad n(\theta) = n_e/\beta(\theta) \tag{1.28}$$

where we defined $\beta^2(\theta) = \gamma^2\cos^2(\theta) + \sin^2(\theta)$, and two polarizations:

$$\vec{p_o} = (p_1, 0, 0) \qquad \vec{p_e} = (0, p_2, -\frac{\tan(\theta)}{\gamma^2}p_2) \tag{1.29}$$

with refractive indices n_o and $n_e/\beta(\theta)$ respectively.

In the wave's reference frame these vectors become:

$$\vec{p_o'} = (0, p_1, 0) \qquad \vec{p_e'} = (p_2, 0, -\frac{\tau}{\beta^2}p_2) \tag{1.30}$$

where $\tau = \frac{1}{2}(\gamma^2 + 1)\sin(2\theta)$. By using this we define two vectors in the wave reference frame for the ordinary and extraordinary directions of polarization:

$$\vec{u_o} = (0, 1, 0) \qquad \vec{u_e} = (1, 0, -\frac{\tau}{\beta^2}) \cong (1, 0, 0) \tag{1.31}$$

As we have seen, the plane wave solutions of the linearized wave equation recover the expected behavior in a birefringent material: the ordinary wave, with refraction index n_0 is polarized orthogonal to the principal plane, while the extraordinary wave is polarized in a direction inside the principal plane.

Having determined the linear polarization of the ordinary and extraordinary waves, the spatio-temporal dynamics of the field is obtained taking into account these two polarization directions (ordinary and extraordinary). We consider the electric field as a plane wave propagating in the z direction, and slowly modulated by an amplitude $\vec{\xi}(x, y, z, t)$:

$$\vec{E}(x, y, z, t) = \vec{\xi}(x, y, z, t)e^{-\imath(\omega t - k_0 n z)} + c.c \tag{1.32}$$

where $\vec{\xi}(x,y,z,t)$ can be written as a sum of an ordinary and an extraordinary polarized components $\vec{\xi}(x,y,z,t) = \vec{u}_o\xi_o(x,y,z,t) + \vec{u}_e\xi_e(x,y,z,t)$.

First we consider the ordinary polarized component of the electric field, in this case $\vec{\xi}(x,y,z,t) = \vec{u}_o\xi_o(x,y,z,t)$, and $n = n_o$, so the linear part of the propagation equation Eq. (1.25) is:

$$\nabla_\perp^2\xi_o + \partial_z^2\xi_o + 2\imath n_o k_0\partial_z\xi_o - \frac{n_o^2k_0^2}{\omega^2}(\partial_t^2 - 2\imath\omega\partial_t)\xi_o = 0 \tag{1.33}$$

Where $\nabla_\perp^2 = \partial_x^2 + \partial_y^2$ is the transverse Laplacian. For the extraordinary wave $\vec{\xi} = \vec{u}_e\xi_e$ and $n = n_e/\beta^2$. In this case, the Z component of the field is proportional to the Y component, so we write only an equation for the latter. In this case, the linear part of the propagation equation yields:

$$\begin{aligned}\partial_y\xi_e + \overline{\beta}^2\partial_x^2\xi_e + \beta^2(\partial_z^2 + 2\imath k_0 n(\theta)\partial_z)\xi_e \\ +2\tau(\partial_{xz} + \imath k_0 n\partial_x)\xi_e - \frac{k^2n_e^2}{\omega^2}(\partial_t^2 - 2\imath\omega\partial_t)\xi_e = 0\end{aligned} \tag{1.34}$$

where we defined $\overline{\beta}^2 = \cos^2(\theta) + \gamma^2\sin^2(\theta)$. We will consider now, that the variations in space and time of the envelope $\vec{\xi}(x,y,z,t)$ are much smaller than the variations in space and time of the optical phase, i.e. any spatial variation of $\vec{\xi}(x,y,z,t)$ takes place in scales much smaller than $1/k_0$ and any temporal variation is much slower than $1/\omega$. These are called the slowly varying and paraxial approximations:

$$\begin{aligned}|\partial_z\vec{\xi}| \ll k_0 n|\vec{\xi}| \\ |\partial_t\vec{\xi}| \ll \omega|\vec{\xi}|\end{aligned} \tag{1.35}$$

Which are equivalent to:

$$\begin{aligned}|\partial_z^2\vec{\xi}| \ll k_0 n|\partial_z\vec{\xi}| \\ |\partial_{xz}^2\vec{\xi}| \ll k_0 n|\partial_x\vec{\xi}| \\ |\partial_t^2\vec{\xi}| \ll \omega|\partial_t\vec{\xi}|\end{aligned} \tag{1.36}$$

As already stated, here we apply this approximations without much justification, to keep this deduction as simple as possible. Quantitative arguments to justify them for physical beams are given in Sec. 1.7.1.

Under this approximations, Eqs. (1.33) and (1.34) give:

$$\nabla_\perp^2 \xi_o + 2\imath n_o k_0 (\partial_z - \frac{n_o}{c^2}\partial_t)\xi_o = 0 \tag{1.37}$$

$$(\partial_y^2 + \overline{\beta}^2 \partial_x^2)\xi_e + 2\imath k_0 n(\theta)(\beta^2 \partial_z + \tau \partial_x)\xi_e + 2\imath n_e k_0 (n_e/c)\partial_t \xi_e = 0 \tag{1.38}$$

These equations describe the linear propagation of the field envelope inside a birefringent crystal. In the following section we will consider the nonlinear interaction between the light and the crystal.

1.6.4 Nonlinear wave-mater interaction

As previously stated, we will deal here with the process of second harmonic generation which is a process that occurs in crystals with a $\chi^{(2)}$ nonlinearity. Since this is a three-wave mixing process, we write the Fourier component at frequency $\omega_n + \omega_m$ of the second order nonlinear polarization [130]:

$$P_{NLi}(\omega_n + \omega_m) = \sum_{j,k} \sum_{(n,m)} \chi^{(2)}_{ijk}(\omega_n + \omega_m, \omega_n, \omega_m) E_j(\omega_n) E_k(\omega_m) \tag{1.39}$$

where ijk refer to the cartesian components of the fields.

In the case of second harmonic generation $\omega_m = \omega_n = \omega$, so the sum over (mn) has only one term:

$$P_{NLi}(2\omega) = \sum_{j,k} \chi^{(2)}_{ijk}(2\omega, \omega, \omega) E_j(\omega) E_k(\omega) \tag{1.40}$$

$$P_{NLi}(w) = 2 \sum_{j,k} \chi^{(2)}_{ijk}(\omega, 2\omega, -\omega) E_j(2\omega) E_k(-\omega) \tag{1.41}$$

where we used the intrinsic permutation symmetry of the nonlinear susceptibility, $\chi^{(2)}_{ijk}(\omega_m + \omega_n, \omega_m, \omega_n) = \chi^{(2)}_{ijk}(\omega_m + \omega_n, \omega_n, \omega_m)$.

Each of the frequency components of the field can have projections onto the ordinary and extraordinary directions, so the P_{NLi} in general consists of a sum of four terms. Each of these terms will have a wave vector $\pm k_j \pm k_k$. Refractive and dispersive properties of uniaxial crystals permit only one of the four possible terms to be phase matched with k_i, a condition achieved by directing the pump beams in the appropriate directions. A slight misalignment Δk in the coupled fields produce a phase mismatch, which reduces the efficiency of second harmonic generation.

Considering a positive crystal ($\gamma > 1$), the allowed phase-matched configurations are the Type I, in which the two pump fields at frequency ω are polarized in the extraordinary direction and the second harmonic field is polarized in the ordinary direction, and the Type II in which there is one pump field polarized in the extraordinary direction and the other in the ordinary direction, and the second harmonic field is either ordinary or extraordinary.

In this case we will consider the Type II second harmonic generation, so the polarization fields are:

$$P_{NLo}(2\omega) = d_{eff} E_e(\omega) E_o(\omega) \tag{1.42}$$

$$P_{NLe}(w) = d_{eff} E_e(2\omega) E_o^*(\omega) \tag{1.43}$$

$$P_{NLo}(w) = d_{eff} E_e(2\omega) E_e^*(\omega) \tag{1.44}$$

where d_{eff} is obtained by evaluation of the summation $\sum_{jk}$, and depends on the type of crystal considered [130, 132]. We have considered it to be independent of the frequency, and we also used that $E(-\omega) = E^*(\omega)$.

By using the slowly varying envelope and paraxial approximations for the nonlinear polarization term, we obtain the equations for the nonlinear spatio-temporal dynamics of the field:

$$\frac{n_o}{c}\partial_t A_o = \frac{\imath}{2k_0 n_o}\nabla_\perp^2 A_o - \partial_z A_o + \imath\frac{\omega d_{eff}}{n_o c} B A_e^* e^{-\imath\Delta kz} \tag{1.45}$$

$$\frac{n(\theta)}{c}\partial_t A_e = \frac{\imath}{2k_0 n(\theta)}\left(\frac{\overline{\beta}^2}{\beta^2}\partial_x^2 + \frac{1}{\beta^2}\partial_y^2\right) A_e - \partial_z A_e + \tan\rho\partial_x A_e + \imath\frac{\omega d_{eff}}{n(\theta)c} B A_o^* e^{\imath\Delta kz} \tag{1.46}$$

$$\frac{n(\theta)}{c}\partial_t B = \frac{\imath}{2k_0 n(\theta)}\left(\frac{\overline{\beta}^2}{\beta^2}\partial_x^2 + \frac{1}{\beta^2}\partial_y^2\right) B - \partial_z B + \tan\rho\partial_x B + \imath\frac{2\omega d_{eff}}{n(\theta)c} A_e A_o e^{\imath\Delta kz} \tag{1.47}$$

where we identified A with the slowly varying envelope at frequency ω and B with the slowly varying envelope at 2ω. We defined also $\tan\rho = \tau/\beta^2$. ρ is called the walk-off angle, produced by the crystal birefringence.

Phase-matched processes occur for:

$$\vec{k}_B^{(e)}(\theta) = k_A^{(e)}(\theta) + k_A^{(o)} + \vec{\Delta k} \tag{1.48}$$

where $\vec{\Delta k}$ is a small phase mismatch. In terms of photons this is the condition for momentum conservation.

For the sake of simplicity we considered here that n_o and n_e are independent of the frequency, which in general is not true, but is a good approximation in our case.

Then, Eqs. (1.45-1.47) can be written in a more compact form:

$$\frac{n_o}{c}\partial_t A_o = \frac{\imath}{2k_0 n_o}\nabla_\perp^2 A_o - \partial_z A_o + \imath\frac{\omega d_{eff}}{n_o c}BA_e^* e^{-\imath\Delta kz} \tag{1.49}$$

$$\frac{n(\theta)}{c}\partial_t A_e = \frac{\imath}{2k_0 n(\theta)}\nabla_\perp^{2\,e} A_e - \partial_z A_e + \tan\rho\partial_x A_e + \imath\frac{\omega d_{eff}}{n(\theta)c}BA_o^* e^{\imath\Delta kz} \tag{1.50}$$

$$\frac{n(\theta)}{c}\partial_t B = \frac{\imath}{2k_0 n(\theta)}\nabla_\perp^{2\,e} B - \partial_z B + \tan\rho\partial_x B + \imath\frac{2\omega d_{eff}}{n(\theta)c}A_e A_o e^{\imath\Delta kz} \tag{1.51}$$

where we defined $\nabla_\perp^{2\,e} = \frac{1}{\beta^2}\nabla_\perp^2 + \beta_e\partial_x^2$ with $\beta_e = \tan\rho\tan\theta$.

1.6.5 Mean field approximation

In order to enhance the conversion of the fundamental field to the second harmonic, the nonlinear crystal is usually placed inside a cavity forming an oscillator (Fig. 1.31). This imposes boundary conditions to the field propagation which should be dealt with. We consider the crystal inside a doubly resonant cavity, i.e. resonant at frequencies ω and 2ω. Considering a plane mirror cavity the field can be decomposed into its longitudinal fourier modes, and under the mean field approximation we only take into account the fundamental mode. This implies that not z dependence of the field is modeled, once the boundary conditions at the mirrors of the cavity are taken into account. In Sec. 1.7.2 we will give more details of this approximation for a cavity filled with a $\chi^{(3)}$ medium, instead of a $\chi^{(2)}$ (We skip this description here because it can be given in a more compact form for the single equation of the Kerr cavity). Finally we consider a phase matched ($\Delta k = 0$ and walk off compensated ($1/\beta^2 = 1, \tan\rho = 0, \overline{\beta^2}/b^2 = 1$) system. Under this approximations we obtain [133–136]:

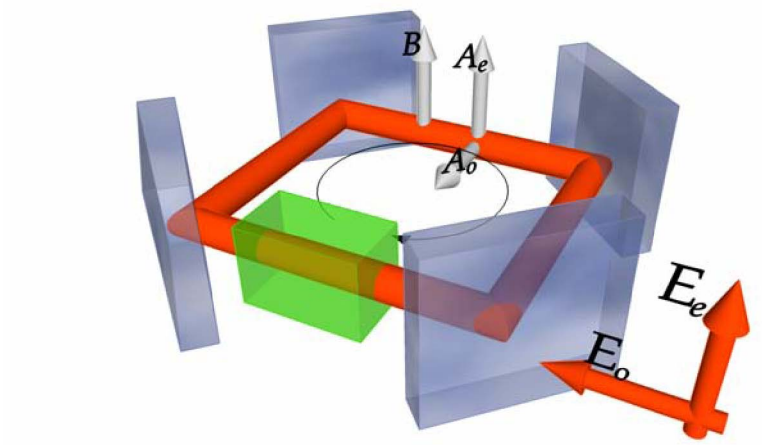

Figure 1.31: Ring cavity with a χ^2 nonlinear medium. E_e and E_o are the input fields in the extraordinary and ordinary directions respectively. $|A_o|$ and $|A_e|$ are the intracavity fundamental fields and $|B|$ is the intracavity second harmonic field .

$$\partial_t A_o = (1 + \imath\delta_A)A_o + \imath\nabla_\perp^2 A_o + \imath A_e^* B + E_o \tag{1.52}$$

$$\partial_t A_e = (1 + \imath\delta_A)A_e + \imath\nabla_\perp^2 A_e + \imath A_o^* B + E_e \tag{1.53}$$

$$\partial_t B = (1 + \imath\delta_B)B + \frac{\imath}{2}\nabla_\perp^2 B + \imath A_e A_o \tag{1.54}$$

where A_o, A_e and B where rescaled and are now adimensional fields, and E_o and E_e are the normalized external pumps. $\Delta = \omega \quad \omega_c$ and $\Delta_0 = 2\omega \quad \omega_c'$ are the detunings between the frequency of the field (ω and 2ω) and the closest resonance frequency of the cavity (ω_c and ω_c'). The time of the equations has been rescaled in units of the cavity relaxation time and the space in units of the diffraction constant.

1.7 Kerr Cavities

The optical Kerr effect (or simply Kerr effect) is a change in the refractive index of a material in response to the electric field of light propagating inside the medium. This effect occurs when the material has an order three nonlinearity, described by a $\chi^{(3)}$ medium (i.e. $\chi^{(3)}$ term for the polarization in Eq. (1.18) is nonzero). Depending on the sign of this change of the refractive index, the Kerr effect can lead to self focusing, if the refractive index increases with the field intensity, or self defocusing in the opposite case. These effects can be easily understood by geometric optics. In a medium with a non homogeneous refractive index the light rays turn from regions of low refractive index to regions of high refractive index. Therefore, in the self focusing case, regions where the electric field is more intense, the refractive index increases creating a positive feedback and further increasing the focalization of the field. As the light propagates inside the medium it continues to focus leading to the formation of light filaments. The self defocusing effect can be understood in an analog way. When the medium is placed inside a cavity, the filamentation is balanced by diffraction, and this balance leads to the formation of Localized Structures.

In this section we will derive the Lugiato-Lefever [137] model for a cavity filled with a Kerr medium. We will start from Eq. (1.23) for $\nabla \times \nabla \times \vec{E}$ that we derived in Section 1.6.2. Then we will apply the slowly varying and paraxial approximations to derive an equation for the transversely polarized component of the field. We will then apply the Mean Field approximation to eliminate the dependence of the equations on the transverse variable. Finally, we will introduce the explicit form of the nonlinear term, to arrive to the desired equation.

1.7.1 Nonlinear wave equation and paraxial approximation

To derive the equation for a Kerr cavity, we start from Eq. (1.23) for the electric field inside the nonlinear medium. In this case, since the medium is isotropic, we can avoid the discussion given in Section 1.6.2 because here the refractive index seen by a wave inside the material will be independent of the polarization direction. Thus, in this case the permittivity ϵ of the material is a scalar, and therefore Eq. (1.24) can be written as:

$$\nabla \cdot \vec{E} = -\nabla \cdot \vec{P}_{NL}/\epsilon \tag{1.55}$$

And Eq. (1.25) can be written as:

$$\nabla^2\vec{E} - \frac{1}{c^2}\partial_t^2(\epsilon\vec{E}) + (\frac{1}{\epsilon_\emptyset n}\nabla\nabla\cdot - \mu_0\partial_t^2)\vec{P}_{NL} = 0 \tag{1.56}$$

This is a vectorial wave equation with the added nonlinear terms. Analogously to what we have done for the case of second harmonic generation we consider the electric field as a slowly modulated plane wave propagating in the z direction,

$$\begin{aligned}\vec{E}(x,y,z,t) &= \vec{E}(x,y,z,t)e^{-\imath(\omega t-kz)} + c.c \\ &= (\vec{E}_\perp + E_z\vec{k})e^{-\imath(\omega t-kz)} + c.c\end{aligned} \tag{1.57}$$

with $\omega/k = c$, and we write the nonlinear polarization in a similar form:

$$\begin{aligned}\vec{P}_{NL}(x,y,z,t) &= \vec{P}_{NL}(x,y,z,t)e^{-\imath(\omega t-kz)} + c.c \\ &= (\vec{P}_{NL\perp} + P_{NLz}\vec{k})e^{-\imath(\omega t-kz)} + c.c\end{aligned} \tag{1.58}$$

where we explicitly considered the polarization components in the propagation direction and transverse to the propagation direction.

At this point, we will apply the slowly varying and paraxial approximations. We will consider now that the variations in space and time of the envelope are much smaller than the variations in space and time of the optical phase. The usual way to do this is to make the uncontrolled approximation of dropping $\nabla\nabla\cdot$ and the second derivatives in z and t, as we did in Sections 1.6.3 and 1.6.4 for the case of second harmonic generation. Here we will show how these approximations can be done in a rigorous and self consistent way by expanding the equation in terms of a small parameter [138, 139].

First we need to consider the characteristic scales of the electric field. We will consider a Gaussian-like beam, with a characteristic width w_0 in the transverse dimension. For such a beam there is an naturally associated diffraction length $l = kw_0^2$, which is the characteristic length in the longitudinal direction [140], and a characteristic time $\tau = l/c$.

In this way we define a smallness parameter $\eta = w_0/l$, which is the ratio between the beam waist and the diffraction length, for assessing the relative magnitude of the various spatial and temporal derivatives in Eq. (1.56). We rescale the independent variables in terms of their characteristic scales:

$$x \to \frac{x}{w_0} \qquad y \to \frac{y}{w_0} \qquad z \to \frac{z}{l} \qquad t \to \frac{t}{\tau} \tag{1.59}$$

Then, using these definitions and introducing Eqs. (1.57) and (1.58) into Eq. (1.56), we obtain

$$\begin{aligned} \nabla_\perp^2 \left(\eta^2 \nabla_\perp \cdot \vec{E}_\perp + \imath\eta E_z + \eta^3 \partial_z E_z\right) - \eta^2 \nabla_\perp^2 \vec{E}_\perp - \eta^4 \partial_{z^2}^2 \vec{E}_\perp - 2\imath\eta^2 \partial_z \vec{E}_\perp = \\ -\eta^4 \partial_{t^2}^2 \vec{E}_\perp + 2\imath\eta^2 \partial_t \vec{E} - \mu_0 c^2 \left[\eta^4 \partial_{t^2}^2 \vec{P}_{NL\perp} - 2\imath\eta^2 \partial_t \vec{P}_{NL\perp} - \vec{P}_{NL\perp}\right] \end{aligned} \tag{1.60}$$

for the transverse part, and

$$\begin{aligned} \eta^3 \partial_z \left(\nabla_\perp \cdot \vec{E}_\perp\right) + \imath\eta \nabla_\perp \cdot \vec{E}_\perp - \eta^2 \nabla_\perp \cdot E_z) = \\ -\eta^4 \partial_{t^2}^2 E_z + 2\imath\eta^2 \partial_t E_z + E_z - \mu_0 c^2 \left[\eta^4 \partial_{t^2}^2 \vec{P}_{NLz} - 2\imath\eta^2 \partial_t \vec{P}_{NLz} - \vec{P}_{NLz}\right] \end{aligned} \tag{1.61}$$

for the longitudinal part. Now we expand the fields in terms of η

$$\begin{aligned} \vec{E}_\perp &= \vec{E}_\perp^{(0)} + \eta \vec{E}_\perp^{(1)} + \eta^2 \vec{E}_\perp^{(2)} + ... \\ E_z &= E_z^{(0)} + \eta E_z^{(1)} + \eta^2 E_z^{(2)} + ... \\ \vec{P}_{NL\perp} &= \eta^2 \vec{P}_{NL\perp}^{(0)} + \eta^3 \vec{P}_{NL\perp}^{(1)} + ... \\ \vec{P}_{NLz} &= \eta^2 \vec{P}_{NLz}^{(0)} + \eta^3 \vec{P}_{NLz}^{(1)} + ... \end{aligned} \tag{1.62}$$

Where we assume $|\vec{P}| = O(\eta^2)$ because the nonlinear polarization is much smaller than $|E|$.

We now collect the terms in Eqs. (1.61) and (1.62) at each order in η. At $O(\eta^0)$ we find

$$E_z = 0 \tag{1.63}$$

This condition implies that at order zero the field is purely transverse, but higher order corrections should be considered to ensure that the field will satisfy Maxwell's equations. At $O(\eta)$ we get

$$E_z^{(1)} = \imath \nabla_\perp^2 \vec{E}_\perp^{(0)} \tag{1.64}$$

$$\nabla_\perp^2 \vec{E}_\perp^{(0)} + 2\imath\partial_z \vec{E}_\perp^{(0)} + 2\imath\partial_t \vec{E}_\perp^{(0)} = \frac{1}{\epsilon_\emptyset} \vec{P}_{NL\perp}^{(0)} \tag{1.65}$$

Finally, we use Eqs. (1.59) and (1.63) to recover the original variables and, dropping the subscripts on the field variables, we obtain a simplified nonlinear wave equation for the transversely polarized component of the field

$$\nabla_\perp^2 \vec{E} \quad 2\imath k \left(\partial_z \vec{E} + \frac{1}{c} \partial_t E \right) = \mu_0 \omega^2 \vec{P}_{NL} \tag{1.66}$$

1.7.2 Mean field approximation

As stated in section 1.6.5 for second harmonic generation, we will consider that the nonlinear medium is placed inside a resonant cavity in order to enhance the interaction of the light with the medium. By using the boundary conditions imposed by the cavity we will show how it is possible to further simplify Eq. (1.66) by eliminating the dependence on z, under a suitable set of assumptions.

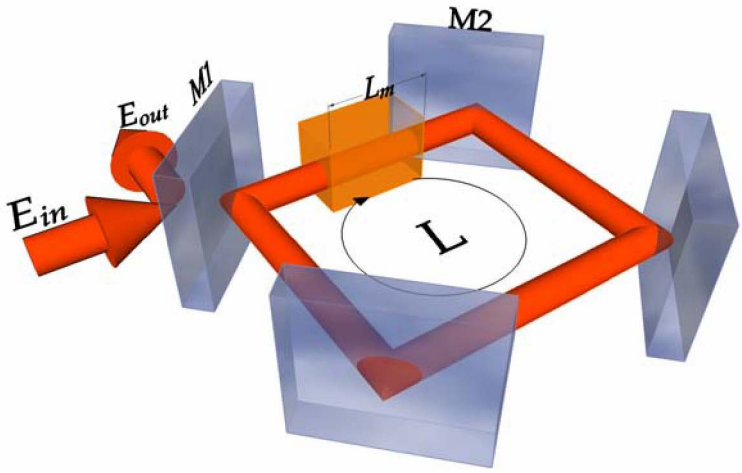

Figure 1.32: Ring Cavity with a nonlinear medium.

We choose the geometry shown in Fig. 1.32, a ring cavity of length L with flat mirrors, containing a thin nonlinear medium of length L_m and pumped by E_{in}. We will assume that the medium is thin and, therefore, we can neglect diffraction within it. Therefore the equation for the field inside the medium becomes

$$\left(\partial_z \vec{E} + \frac{1}{c}\partial_t \vec{E}\right) = -\frac{k}{\epsilon_\emptyset}\vec{P}_{NL} \tag{1.67}$$

In order to compute the boundary condition at the entrance of the nonlinear medium ($z = 0$). We need to compute the propagator of the field while it travels through the empty cavity. This is done by solving Eq. (1.66) without polarization which yields:

$$\vec{E}(x, y, z, t - z/c) = e^{z\left(\frac{i}{2k}\nabla^2 - \frac{i\omega}{c}\right)}\vec{E}(x, y, 0, t) \tag{1.68}$$

Then the boundary condition is

$$\vec{E}(x, y, 0, t) = Re^{-i\delta_0 + (L-L_m)\frac{i}{2k}\nabla^2}\vec{E}\left(x, y, L_m, t - \frac{L - L_m}{c}\right) + T\vec{E}_i(x, y, t) \tag{1.69}$$

where the right hand side is the field propagated from the end of the nonlinear crystal $z = L_m$ through the cavity. $R = 1 - T$ is the reflectivity of the mirrors M1 and M2, and δ_0 is the cavity detuning defined as

$$\delta_0 = \frac{(\omega_c - \omega)L}{c} + O(L_m) \tag{1.70}$$

where ω_c is the frequency of the longitudinal cavity mode closest to the frequency ω of the input field. The $O(L_m)$ term is explicitly $-(w/c)L_m$ which is an additional term to the detuning due to the propagation inside the nonlinear crystal. Since L_m is considered to be small, this term will be neglected from now on. Finally, $E_i(x, y)$ is the input field at the entrance of the nonlinear medium.

Now we will define a transformation in order to convert this boundary condition into a periodic boundary condition in the new variables. Therefore we define:

$$\begin{aligned} z' &= z \\ t' &= t + \left(\frac{L - L_m}{c}\right)\frac{z}{L_m} \\ \Rightarrow \partial_z + \frac{1}{c}\partial_t &= \partial_{z'} + \frac{L}{cL_m}\partial_{t'} \end{aligned} \tag{1.71}$$

and a new field variable $\vec{E}'(x, y, z', t')$

$$\vec{E}'(x, y, z', t') = \hat{\Gamma}\vec{E}(x, y, z', t') + T\vec{E}_i(x, y)\frac{z'}{L_m} \tag{1.72}$$

where we defined

$$\hat{\Gamma} = e^{\frac{z'}{L_m}\left(\ln R - \imath\delta_0 + (L - L_m)\frac{\imath}{2k}\nabla^2\right)} \tag{1.73}$$

Then, in the new variables, the boundary condition becomes

$$\vec{E}'(x, y, 0, t') = \vec{E}'(x, y, L_m, t') \tag{1.74}$$

that is, the boundary conditions in the new variables are expressed in terms of the fields at the same time, and they are periodic in z'. This simplification of the boundary conditions comes to the price of making complicating the field equation that now reads

$$\begin{aligned} \partial_{t'}\vec{E}' + \frac{cL_m}{L}\partial_{z'}\vec{E}' = \frac{cL_m}{L}\left[\left(\ln R - \imath\delta_0 + (L - L_m)\frac{\imath}{2k}\nabla^2\right)\frac{\vec{E}}{L_m} + \hat{\Gamma}\partial_{z'}\vec{E}\right] \\ + \hat{\Gamma}\partial_{t'}\vec{E} + \frac{cT\vec{E}_i}{L} \end{aligned} \tag{1.75}$$

Now we use that $\vec{E} = \Gamma^{-1}\left(\vec{E}' - T\vec{E}_i\frac{z'}{L_m}\right)$ and Eq. (1.67) to get

$$\begin{aligned} \partial_{t'}\vec{E}' + \frac{cL_m}{L}\partial_{z'}\vec{E}' = \frac{cL_m}{L}\left[\left(\ln R - \imath\delta_0 + (L - L_m)\frac{\imath}{2k}\nabla^2\right)\frac{\Gamma^{-1}}{L_m}\left(\vec{E}' - T\vec{E}_i\frac{z'}{L_m}\right)\right] \\ + \frac{cT\vec{E}_i}{L} - \frac{ckL_m}{L\epsilon_\emptyset}\Gamma\vec{P}_{NL} \end{aligned} \tag{1.76}$$

At this point, we will introduce a set of approximations that will allow us to simplify Eq. (1.76). We assume

$$\begin{cases} T \ll 1 \\ \delta_0 \simeq O(T) \ll 1 \\ kL_m/\epsilon_\emptyset \simeq O(T) \ll 1 \\ C = kL_m/T\epsilon_\emptyset \simeq O(1) \\ \theta = \delta_0/T \simeq O(1) \\ a = (L - L_m)/2kT \simeq O(1) \end{cases} \tag{1.77}$$

$T \ll 1$ implies a high finesse cavity, that means that the frequency spacing between longitudinal modes is large compared to their bandwidth. $\delta_0 \ll 1$ means that the frequency of the input field is close to the frequency of one of the longitudinal modes of the cavity. These two conditions ensure that only one of the longitudinal modes of the cavity will be excited by the input field. The entire set of conditions assumes that the change of the field after one pass in the cavity is small, although the cumulative effect after many round trips will be significant.

Under these assumptions we are able to simplify the field equation (1.76). First we expand the operator $\hat{\Gamma}$ up to first order:

$$\hat{\Gamma} \simeq 1 + \frac{z'}{L_m}\left(\ln R - \imath\delta_0 + (L - L_m)\frac{\imath}{2k}\nabla^2\right) + O(2) \tag{1.78}$$

Then, using that $\ln R = \ln(1 - T) \simeq -T$ and keeping terms up to $O(T)$ we arrive to the following equation:

$$\partial_{t'}\vec{E}' + \frac{cL_m}{L}\partial_{z'}\vec{E}' = \gamma(-\vec{E}' - \imath\theta\vec{E}' + \imath a\nabla^2\vec{E}' + \vec{E}_i - C\vec{P}_{NL}) \tag{1.79}$$

where $\gamma = cT/L$ is the cavity decay rate. This equation still has an explicit dependence on z', however, since $\vec{E}'$ is periodic we can expand it and $\vec{P}_{NL}$ as a Fourier series. Under the assumptions that we have made, the only mode that will interact with the input field is the one at zero frequency, this means that $\vec{E}'$, and hence $\vec{P}_{NL}$, will be independent of z' and therefore we can drop the $\partial_{z'}\vec{E}'$ from Eq. (1.79). Then the Mean Field Equation reads

$$\partial_{t'}\vec{E}' = \gamma(-\vec{E}' - \imath\theta\vec{E}' + \imath a\nabla^2\vec{E}' + \vec{E}_i - C\vec{P}_{NL}) \tag{1.80}$$

This equation describes the evolution of the field inside a nonlinear medium placed inside a ring cavity. The remaining step to arrive to the Kerr model equations is to define the dependence of P with E for the third order nonlinear process. This will be done in the next section.

A final point should be made about the type of cavities in which this model and the one derived for second harmonic generation are valid. We derived these equations for a ring cavity where we supposed that the field inside it propagates only in one direction. For Fabry-Perot cavities this is no longer true since we have to consider two counterpropagating modes, and their interaction. Hence, the results obtained with these models for a ring cavity cannot be, in general, extrapolated to Fabry-Perot cavities [141].

1.7.3 Nonlinear wave matter interaction

As we did in section 1.6.4 for the second order nonlinearity, we will write here an equivalent expression for the polarization as a function of the electric field. In the case of a χ^3 nonlinearity this expression describe a four-wave mixing process and reads [130]

$$P_{NLi}(\omega_o + \omega_n + \omega_m) = \sum_{j,k,l} \sum_{(n,m,o)} \chi^{(3)}_{ijkl}(\omega_o + \omega_n + \omega_m, \omega_o, \omega_n, \omega_m) \ldots E_j(\omega_o) E_k(\omega_n) E_l(\omega_m) \tag{1.81}$$

where i, j, k, l refer to the cartesian components of the field. Summing over m, n, o we obtain

$$P_{NLi}(\omega_o + \omega_n + \omega_m) = D \sum_{j,k,l} \chi^{(3)}_{ijkl}(\omega_o + \omega_n + \omega_m, \omega_o, \omega_n, \omega_m) \ldots E_j(\omega_o) E_k(\omega_n) E_l(\omega_m) \tag{1.82}$$

where the degeneracy factor D represents the number of distinct permutations of the frequencies ω_m, ω_n and ω_o. We are interested in studying the case of nonlinear refractive index, given by the choice of frequencies $\chi^{(3)}_{ijkl}(\omega, \omega, \omega, -\omega)$. In this case $D = 3$ and the nonlinear polarization becomes

$$P_{NLi}(\omega) = 3\sum_{j,k,l} \chi^{(3)}_{ijkl}(\omega,\omega,\omega,-\omega)E_j(\omega)E_k(\omega)E_l(-\omega) \tag{1.83}$$

For the selected frequencies and an isotropic medium Eq. (1.83) can be written in vectorial form as [130]

$$\vec{P}_{NL} = 6\chi_{1122}(\vec{E}\cdot\vec{E}^*)\vec{E} + 3\chi_{1122}(\vec{E}\cdot\vec{E})\vec{E}^* \tag{1.84}$$

where we used that $\vec{E}(-\omega) = \vec{E}^*(\omega)$

Considering only linearly polarized fields, this vectorial equation reduces to the scalar expression

$$\vec{P}_{NL} = A|E|^2E \tag{1.85}$$

where we defined $A = 6\chi_{1122} + 3\chi_{1122}$.

With this expression for the nonlinear polarization as a function of the electric field Eq. (1.80) yields

$$\partial_{t'}E' = \gamma(-E' - \imath\theta E' + \imath a\nabla^2 E' + E_i - C'|E'|^2E') \tag{1.86}$$

where we defined $C' = CA$ and we have dropped the vectorial notation for the fields.

Finally we define $t = 1/\gamma t'$, $x = \sqrt{a}x$, $y = \sqrt{a}y$ and $E_i = C'^{1/2}E_i$ to get the scaled equation

$$\frac{\partial E}{\partial t} = -(1+\imath\theta)E + \imath\nabla^2 E + E_i + \imath|E^2|E \tag{1.87}$$

To sum up, in this section we have obtained, through the mean-field approximation, a model that describes the dynamics of the slowly varying amplitude of the electromagnetic field $E(\vec{x},t)$ in the paraxial limit, where $\vec{x} = (x,y)$ is the plane transverse to the propagation direction z in which the slow dynamics takes

place. In the scaled variables, the first term in the right hand side of Eq. (1.87) describes cavity losses (making the system dissipative), E_i is the input field, θ the cavity detuning with respect to E_0, and $\nabla^2 = \partial^2/\partial x^2 + \partial^2/\partial y^2$ is the transverse Laplacian modeling the diffraction. The sign of the cubic term indicates the so called self-focusing case.

Part I

Image and Data Processing with Nonlinear PDE

Chapter 2

Image Processing Using Type II SHG

In Sect. 1.6 we derived the model for a cavity containing a Second Harmonic Generation (SHG) crystal in type II phase matching configuration. In this chapter we will show that this system can be used to perform several image processing tasks such as frequency transfer, contour recognition, contrast enhancement and noise filtering.

First we will show how this processing scheme can be implemented in a cavity with planar mirrors, described by Eqs. (1.52-1.54). This constitutes an example that allows to develop a deep understanding on how the image processing scheme works, but is hard to implement experimentally because planar cavities are extremely difficult to align. With this in mind, in Section 2.2 we will introduce modifications to this equations to describe a cavity with spherical mirrors, and we will show how the image processing scheme is also possible in this case with slight changes.

2.1 Image Processing in a Planar Cavity

To achieve the image processing in this system we pump it with an image coded as the spatial intensity modulation of the field linearly polarized in the y direction E_o, along with an homogeneous field E_e linearly polarized in the x direction, as shown in Fig. 2.1. The intracavity fundamental fields A_o, A_e and

the second harmonic field B will show as a spatial modulation of their intensity the different processes over the input image. The fields outside the cavity are directly proportional to the intracavity fields, therefore we will focus only in the dynamics of the later ones.

To describe the different image processing operations that are possible in this system we will first study the homogeneous stationary solutions of Eqs. (1.52-1.54). For homogeneous pump, a change in the phase of the input fields $E_o \rightarrow E_o e^{\phi_o}$, $E_e \rightarrow E_e e^{\phi_e}$ leads to the same homogeneous stationary solutions, with a change in the phase: $A_o \rightarrow A_o e^{\phi_o}$, $A_e \rightarrow A_e e^{\phi_e}$ and $B \rightarrow B e^{\phi_o + \phi_e}$. Therefore, to compute the homogeneous solutions we consider the pump fields E_o and E_e as as real fields without loss of generality. First we consider, Eqs. (1.52-1.54) for the case of symmetrical pumping $E_o = E_e$, which maximizes the production of second harmonic. In this case, the homogeneous stationary solution for the fundamental fields A_o and A_e can be derived [133–136, 142]:

$$(1 + \delta_A^2 - \frac{|A_e|^2 |A_o|^2}{1 + \delta_B})(|A_o|^2 - |A_e|^2) = 0 \tag{2.1}$$

Eq. (2.1) admits a symmetric solution with $|A_o| = |A_e|$ and an asymmetric solution as shown in Fig. 2.2. The homogeneous symmetric stationary steady state becomes unstable for a pump above the critical value:

$$E_{as}^2 = 2(1 + \delta_B^2)^{1/2}(1 + \delta_A^2)^{3/2} + 2(1 + \delta_A^2)(1 - \delta_A \delta_B).$$

The system evolves to the asymmetric homogeneous solution for with $|A_o|^2 |A_e|^2 = (1 + \delta_A^2)(1 + \delta_B^2)$, therefore the intracavity field polarization is no longer the same as the pump (polarization instability). Because of the symmetry of the pump, two different equivalent states can exist, one with a large value of $|A_o|$ and a low value of $|A_e|$ and the opposite one [133, 134, 143].

We now consider the case of two homogeneous pump fields E_o and E_e but with different amplitudes . In this case the homogeneous stationary solutions for $|A_e|$ are given by the solution of the polynomial

$$\begin{aligned} \Delta_A |A_e|^{10} + [4(1 - \delta_B)\Delta_A - E_e^2]|A_e|^8 + 2[\Delta_A Q + \Delta_{AB}(E_o^2 - 2E_e^2)]|A_e|^6 \\ +2\{2\Delta_A^2 \Delta_B^2 \Delta_{AB} - Q E_e^2 - 2\Delta_{AB}^2 E_o^2\}|A_e|^4 + [\Delta_A^3 \Delta_B^2 + \\ 2\Delta_A \Delta_B \Delta_{AB}(E_o^2 - 2E_e^2)]|A_e|^2 - \Delta_A^2 \Delta_B^2 E_e^2 = 0. \end{aligned}$$

where $\Delta_A = 1 + \delta_A^2$, $\Delta_B = 1 + \delta_B^2$, $\Delta_{AB} = 1 - \delta_A \delta_B$ and $Q = (\delta_A + \delta_B)^2 + 3\Delta_{AB}^2$. Once $|A_e|$ is known, $|A_o|$ and $|B|$ are given by

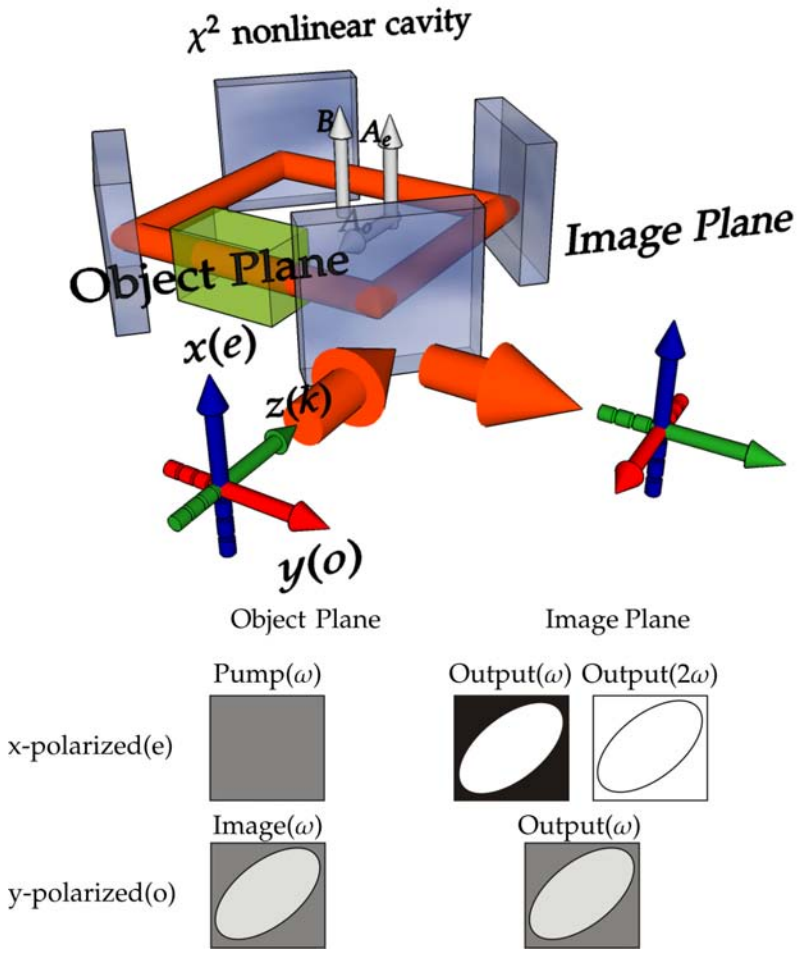

Figure 2.1: Image processing by Second Harmonic Generation. The image is inserted in the y-polarized field along with an homogeneous x-polarized field. The image processing occurs inside the cavity (represented by the gray prism) and the processed images are obtained in the fundamental fields $|A_o|$ and $|A_e|$ and in the second harmonic field $|B|$.

$$|A_o|^2 = \frac{\Delta_B E_o^2}{|A_e|^2 + 2\Delta_{AB}|A_e| + \Delta_A\Delta_B}$$
$$|B|^2 = \frac{|A_o|^2|A_e|^2}{\Delta_B}$$

Fig. 2.3 shows the typical dependence of the homogeneous stationary solutions for the intracavity fields $|A_o|$, $|A_e|$ and $|B|$ on E_o when E_e is fixed to a given value, in this case $E_e = 5$. For small E_o, the functions $A_o(E_o)$ and $B(E_o)$ take small values while $A_e(E_o)$ is large and close to $E_e/(1 + i\delta_A)$. All of them are single valued. When E_o approaches E_e the system becomes bistable, with two stable branches connected by an unstable one, in the case of $A_o(E_o)$ and $A_e(E_o)$, and a loop for $B(E_o)$. For large E_o all the functions become again single valued but now $A_o(E_o) \gg A_e(E_o)$. The existence of three steady-state solutions of Eqs. (1.52-1.54) in a region of finite width centered on $E_o = E_e$ is closely related to the polarization

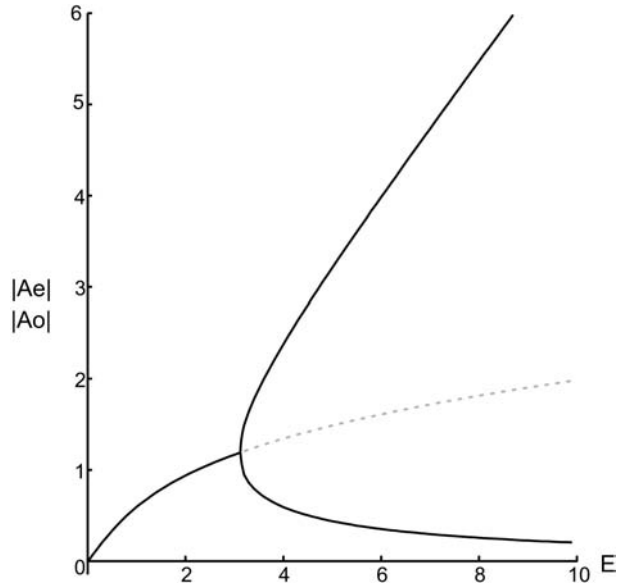

Figure 2.2: Steady states for second harmonic generation with asymmetric homogeneous pumping. We plot the stationary amplitude of the intracavity fundamental fields for homogeneous asymmetric pumping E ($\delta_B = 0$, $\delta_A = 1$).

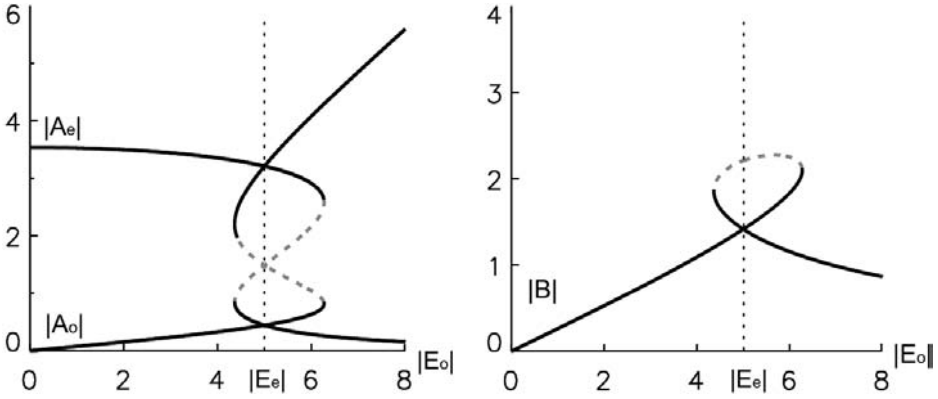

Figure 2.3: Steady states for second harmonic generation with asymmetric homogeneous pumping. We plot the stationary amplitude of the intracavity fields for homogeneous asymmetric pumping as a function of E_o for $E_e = 5$ ($\delta_B = 0$, $\delta_A = 1$, and $E_{as} = 3.10755$).

instability occurring in the symmetrical pumping case. If fact, this S shape can be observed only if $E_e > E_{as}$.

Now that we know the homogeneous stationary solutions of the equations as a function of the pump we can consider the effects produced on an image inserted in the system as spatial variations in the intensity of the x-polarized pump field along with an homogeneous pump E_e. Tuning the amplitude of the homogeneous pump it is possible to achieve different operations over the image. First we show the simplest case in which the image can be transferred from the fundamental to the second harmonic. Then we show how it is possible to enhance the contrast and to detect the contour of the image [143]. In this same case we will also use the system to filter noise added to the image. For simplicity E_o and E_e are taken as real fields except when noise is considered.

2.1.1 Frequency transfer

Lets consider the injection of a very simple 1-dimensional image in which the amplitude of the ordinary polarized signal $E_o(x)$ takes only two real values E_0 and E_1 along the transverse coordinate x, as shown in Fig. 2.4 ($E_e > E_1 > E_0$). In the zones of the image where the details are much larger than the diffraction length (i.e. far from the edges) the intracavity fields $A_{o,e}(x)$ and $B(x)$ tend to take

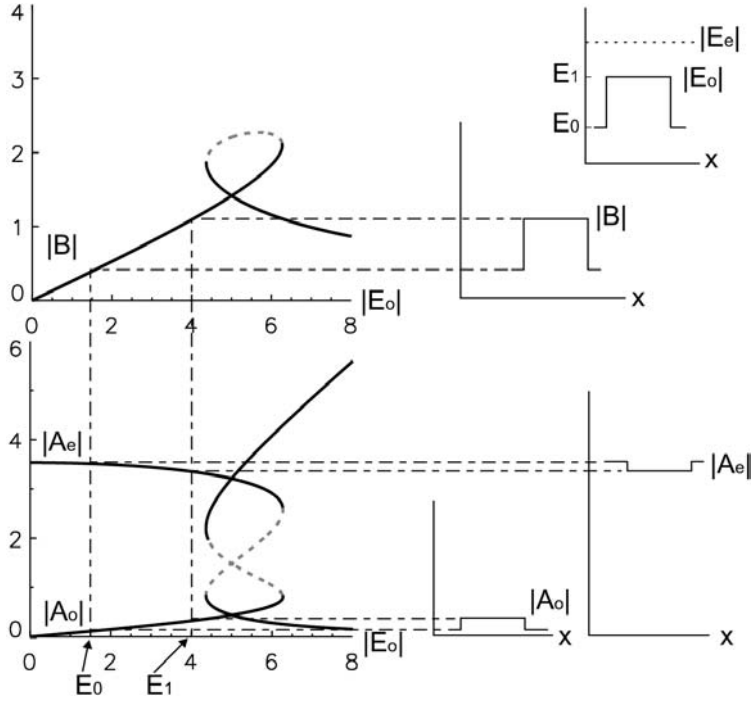

Figure 2.4: Geometrical construction to illustrate the frequency transfer regime. On the left we plot the stationary amplitude of the intracavity fields for homogeneous asymmetric pumping as a function of E_o for $E_e = 5$ ($\delta_B = 0$, $\delta_A = 1$, and $E_{as} = 3.10755$). On the right we plot the response of the system to a simple image (sketched on the far right) where E_o takes only the values E_0 and E_1 with $E_0 < E_1 < E_e$.

the stationary values shown in Fig. 2.4 corresponding to homogeneous pumps of amplitude E_0 and E_1.

As sketched in Fig. 2.4, for $E_o \ll E_e$, A_o is almost a linear function of E_o, therefore, A_o reproduces the spatial distribution of the input image E_o. Following a similar argument, we can see that the extraordinary polarized intracavity field A_e shows the negative of the input image. More important, since the second harmonic field B behaves also almost linearly with E_o, the the image in the fundamental field is reproduced in the second harmonic. Furthermore since B is extraordinary polarized, for an ordinary polarized input image there is also a polarization transfer. While Fig. 2.4 is just a convenient geometrical construction, the results

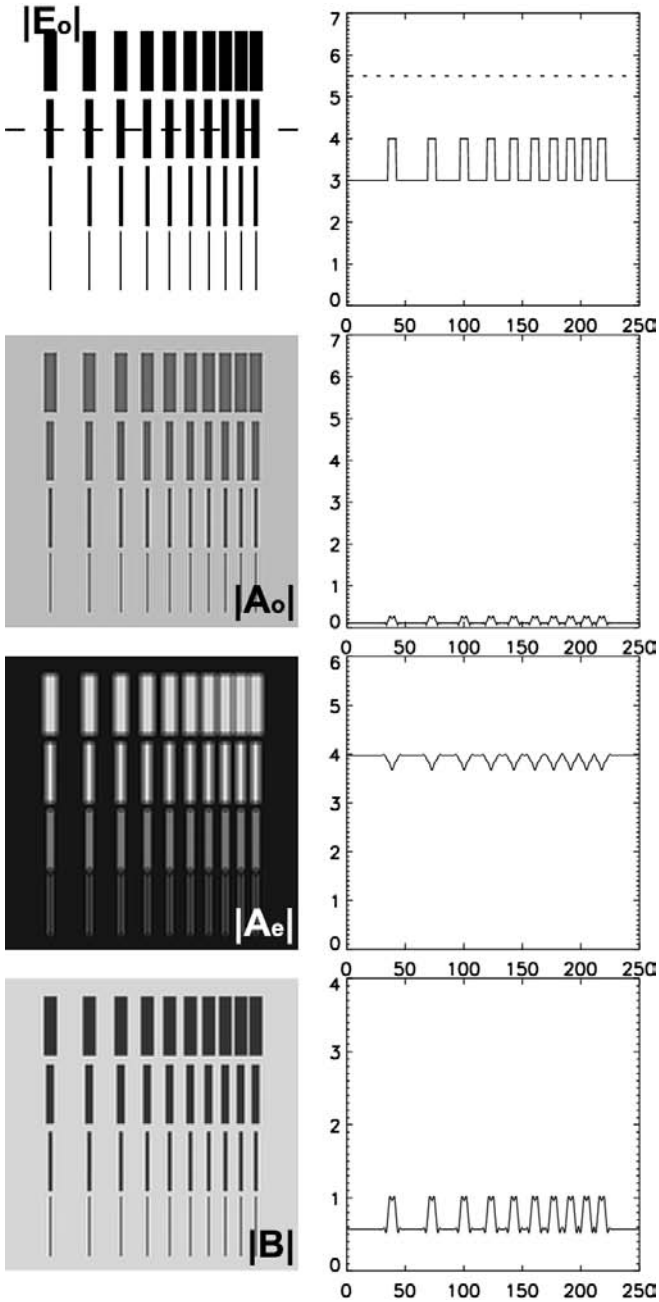

Figure 2.5: Frequency transfer. The left column shows (from top to bottom) the spatial distribution of amplitude input field E_o, and the amplitude of the intracavity fields $|A_o|$, $|A_e|$ and $|B|$. In all the figures of this chapter, except if otherwise noted, the grey scale of goes from the minimum (white) to the maximum (black) of each field. The right column shows a transversal cut of the fields along the dashed line on the top left panel. We have considered $E_e = 5.5$ (shown as dashed line on the top right panel).

obtained from numerical integration of the full model, including the effects of diffraction are in excellent agreement with it. We integrated Eqs. (1.52-1.54) following the procedure described in Appendix A. Fig. 2.5 shows the result of processing a 2d-image, where an image of constant amplitude 1 is put on top of a plane wave background with amplitude $E_o = 3$. In this image can be seen that as an effect of the diffraction the edges of the image are smothered out. Nevertheless the image is quite well reproduced as seen in Fig. 2.5. We are considering here a system with a transverse size of 256 diffraction units. Diffraction sets the effective minimum scale for which details are going to be resolved. Therefore the size of the system as compared to the diffraction length can be considered as an effective pixel number. In out sample image the largest rectangles are 11 pixels wide with separations ranging from 24 to 1 pixels, and smallest are 1 pixel wide.

2.1.2 Contrast enhancement and contour recognition

Let us consider again the simple 1-d image where E_o takes only two values E_0 and E_1 along the transverse coordinate but now the lower value E_0 is below E_e while the higher value E_1 is above, as shown in Fig. 2.6 ($E_1 > E_e > E_0$). In this case the multivalued dependence of $A_o(E_o)$, $A_e(E_o)$ and $B(E_o)$ comes into play. If the selected value E_1 is above the bistability region and E_0 is below it, $A_o(E_o(x))$ has to jump from the lower to the upper branch of the hysteresis cycle, while $A_e(E_o(x))$ has to jump from the upper to the lower branch. This will give rise to a sharp spatial variation of A_o and A_e. In fact for vanishing intracavity fields as initial condition, it is not necessary to fully cross the hysteresis cycle to have a jump. With those initial conditions where $E_o < E_e$ the system locally selects the steady state solution with small value for $|A_o|$ and a large value for $|A_e|$, while it selects the steady state solution with a large value for $|A_o|$ and a small value for $|A_e|$ where $E_o > E_e$. Therefore, E_e plays in fact the role of an effective threshold and the jump already occurs if E_o crosses E_e as sketched in Fig. 2.6. In the region where $E_o(x)$ is larger than E_e, $|A_o|$ has a large value compared with the zones where $E_o(x) < E_e$; so the contrast enhanced (Fig. 2.6). The amplitude $|A_e|$ takes lower values where $E_o < E_e$ so the image in this field is inverted with respect to the input, and is also contrast enhanced (Fig. 2.6). At the border between the regions $E_o > E_e$ and $E_o < E_e$ the second harmonic field B displays a sharp peak, as can be seen from Fig. 2.6, the values of B for E_0 and E_1 are similar, but this two regions must be connected by the high intensity solution in the middle of the loop. Therefore the second harmonic field displays the contour of the input image (Fig. 2.6).

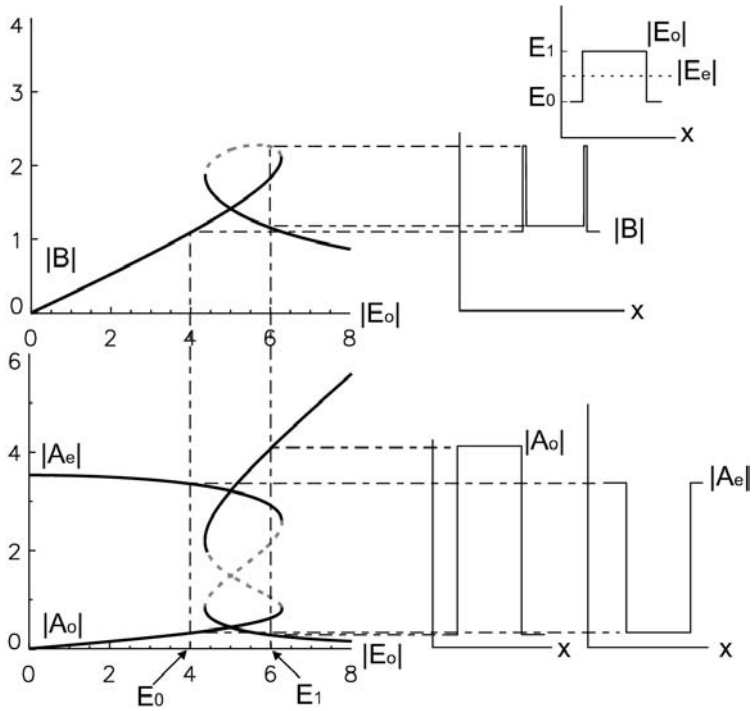

Figure 2.6: Geometrical construction to illustrate the contrast enhancement and contour recognition regime similar to Fig. 2.4 but with $E_0 < E_e < E_1$.

This processing effects are shown for two dimensional image in Fig. 2.7. The first row shows the original image E_o, which have a contrast of 1 in arbitrary units. In the second row the contrast enhanced image $|A_o|$ is shown. In this image can be seen that the contrast was amplified about 3 times from the original image. This same amount of contrast amplification is achieved for the negative image $|A_e|$ shown in the third row of Fig. 2.7. Finally, the fourth row of Fig. 2.7 shows the contour of the original image. We can see from this image that the system is able to resolve two edges separated by two pixels, so it is not able to resolve the contour of the last row of lines. This contour is displayed with a contrast that is about half the contrast of the original image.

Analyzing Fig. 2.6 in detail can be seen that $|A_o|$ grows almost linearly with E_o with a slope of about 1 in the upper branch, therefore there is almost no improvement in the contrast amplification factor by changing the value of E_1. Due to the shape of the lower branch of $|A_o|$, if we decrease the value of E_0 the contrast amplification ratio also decreases, since for a large variation of E_0 there is a very small variation of $|A_o|$, i.e., the original image will have more contrast, but the processed image but the contrast of the processed image will remain barely the same. Even more, for a very small value of E_o we can get a decrease in the contrast of the processed image with respect to the original one. From this, can be concluded that the highest contrast amplification factor is achieved when the background level of the input image (E_0) is near to the value of E_e.

It should be emphasized that the previous results show that for a given image different processing capabilities are possible tuning the amplitude of the homogeneous field E_e. This is even more interesting when considering images which are composed of many levels of intensity, as in a grey scale image. In that sense, if the homogeneous pump E_e is set to a value larger than E_o for all the points of the image then the frequency transfer process will take place and the whole image will be displayed by the second harmonic frequency field B. If E_e is decreased, then the parts of the image where $E_o > E_e$ will undergo a contrast enhancement process. As illustrated in Fig. 2.8 for a 2-dimensional image the intracavity field $|A_o|$ is largely enhanced in these spatial regions. Simultaneously the amplitude of the second harmonic field $|B|$ shows the contour of the region whose contrast has been enhanced. The amplitude of the homogeneous pump acts as a tunable reference level and placing it at different values allows for the selective enhancement (and selective contour detection) of different parts of the figure (see Fig. 2.8). Even more, if instead of using an homogeneous field E_e, we can use it as a kind of "mask" to selectively enhance the contrast of some parts of the image, by using different values of E_e for each region.

At this point is convenient to differentiate between the edge enhancement procedure [26, 144, 145] and this effect called here contour recognition: while in the

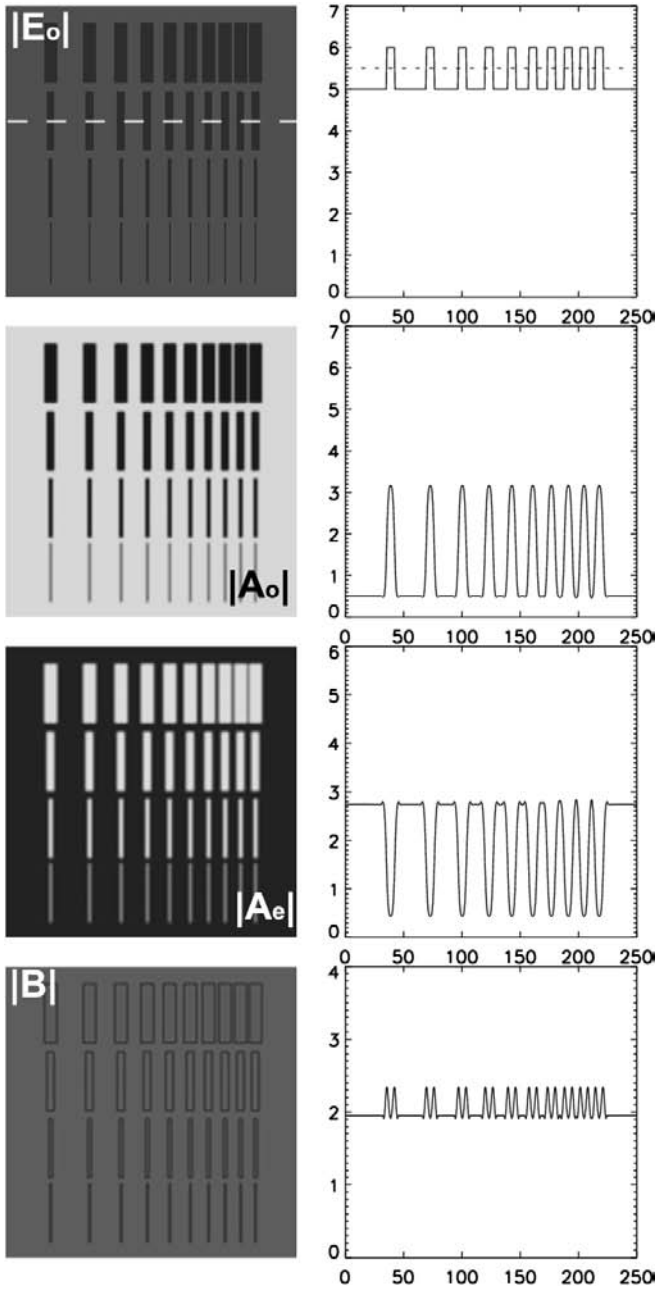

Figure 2.7: Contrast enhancement and contour recognition.

first procedure the edges of the whole image are enhanced in the second we have a contour level curve similar somehow to those of altitude maps where E_e sets the altitude level.

2.1.3 Noise filtering

Another interesting property of this system is its ability to filter out noise from the processed image. This noise filtering effect arises from an interplay between the diffraction an the nonlinearity which filter out all the high spatial frequency components of the input image. Therefore the small scale fluctuations associated to noise are effectively removed [143]. This effect appears both in the frequency transfer and in the contrast enhancement regimes as is shown in Figs. 2.9 and 2.10. In these figures the image has been superimposed with a complex random field, yielding a noisy image both in intensity and phase. The figures also show that the noise filtering effect is more effective in the contrast enhancement regime, since in this regime the nonlinearities play a more important role, and the interplay between nonlinearity and diffraction is what produces the desired effect, and not only the diffraction. To quantify the noise filtering degree, for images in which the intensity takes only two values we define the signal to noise ratio (SNR) of the image as:

$$SNR = \frac{\mu_{img} - \mu_{bkg}}{\sigma_{img}} \tag{2.2}$$

where μ_{img} and μ_{bkg} are mean values of the high level intensity of the image and the background respectively and σ_{img} is the standard deviation computed at the high level intensity regions of the image. Therefore, the SNR measures the ratio between the contrast of the image and the standard deviation of noise. Now, the SNR of the input image E_o both for Figs. 2.9 and 2.10 is 3.46. In the frequency transfer regime, the SNR of the image transferred to the second harmonic ($|B|$) is 13.62, that is an improvement of almost 4 times the original SNR. In the contrast enhancement regime we look at the SNR of the enhanced image $|A_o|$, since in the second harmonic we have the contour of the original image. The SNR of $|A_o|$ in this case is 12.36, also an improvement of almost 4 times the SNR. But in this second case there is also an improvement of the contrast of the image that gives it a much better visibility above the background noise.

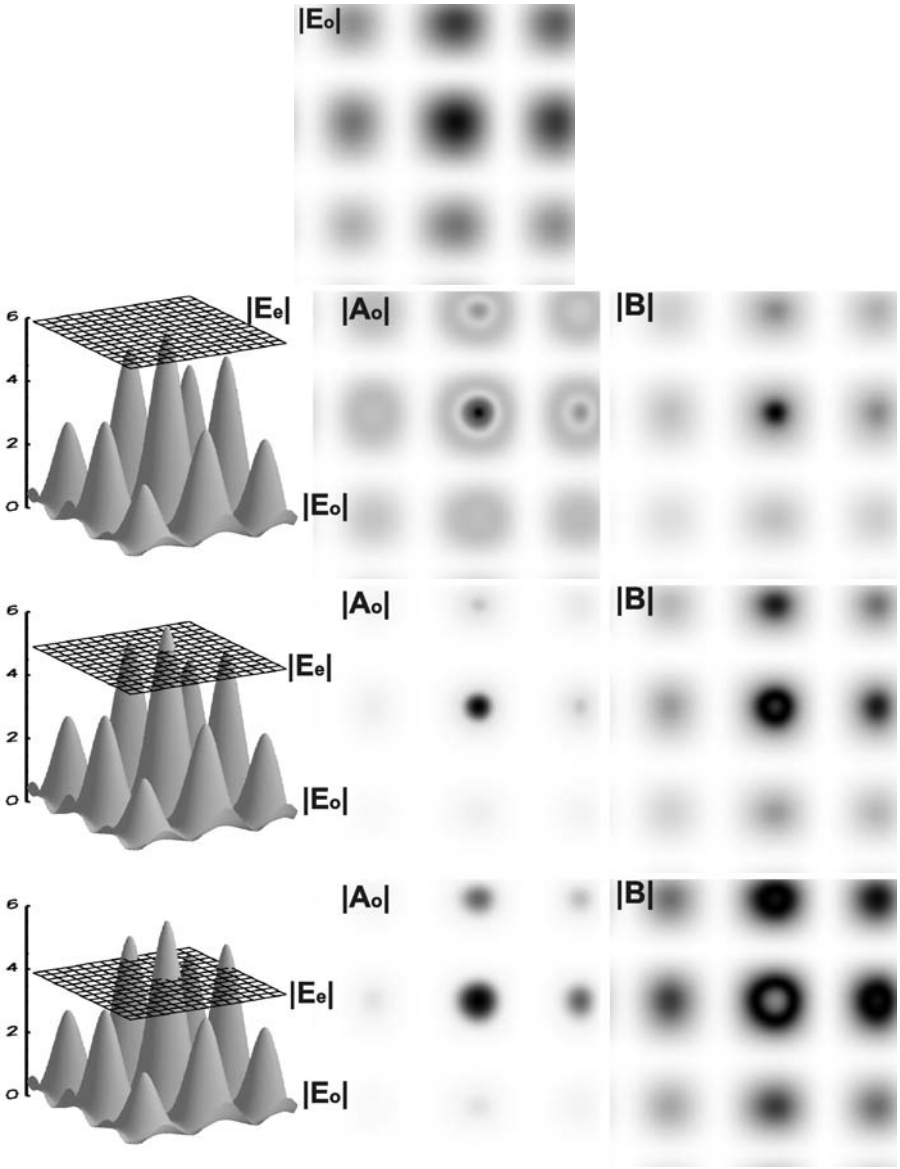

Figure 2.8: Scanning of a 2 dimensional grey scale image shown at the top. The left column shows a 3D plot of the input image E_o and the homogeneous field E_e plotted as a regular grid. The central column shows the amplitude of the intracavity field $|A_o|$, and the right column shows $|B|$. From top to bottom E_e takes the values 6, 5 and 4.

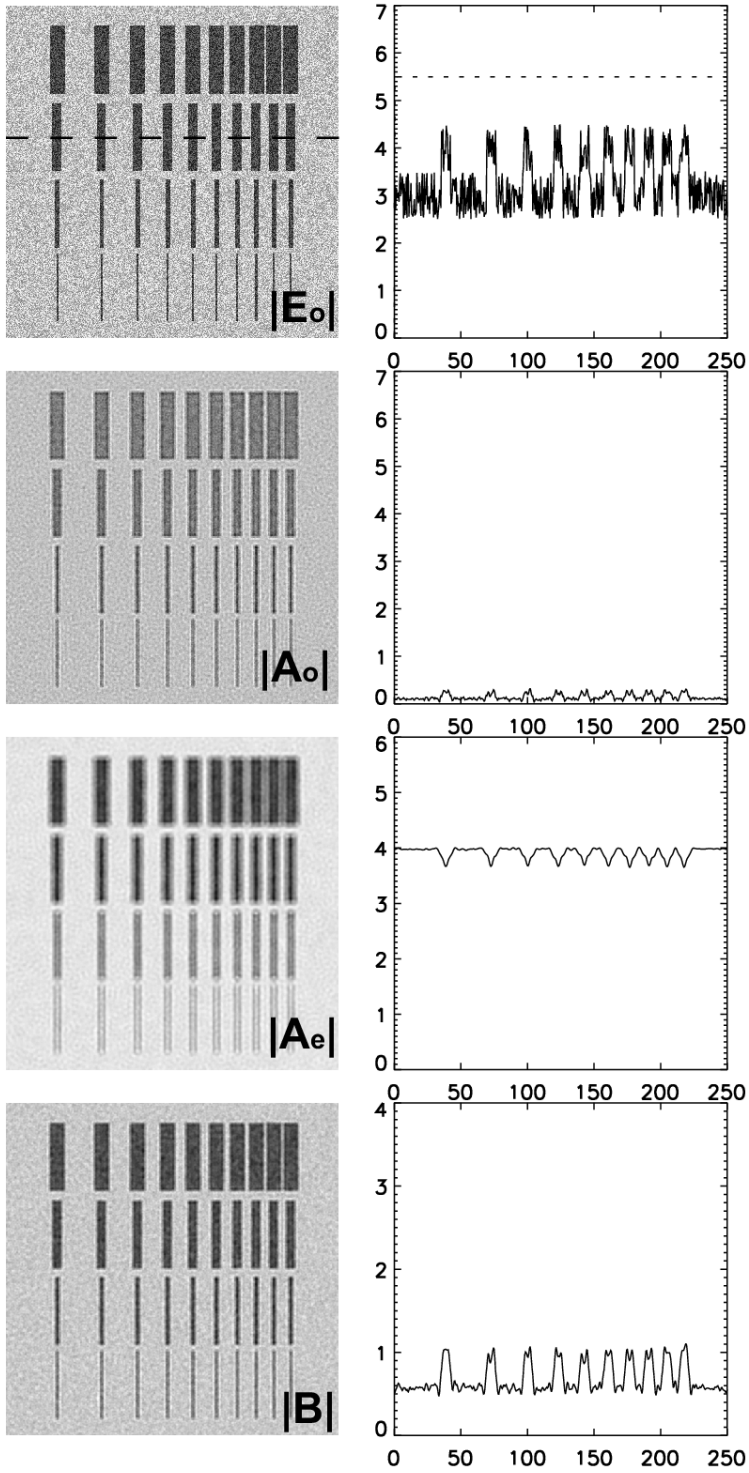

Figure 2.9: Noise filtering in the frequency transfer regime.

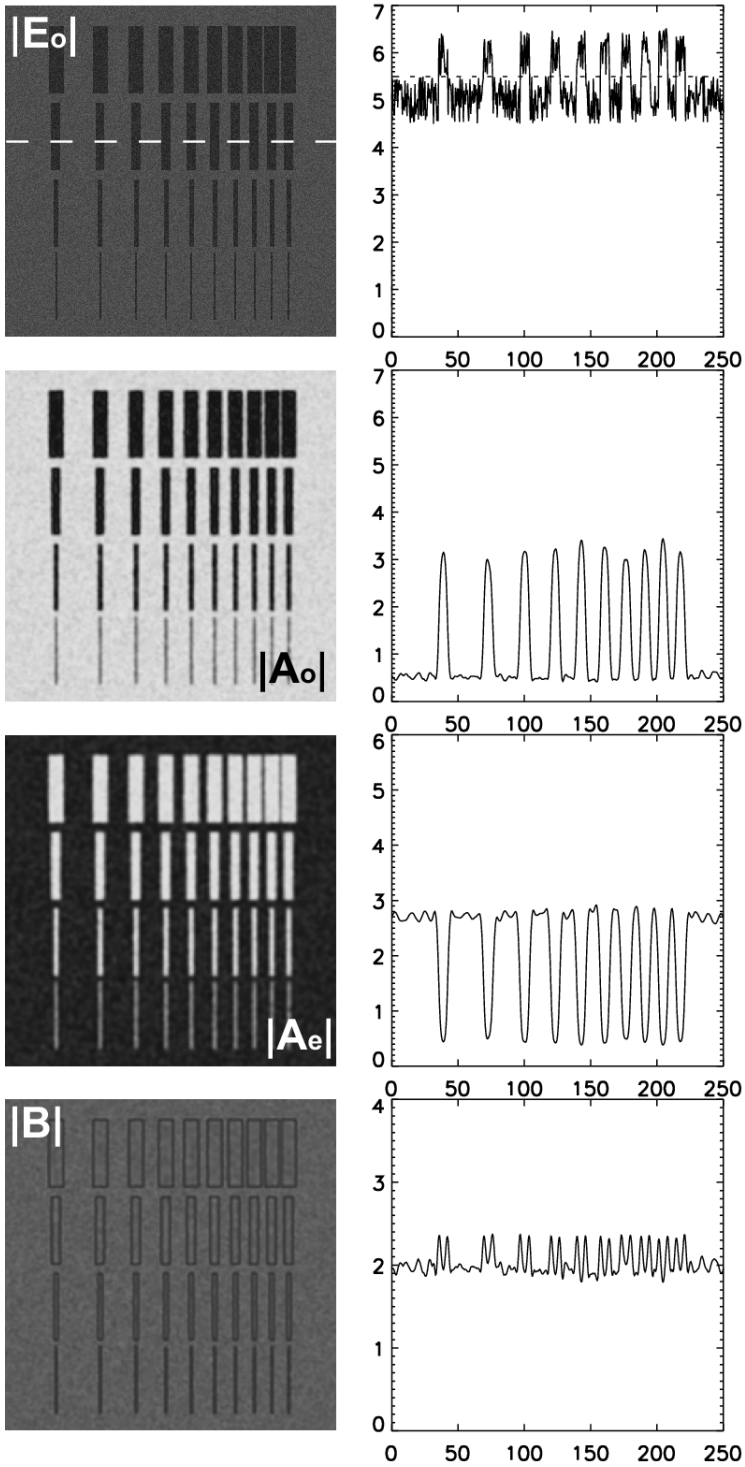

Figure 2.10: Noise filtering in the contrast enhancement regime.

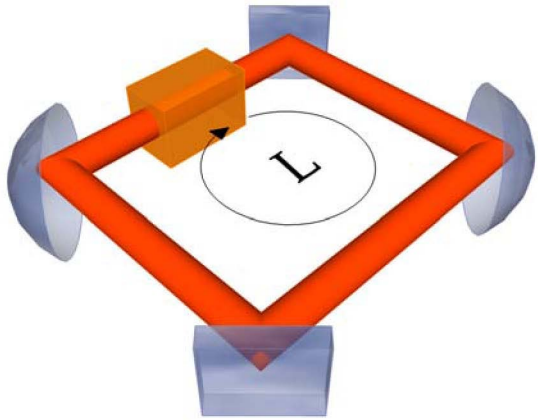

Figure 2.11: Sketch of a confocal ring cavity with a nonlinear medium. The radii of curvature of the two semi-spherical mirrors is equal to $L/2$, half the length of the cavity (the sketch is not at scale).

2.2 Cavities with spherical mirrors

The previous section dealt with the ideal case of a cavity with plane and infinite mirrors. Even considering finite mirrors, planar cavities are difficult to realize experimentally since they are prone to instabilities. Cavities with spherical mirrors are more stable and a commonly used experimentally, but from a fundamental point of view, the introduction of curved mirrors breaks the translational invariance, which is an inconvenient for the processing of an image. Spatial points of the image where the field takes the same value and which would otherwise be treated in the same way are now treated differently if they are located at different distances from the optical axis.

We consider now a model for a cavity with spherical mirrors based in the model given in Ref. [146] for an Optical Parametric Oscillator. The deduction of this model is similar to the one already described in Chapter 1 for plane mirrors. The difference is that when taking the mean field approximation the field inside the cavity is not decomposed in Fourier modes but in Gauss-Laguerre modes, that are compatible with the geometry of the system. This gives a modified version of Eqs. (1.52-1.54), which have some additional terms that take into account the geometry of the mirrors:

$$\begin{aligned}
\partial_t B(r,\phi,t) &= -(k_B + \imath\delta_B - \imath\xi L_B)B(r,\phi,t) \qquad (2.3)\\
&\quad -\chi A_o(r,\phi,t)A_e(r,\phi,t)\\
\partial_t A_o(r,\phi,t) &= -(k_A + \imath\delta_A - \imath\xi L_A)A_o(r,\phi,t) \qquad (2.4)\\
&\quad +\chi A_e^*(r,\phi,t)B(r,\phi,t) + E_o(r,\phi,t)\\
\partial_t A_e(r,\phi,t) &= -(k_A + \imath\delta_A - \imath\xi L_A)A_e(r,\phi,t) \qquad (2.5)\\
&\quad +\chi A_o^*(r,\phi,t)B(r,\phi,t) + E_e(r,\phi,t)
\end{aligned}$$

Where we chosen to write the fields in polar coordinates, which seem to be the best option due to the geometry of the cavity. χ is the nonlinear coupling strength, ξ is the effective transverse mode spacing, k_A and k_B are cavity linewidths for the fundamental and second harmonic fields and δ_A and δ_B are the respective detunings.

The effect of diffraction and the geometry of the cavity are taken in account by the differential operator [146]

$$L_k = \frac{W_k^2}{4}\nabla_\perp^2 - \frac{r^2}{W_k^2} + 1\,, \qquad k = A, B \qquad (2.6)$$

where $W_k = \sqrt{(2z_r c)/\omega_k}$ is the minimum waist of the intracavity fields, z_r is the common Rayleigh length of the three fields, c the speed of the light and $\nabla_\perp$ the transverse Laplacian. The first term of Eq. (2.6) models diffraction in the paraxial approximation while the r^2 term comes from the curvature of the mirrors. The last term adds an effective contribution to the detuning which depends on the mode spacing ξ. If we now consider the case in which $\xi \to 0$ while $W_k \to \infty$ in such a way that the product ξW_k^2 converges to a finite value. The diffraction term in Eq. (2.6) remains finite while the term associated with the mirror's curvature term vanishes; so that case corresponds to an ideal planar cavity. Rescaling $\chi A_e \to A_e$, $\chi A_o \to A_o$, $\chi B \to B$, $\chi E_e \to E_e$, $\chi E_o \to E_o$ and $\frac{\xi W_A^2}{4}\nabla_T^2 \to \nabla_T^2$; and taking $k_A = k_B = 1$ we recover Eqs. (1.52-1.54) for a planar cavity.

We now chose the parameters such that they describe a cavity in quasi-confocal configuration [146]: $\delta_A = 1$, $\delta_B = 0$, $\xi = 0.005$, $W_A^2 = 1$ and $W_B^2 = 0.5$. A confocal cavity is one in which the radius of the mirror are equal to the separation between them, as shown in Fig. 2.11. A quasi-confocal cavity is a cavity near this configuration, where the distance between the mirrors is nearly the radius of them.

Due to the geometry of the cavity the pump fields have to decay to zero when $r \to \infty$. We consider a super-Gaussian field which has a large plateau around

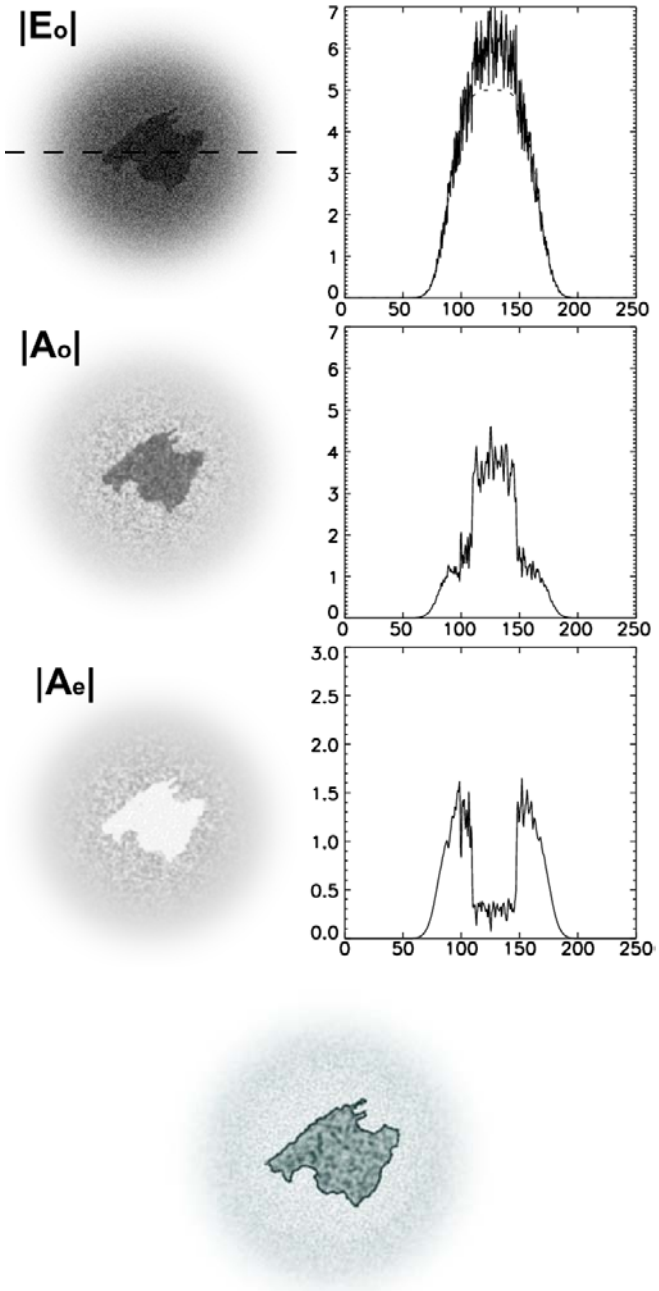

Figure 2.12: Contrast enhancement and contour recognition in a quasi-confocal cavity. The left column shows (from top to bottom) the spatial distribution of $|E_o|$, $|A_o|$ and $|A_e|$. In the top right the dashed line shows the profile of E_e and it is covered by E_o in the rest of the figure. The bottom row shows the spatial distribution of B, where the contour of the image is displayed.

the optical axis where we can superimpose the image. The pump fields are: $E_e(r,\phi) = E_{0e}exp(-r^4/w_e^2)$, and $E_o(r,\phi) = I(r,\phi) + E_{0o}exp(-r^4/w_e^2)$, where $w_e = 300$ and $I(r,\phi)$ is an image as it has been considered in the planar cavity case. The input intensity levels are chosen such that they correspond to a regime where nonlinear effects are important.

While the simple geometrical construction used in the previous chapter can not be directly applied here, since there are no homogeneous steady state solutions, we found numerically that the amplitude of the extraordinary polarized super-Gaussian field plays again the role of setting a reference level. If $|E_o| < |E_e|$, then a (weak) image is transferred to the second harmonic. This corresponds to the frequency transfer regime.

Since the aim of this section is just to show that the same operations that can be done in a planar cavity can be also done in a cavity with spherical mirrors we will only illustrate the example of the contrast enhancement, and contour recognition regime with the addition of noise to show also the noise filtering properties. Eqs. (2.3-2.5) where integrated following the procedure described in Appendix A, where the r^2 term in L_k is computed along with the nonlinear term.

Contrast enhancement operation takes place in the part of the image where $|E_o| > |E_e|$ as before. This is illustrated in Fig. 2.12. The upper panels shows E_o for a 2d image inserted on top of a super-Gaussian with $E_{0o} = 5$ plus a complex random field. E_e is taken as a super-Gaussian with $E_{0e} = 5.5$. Due to the lack of an homogeneous background the definition of a contrast ratio is not straightforward as before, but in Fig. 2.12 can be easily seen that the contrast of the image is clearly enhanced. Therefore the same contrast-enhancement operation obtained with planar cavities can be performed in cavities with spherical mirrors. The fact that the image is inserted on top of a super-Gaussian field does not preclude any of the nonlinear operations since E_e is also a super-Gaussian. What really matters is the fact that locally the value of $|E_o|$ exceeds the value of E_e. The main restriction comes from the fact that to achieve nonlinear effects the image should be placed on the central part or the beam where the pump fields are strong enough.

As in the planar case, the contour recognition of the image above the reference level is displayed in $|B|$, this is shown in Fig. 2.12. Although now this contour is on top of a super-Gaussian beam, it is still clearly distinguishable.

Finally, as can be seen in Fig. 2.12, this system is also capable of noise filtering. As happen with the contrast ratio, the SNR is difficult to compute because of the super-gaussian background, but by comparing Figs. 2.12 and 2.10 can be seen that the noise filtering effect is smaller for cavities with spherical mirrors. This comes from the fact that the coefficient of the Laplacian term in Eq. (2.6), depends on the minimum waist of the intracavity fields and, for the configuration

considered here, this coefficient takes a lower value than in the planar mirror case.

2.3 Conclusions

In this chapter we have shown that intracavity second harmonic generation can be used for all-optical image processing. Operating in a linear regime it is possible to transfer an image from the fundamental to the second harmonic frequency. More important, by taking advantage of the system bistability it is possible to magnify the contrast in the fundamental field of any part of the image whose intensity is above a given reference level while simultaneously the second harmonic field displays the contour of the same part of the image. Furthermore, the reference level can be tuned allowing for a complete scan of the image. This system also displays interesting noise filtering properties. Another advantage of this scheme is that, for being founded in an all-optical process the image processing could be implemented in an optical cavity without need of a computer or having to digitalize the image. This reduces errors due to an imperfect calibration of the individual photodetectors as well as noise introduced by the measurement and discretization process, and subsequent electronic transmission. These effects, which deteriorate the image quality of the image before processing, are, in the all-optical case, absent or postponed to the very end of the information processing chain. Moreover, the resolution of this scheme is only limited by diffraction, and not by the number of pixels in the detection plane. And finally, the all-optical processing is intrinsically parallel, while image processing in computers is usually done in a serial way.

It is important to stress that all this image processing capabilities where shown both in planar cavities and in the situation of cavities with spherical mirrors, despite the fact that the translational symmetry is broken in the later case. The study of this effects in cavities with spherical mirrors aims to make this results easier to explore experimentally. Also, along this direction, we want to state that our theoretical calculations seems to be within accessible values of current SHG experiments [147]. For example with a 1-cm-long $KNbO_3$ crystal [143, 147], for the plane mirror case the typical pump field of $E_x = E_y = 5$ corresponds to an intensity $I = 860\text{kW/cm}^2$ yielding a power of $P = 1.56\text{W}$.

Is important also to notice that the processing scheme presented can be also achieved using other partial differential equations given that they share some of

the properties of the second harmonic generation model. This will be explored in the next chapters and applied to the processing of temporal data series.

Chapter 3

Detecting Change Points in Ecological Data Series

Is important to notice that the noise filtering and contrast enhancement scheme presented in Chapter 2 is quite independent of the particular details of the equations considered given that they present a bistable steady state similar to the one of Eqs. (1.52-1.54) for second harmonic generation. Even considering only one field the contrast enhancement and noise filtering operations could still be done, provided a bistable regime. This opens the possibility to implement similar processing schemes in simpler partial differential equations such as the Ginzburg Landau Equation (GLE) or in physical systems described by this equation.

One example in this direction is the possibility of using the one dimensional GLE to find changes in the mean value of temporal series [148]. Forcing the GLE with a data series, we will show that it is possible to filter noise and enhance the contrast of a signal, so it can be used to find change points in the data which are hidden because of the noise. In Chapter 4 we will show how this method can be also applied to decode chaos encrypted messages.

In this chapter we will introduce, in Sec. 3.1, the Ginzburg Landau Equation and we will show how the data processing scheme works. Then, in Sec. 3.2, we will illustrate examples on how the filtering process works on ecological time series to detect changes on its mean value.

3.1

The Ginzburg Landau Equation

The Ginzburg Landau Equation is an amplitude equation that describes the onset of an oscillatory instability in a wide variety of systems. Here, we will use this equation as an example of a reaction diffusion equation with a bistable steady state. As was already stated, the working principle of the filtering process is independent of the particular details of the equation, provided a diffusion (or diffraction as in Chapter 2) and a bistable steady state. We are not going to enter into the details of the deduction of the the GLE or in which systems arises. Literature on this equation (in particular on its complex version) is extensive and abundant, and the reader can refer to Refs. [149, 150] as a starting point. In one dimension, the forced GLE takes the following form:

$$\partial_t \psi(x) = a \cdot \partial_x^2 \psi(x) + \psi(x) - \psi(x)^3 + b \cdot h(x) \tag{3.1}$$

Where ψ is a real field, a is the diffusion constant and b is the forcing strength. In the following we set $b = 1$. $h(x)$ is a forcing term normalized between -0.5 and 0.5 . If we neglect $h(x)$ this equation has two stable homogeneous stationary solutions, $\psi_+ = 1$ and $\psi_- = -1$ (plus an instable solution at $\psi = 0$). Considering the forcing, tanking as initial condition $\psi(x) = h(x)$ and neglecting diffusion, in the places where $h(x) > 0$, the field will evolve to ψ_+, while where $h(x) < 0$ the field will evolve to ψ_-. If we now consider the effect of diffusion, those zones of size of the diffusion length (given by $1/a$) where the average of the field is greater than zero will approach to ψ_+, and those zones with average field lower than zero will approach to ψ_-. The diffusion will also wash out the fast spatial variations of the signal. Finally, the effect of the forcing term $h(x)$ is to change the basin of attraction of ψ_+ and ψ_-, favoring the separation mechanism and balancing the effect of diffusion.

Suppose now that we want to filter a temporal data series $P(t)$. In summary, the decoding mechanism works as follows: we identify the function $\tilde{P}(t) - r$ with $h(x)$, where r is a threshold parameter ($0 < h_0 < 1$) and $\tilde{P}(t)$ is the normalized $P(t)$. Starting from $h(x)$ as initial condition we let the equation evolve to the steady state. By properly tuning the diffusion strength a, the total effect of the process is to separate the zones (defined by the diffusion length) where the average of the signal is greater than r and the zones where the average is less than r, enhancing the contrast of the signal and filtering the noise, analogous to the second harmonic generation scheme. The selection of h_0 is arbitrary, and in analogy to what is shown in Fig. 2.8 for second harmonic generation, different

results are obtained with different values of the reference level. However, we expect that if there is a change point in the data series, then it will be a finite range of values of h_0 (those which are in between the mean value before and after the change point) for which the results will be similar. We will take this as the indication of the presence of a change point.

3.2 Time series of ecological data

In this section we will show how the GLE performs by filtering time series corresponding to ecological systems. The aim is to detect changes in the mean value of the series.

The filtering method shown here is an heuristic procedure to find those qualitative changes in the behavior of a system, by detecting changes on the mean value, that can be masked by noise. To make this filter easily available to the scientific community we developed the *Threshold Enhancer* application, available in Ref. [148]. Using this application it is possible to load the data series and apply the filtering procedure that will be described next.

3.2.1 Carpenter Model

Now we will consider data series obtained by integration of the Carpenter Model for lake eutrophication (enrichment of an ecosystem with chemical nutrients, typically compounds containing nitrogen or phosphorus) [151, 152] by excessive phosphorus:

$$\frac{dP}{dt} = l - sP + r\frac{P^q}{m^q + P^q} \tag{3.2}$$

where P is the amount of phosphorus in a water column, l is the rate of input from the watershed, and s is the rate of P loss per unit time. r is the maximum rate of recycling of P. The overall recycling rate is assumed to be a sigmoid function of P represented by the last term of Eq. (3.2). The exponent q ($q \geq 2$) affects the steepness of the sigmoid curve at the point of inflection. The value of P at which recycling reaches half the maximum rate is m.

Now we generate a time series where we linearly increase the value of l. The value of P increases steadily but at some point a threshold is reached and there is a

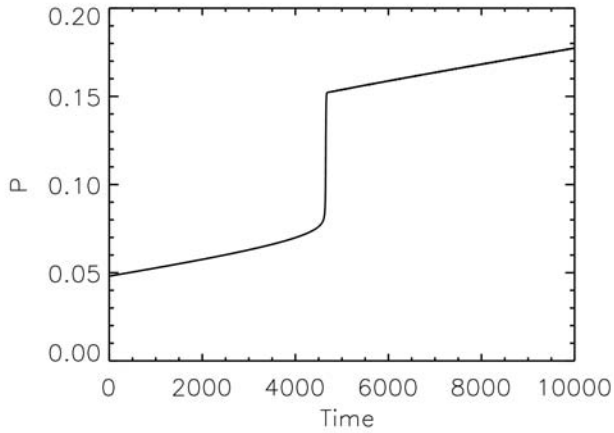

Figure 3.1: Time series generated by the Carpenter Model by linearly increasing l [152]. Both axis are in arbitrary units.

sudden increase in the value of P (Fig.3.1). Beyond this point P increases steadily again. At this point the increase of the amount of P can lead to eutrophication of the lake.

To simulate a real situation where the data is obtained from measurements in a real system we add to the data gaussian noise with an standard deviation equal to the amplitude of the jump that it contains (Fig. 3.2).

Now that we have the noisy data series to be processed we follow the procedure described in Sect. 3.1. The data series is normalized and used as $h(x)$ in Eq. (3.1). To begin with, we chose $h_0 = 0.3$, $a = 20$ and $b = 1$. Then we integrate the equation using the data series as the initial condition, and evolve it until it reaches an stationary point. This stationary solution is shown in Fig. 3.3, and as can be seen it recovers the change point present in the original data series.

Note that in order to solve the Eq. (3.1) boundary conditions need to be specified. Periodic boundary conditions are not appropriate for time series, like the one obtained for the Carpenter model, where a parameter of the system has been continually increased. The would neither be appropriate in time series with one or several jumps in the same direction, so that the final value is much larger or much smaller than the initial one. Another possibility for the boundary condition is to set the first derivative equal to zero at the boundaries, but this

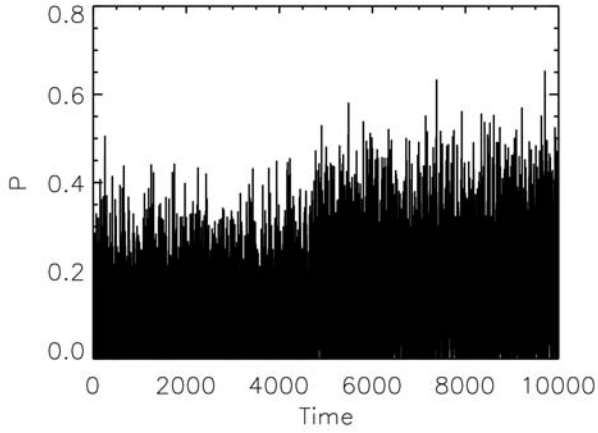

Figure 3.2: Same time series from Fig. 3.1 with added noise.

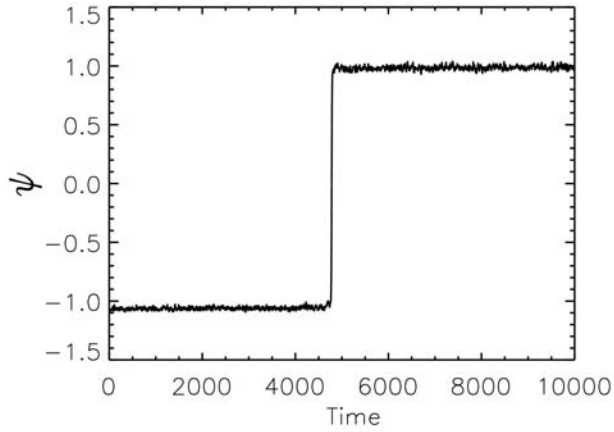

Figure 3.3: Filtered data corresponding to the noisy time series of Fig. 3.2. Both axis are in arbitrary units. Note that the units of ψ, although also arbitrary, are different from the units of P.

choice induces problems in the detection of change points if they occur close to the boundary, or if the data series has few points. We found that a good choice for the boundary conditions is to extend the data series at the beginning and the end by repeating a long string of points with a value equal to the average of the points close to the boundary, and then choosing a zero derivative condition at the new boundary. In this way our filtering method is less prone to create artifacts near the boundaries. In our case we have chosen to include at the beginning and at the end a string with a length of 10% of the total length of the series, and with a value equal to the mean value of the 10% first or last points in each case. In all the figures we only plot the points corresponding to the original time interval of the series and not the extended boundaries. The integration is done using a standard finite differences method.

In this case is easy to check that the processed data series recovers the original change point, since we had the noise free data to begin with. But in a real case the existence and localization of change points should be tested against the change of parameters Eq. (3.1), since the processing can lead to spurious detections. The more robust is a detected change points against change of parameters, the more likely to be a real feature of the data, and not and artifact of the filtering process.

The more relevant parameters for which variation should be tested are a and h_0, since they control how much the noise is averaged and which values of the series will converge to the upper or the lower fixed points, respectively. This is why we excluded variations of b from this discussion, since reasonable changes on this parameter do not produce relevant effects.

In order to determine the right time at which the change point occur we plot its position (in different colors) as a function of a and h_0, in Fig.3.4. In this figure it can be seen how the position of the detected change point moves if we change the parameters, but there is a large region of parameters where the position remains stationary. The change point detected using the parameters in the largest region is the most probable to be a real feature of the data at the right position, and is the one shown in Fig. 3.3 which is coincides with the change point in the original data series.

Despite that we do not have a rigorous mathematical way of determining the probability of a given change point to be real or spurious, this is a useful graphical method to validate the results obtained. Even though we want to stress that this method is not rigorous and can lead to false detections, that is why the results should be validated using other methods like the ones given in Chapter 1 and described in Refs. [41, 153–155].

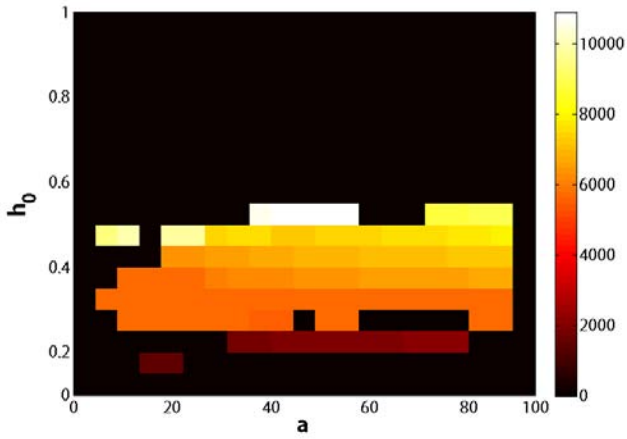

Figure 3.4: Position of the detected change points as a function of h_0 and a for the time series of 3.2. The color code indicates the position of the change point found. Black means that no change point is found for those parameter values.

3.2.2 Ringkøbing Fjord data

Ringkøbing Fjord is situated at the west coast of Denmark, and it covers about the 8% of its area. It has experienced several ecosystem changes due to variation in salinity and nutrient loading during the last 300 years.

In particular, to dilute the progressive eutrophication of the lagoon, an increased water exchange was established artificially. As a consequence, in the summer of 1995 a collapse occurred in the Fjord. The salinity reached the threshold that allowed the colonization of the lagoon with soft clamps and seed production of marine plants. Due to the colonization of the Fjord by high numbers of soft clamp the biomass of phytoplankton decreased to 5% of the former level. This is a by the book example of sudden regime shifts defining thresholds of the system, and that is why we have chosen this case to test the performance of the GLE filter against real data.

We will analyze two data series taken in the Fjord by that time, one corresponding to the Secchi depth, which measures the water transparency, and the other corresponding to the salinity in the Fjord (Fig. 3.5). In the Secchi data series the regime shift is quite obvious without further analysis, but things are no so clear

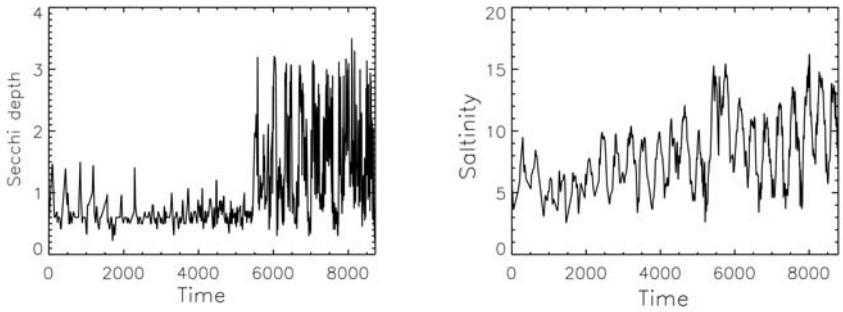

Figure 3.5: Left: Time series of the measured Secchi depth for the Ringkøbing Fjord. Right: Time series of the measured salinity for the Ringkøbing Fjord. The time is in days, and the y axis are in arbitrary units for both figures.

for the salinity. We will use this first series as an additional test to the filtering process.

As in the previous section we plot, for both time series, the position of the threshold in the filtered data versus a and h_0. This plots are shown in Fig. 3.6.

Now we pick the change point which is more stable against changes in the parameters for each time series. A time series for parameters in this region is plotted in Fig. 3.7. As can be seen, we recover the position of the regime shift for the Secchi depth that can be observed in the original data. In the case of salinity, the predicted position coincides with the position of the regime shift in the Secchi depth, as it should be. This is an additional test that shows that the filtering process is able to recover the position of regime shifts in time series, and that the right position of a change point is usually the one predicted by the largest region of parameters. However, we have to keep in mind that this is just an heuristic method.

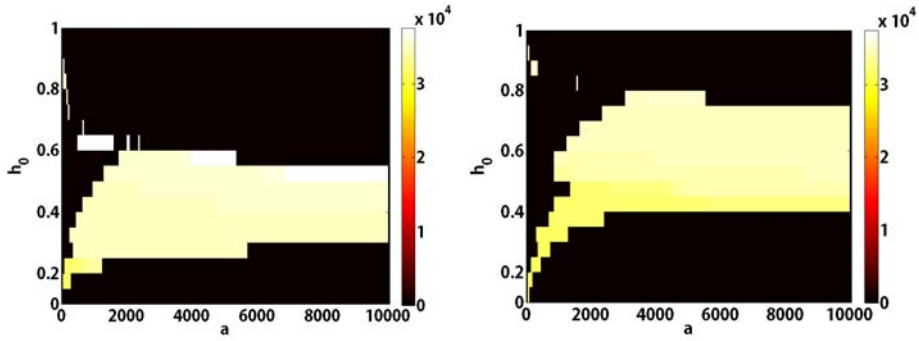

Figure 3.6: Left (right):Position of the detected change point as a function of h_0 and a for the time series of Secchi depth (salinity). The color code indicates the position of the change point found. Black means that no change point is found for those parameter values.

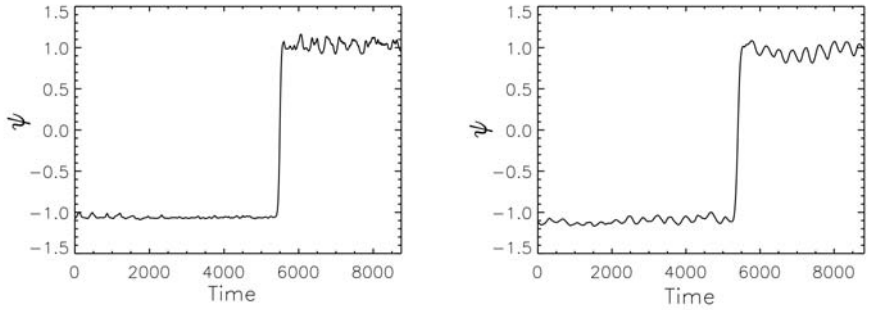

Figure 3.7: Left (rigth): Filtered data for the Secchi depth (salinity) with the most stable change point against change of parameters. Both axis are in arbitrary units. Note that the units of ψ, although also arbitrary, are different from the units of the Secchi depth (salinity).

3.3 Conclusions

In this chapter we have studied how the GLE can be used to filter ecological time series to detect changes on its mean value. This method relies on the bistability of the stationary solutions of the equation to split different regions of the data, as does the contrast enhancement method shown in Chapter 2. The bistability allows to differentiate regions (defined by the diffraction length) according to its mean value that can be otherwise masked by noise.

We applied this method to two different cases. The first one is a synthetic data series generated using the Carpenter model, to which we added noise. In this case we were able to recover the change point in the original series, and we showed a heuristic method to test the validity of the obtained result against the change of the parameters in the Ginzburg Landau Equation.

Then we analyzed real data from the Ringkøbing Fjord. In particular we have dealt with data of the salinity and the Secchi depth of the water. We where able to distinguish the position of the regime shift on the data, and the obtained results where self consistent. Using the position of the change point in the Secchi depth

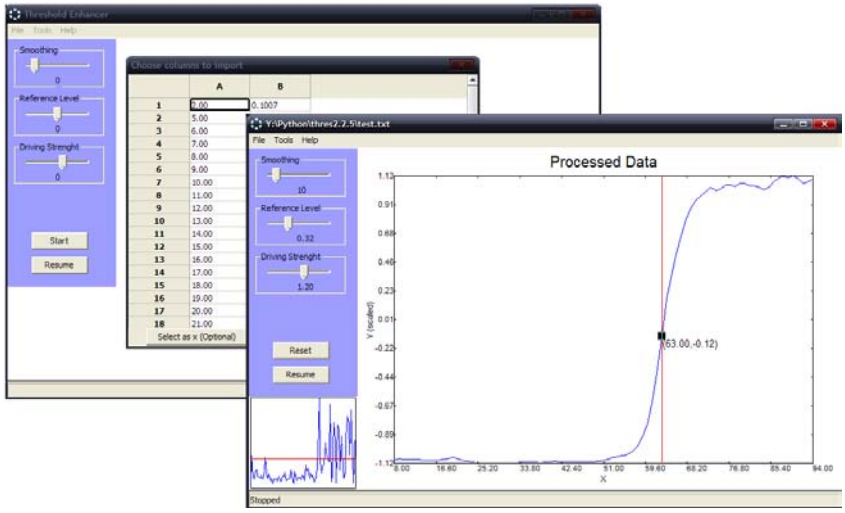

Figure 3.8: Screenshots of the Threshold Enhancer software. This software allows to search for change points using the GLE filtering method.

series as a reference (which can be easily spotted even in the unfiltered series) we found that in the filtered series the right position of the most stable against changes of the parameters of the GLE.

In summary, inspired by the ideas shown in Chapter 2 for the contrast enhancement process, we developed a method based on a simpler equation to find regime shifts in ecological data series. The use of a simpler equation has the advantage that allows to achieve similar results than those obtained with the second harmonic generation equations but using less computational power.

This method has the advantage to be a quick and simple way to process the data, using for example the software developed for with this purpose, that can be found in Ref. [148] (screenshots of this software are shown in Fig. 3.8. On the other hand, despite that we have given an heuristic method to check the results, a disadvantage of this method is that this test is not rigorous. Is also important to stress the actual interest on this type of filtering methods to detect regime shifts in ecological systems given the relevance that this field has taken in the last years.

In the next chapter we will show how this method can be also applied to filter time series of chaos encoded messages in order to decrypt the message.

Chapter 4

Decoding Chaos Encrypted Messages

In the previous chapter we described a method to filter time series and recover changes in the mean value of the data that are masked by noise. Another useful application of the GLE method is to recover messages encoded using chaotic communications. Some chaos encoding schemes codify the message in such a way that the mean value of the transmitted signal (carrier with the message) is different for bits “0" and bits “1". One can interpret that going from bit “0" to bit “1" or viceversa are change points which are masked by the chaotic carrier. Therefore, in principle, we can apply our detection method in this case. In Sec. 4.1 we will show a chaos encoding scheme that works in such a way and, in Sec. 4.2, how this messages can be decoded using our filtering method. Finally, in Sec. 4.3, we will introduce an alternative encoding method where the mean value of the signal is constant, and we will show how the filtering method is useless in this case.

4.1

Chaotic encoding scheme

Chaotic communications have become very popular in the past decade; during this period of time they have evolved from a theoretical concept to an almost ready-to-use technique where successful field experiments have been reported [156]. Out of the ever increasing number of schemes suggested to achieve secure chaos encoded communications, secure message transmission and recovery can

take place when two unidirectionally coupled semiconductor lasers synchronize. In such a system, the transmitted signal consists of a chaotic carrier generated by a semiconductor laser subject to optical feedback and an encrypted message, which can be encoded into the chaotic carrier in several ways [157]. Then, a system similar to the emitter needs to be placed at the authorized receiver side to recover the message.

In particular, a popular method to encode information is Chaos Modulation (CM)[157–160]. In this method, the message (perturbation) is codified by modulating the emitter's chaotic carrier power, according to the expression

$$P_t(t) = \Big(1 - \epsilon\, m(t)\Big) P_m(t), \tag{4.1}$$

where $P_t(t)$ is the transmitted signal, ϵ is the message modulation amplitude, $m(t)$ is the message being transmitted and $P_m(t)$ is the chaotic carrier. The message can be recovered by the authorized receiver as follows:

$$m'(t) = \frac{P_s(t) - P_t(t)}{\epsilon P_s(t)} \tag{4.2}$$

The extraction of the message depends on the quality of the synchronization between the emitter and receiver lasers. For $P_s(t) = P_m(t)$ (ideal synchronization) the message is perfectly recovered.

We model the dynamics of the semiconductor laser subject to optical feedback in terms of the Lang-Kobayashi equations [158, 161]. The equations for the slowly varying amplitude of the electric field $E(t)$ and the carrier number $N(t)$, assuming single mode operation and low to moderate feedback strengths, read

$$\dot{E}_{M,R}(t) = \frac{1+i\alpha}{2}\left[G_{M,R}(t) - \frac{1}{\tau_p}\right] E_{M,R}(t) + \gamma_{M,R} E_{M,R}(t-\tau) e^{-i\Phi} + \kappa_r E_M(t) \tag{4.3}$$

$$\dot{N}(t) = \frac{I}{e} - \frac{N(t)}{\tau_N} - G(t)P(t), \tag{4.4}$$

where M (R) refers to the emitter (receiver) lasers. The gain $G_{M,R} = g(N_{M,R} - N_o)/(1 + s\, P^2_{M,R})$. $P(t) = |E(t)|^2$ is the laser intensity. For simplicity, we have assumed identical internal laser parameters and operating conditions and neglected noise effects in the lasers. $\alpha = 5$ is the linewidth enhancement factor, $\tau_p = 2$ ps is the is the photon lifetime, $\tau_N = 2$ ns is the carrier lifetime, $g = 1.5 \cdot 10^{-8}$ ps^{-1} is the differential gain coefficient, $N_o = 1.5 \cdot 10^8$ is the carrier numbers at transparency, $s = 5 \cdot 10^{-7}$ is the gain compression coefficient, $I_{th} = 14.7$ mA is the threshold current, $\tau = 1$ ns is the feedback delay time and γ is the feedback strength. The last term in Eq. (4.3) only appears in the equation for the receiver

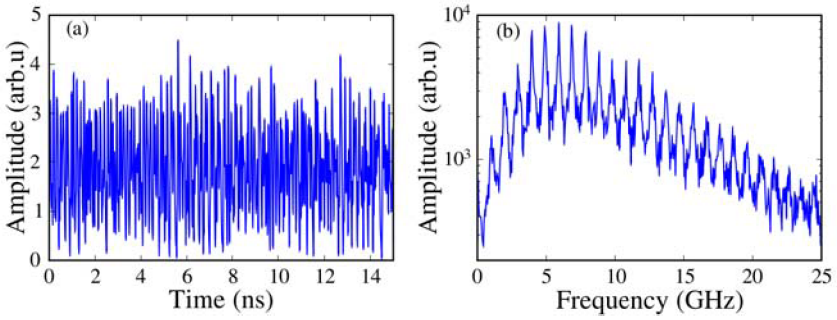

Figure 4.1: (a) Time trace and (b) power spectrum of the chaotic carrier generated by a semiconductor laser subject to feedback. Parameters: $I = 2I_{th}$.

laser and it accounts for the injection of the emitter laser field into the receiver. Without loss of generality, we consider that this injection occurs instantaneously.

An example of the generated chaotic carrier time trace and power spectrum is given in Fig. 4.1. To achieve a high degree of synchronization between emitter and receiver, the receiver is taken to be in a closed loop configuration [158, 162].

To illustrate the quality of the recovered messages, we will show eye diagrams of several sequences of recovered bits. In communication systems, an eye diagram is a representation in which consecutive bits of a digital data signal from a receiver are plotted on top of each other. The data transmission rate is used to set the corresponding time window. It is so called because, for several types of coding, the pattern looks like a series of eyes between a pair of rails. An open eye diagram corresponds to minimal signal distortion. To quantify the performance of the message recovery process we will use the so-called quality factor (Q), which is defined as:

$$Q = \frac{\mu_1 \quad \mu_0}{\sigma_1 + \sigma_0}, \tag{4.5}$$

where μ_1 and μ_0 are the average optical power of bits “1" and “0", and σ_1 and σ_0 are the corresponding standard deviations. A larger value of Q means a better recovery of the message. Note that this measure is similar to the Signal to Noise Ratio (SNR) that we defined in Chapter 2 to evaluate the performance of the noise filtering procedure.

Figure 4.2(a.2) presents the eye diagram of a sequence of recovered bits, which have been encoded with the method of Eq. (4.1) at a transmission bitrate of 1Gb/s and decoded with Eq. (4.2). An open eye diagram ($Q = 11.29$) is obtained since the emitter and receiver lasers are synchronized to a very high degree.

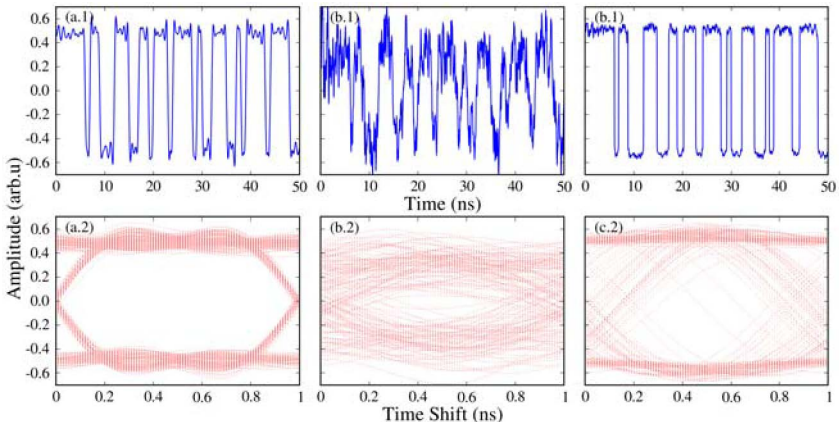

Figure 4.2: Recovered messages (top) and the corresponding eye diagrams (bottom) of an ensemble of 256 transmitted bits encoded with CM of $\epsilon = 0.04$. From left to right: (a) authorized receiver ($\kappa_r = 100\,\text{ns}^{-1}$), (b) GLE first pass ($a = 1000,\ r = 0.5$), and (c) GLE second pass ($a = 1,\ r = 0.65$).

One property of the encryption method described in Eq. (4.1) is that the mean value of the transmitted power is different if the bit transmitted is "1" or "0", during the length of one bit. This feature is shared by other encryption methods such as *Chaos Shift Keying* [163–166] and *Chaos Masking* [158, 167**?** –169], which makes this discussion relevant for these cases too. If the message modulation amplitude ϵ is large these differences on the mean value are easily detectable and the message can be recovered by using a linear filter, such as a low pass filter. On the contrary, if ϵ is small enough, usual filtering techniques are unable to recover the message. Therefore, this is a desirable regime of operation to achieve secure communications. However, the use of a nonlinear filter can improve the ability to detect these deviations, and therefore push the range of secure operation to smaller amplitudes. The disadvantage of working with such small amplitudes is that it increases the bit error rate of the communication and therefore decreases the transmission speed.

The transmission bitrate and the properties of the chaotic carrier itself also set a threshold on the message modulation amplitudes that can be regarded as being secure. Since the carrier is a chaotic signal, the respective mean value of consecutive segments tend to differ as the length of the segment becomes shorter. For the chaotic carrier shown in Fig. 4.1(a), the ratio of the standard deviation of the means of consecutive segments over the mean value of the signal is 0.0183 at 1Gb/s, 0.0547 at 2.5 Gb/s and 0.1045 at 5 Gb/s (here we will consider messages

transmitted at 1Gb/s). When the deviations from the mean value produced by the modulation of the message are of the same order of magnitude than those of the chaotic signal itself, a filtering technique will not be able to distinguish these intrinsic variations from the ones produced by the message, and therefore it will not be able to decrypt the message. The drawback of working in this regime is that, to recover the message with enough quality, a very good synchronization between the emitter and the receiver is needed.

As we said, the variations of the chaotic signal at 1Gb/s are about 2%, and we will show how with the GLE filtering technique we are able to decrypt signals up to these message modulation amplitudes, which is much better than what a linear filter can do.

4.2 Decoding method

The decoding procedure is a variation of the filtering method introduced in the previous section. As can be seen from the power spectrum in Fig. 4.1 the chaotic signal involves a large bandwidth and therefore this signal contains very fast variations along with slower ones at the frequency of the transmitted message. Therefore, the filtering process has to first filter the fast variations and then be adjusted to enhance the contrast of zones of the length of a bit. This is done by applying the filter in two steps: in the first step we choose a large value of a to filter the fast frequencies and in the second step we choose a much smaller value of a to enhance the contrast of the signal and recover the message. Since in the first step, the chosen value of a is very high, the second derivative term in Eq. (3.1) becomes dominant and therefore the equation becomes approximately the diffusion equation, therefore the first step acts as a linear filter and this is why we will refer to it in this way.

To illustrate the procedure we start by processing the message using an encoding amplitude of $\epsilon = 0.04$. In Figs. 4.2(b.1) and 4.2(b.2) we show a part of the time trace of the decoded message, and the eye diagram for the first pass with the filter, using $a = 1000$ and $r = 0.5$, respectively. Here we see that in this case we are able to see some features of the message but the eye diagram is very closed ($Q = 2.57$). This means that we would only be able to recover some parts of the message because of the errors, as previously said, this performance is similar to the expected for a linear filter.

In Fig.4.2(c.1) and 4.2(c.2) we show the effect of a second pass using $a = 1$ and setting h_0 to maximize the Q factor of the recovered message. Here it can be

seen that the message is almost fully recovered (except for an error in one bit, as can be seen in the eye diagram), and the eye diagram is very open ($Q = 5.09$). Considering these results it would not be secure to encode messages with this modulation amplitude.

In this case, the values of the parameters of the filter (Eq. 3.1) are not determined by looking at the stability of the recovered signal as we did in the previous chapter. Since now we are dealing with binary messages this give us a better way of choosing the parameters. First, the values of a are given by the requirements of the filtering procedure; for the first pass a has to be large enough to filter the fast frequencies of the chaos, and in the second pass it should give a diffraction length of the typical length of a bit. Since we are not trying to determine the exact length of every bit, but the sequence of bits, small variations of a in either of the steps will not change the final result significantly. Then, since the mean value of the message will be in general close to 0.5 we choose this value for r in the first step. Finally, the value of r for the second step is adjusted to maximize the Q factor. We also choose $b = 1$ since as was already stated in the previous chapter, changes of this value does not change significatively the results.

In Fig. 4.3 we show the Quality factor as a function of the message modulation amplitude ϵ. We can see that, applying the GLE twice, performs much better that with a single pass with large diffusion (which is basically a linear filter). While the performance is not as good as the authorized receiver, it is still enough to decode the message if the value of ϵ is not too small. Performance decreases with ϵ, and approaching $\epsilon \sim 0.02$ (which is of the order of the chaos fluctuations of the bit mean) the nonlinear filtering method recovers only part of the message. However, it should be kept in mind, that reproducing part of the message is already a security threat. So, to prevent decoding using a nonlinear filter like the one considered here, the amplitude of the message should be of the order or smaller than the chaos fluctuations of the bit mean.

4.3 New codification scheme

As we already stated, the GLE filter acts by detecting changes in the mean value of the signal within the diffraction length, therefore it is useless if the message is encoded in such a way that the mean value of the chaotic carrier is preserved. We introduce a modified version of the chaos modulation method, where transmitted bits "1" and "0" have identical mean:

$$P_t(t) = \Big(1 - \epsilon\, m(t)\Big)P_m(t) + \epsilon\, m(t)\bar{P}_m, \tag{4.6}$$

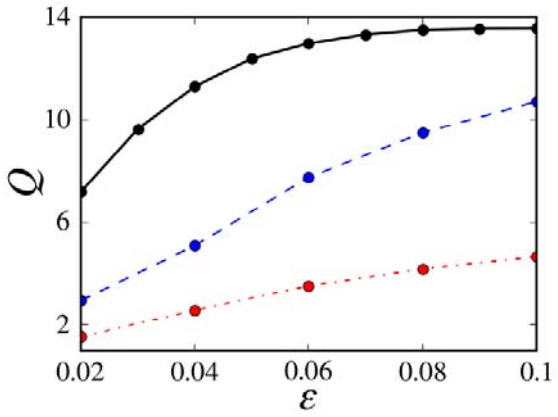

Figure 4.3: Quality factor Q as a function of the encrypted message modulation amplitude ϵ using the Chaos Modulation (CM) scheme. The solid line corresponds to the authorized receiver, the dotted dashed line to the GLE first pass, and dashed line to the GLE second pass.

where $\bar{P}_m$ is the mean of the chaotic carrier. The last term in Eq. (4.6) compensates for the changes in the mean value of the transmitted signal due to the message. The compensation term is chosen in such a way that $< P_t(t) >=< P_m(t) >=\bar{P}_m$ at any given time.

The recovery of the message at the authorized receiver side needs to account for the mean of the transmitted signal:

$$m'(t) = \frac{P_s(t) - P_t(t)}{\epsilon(P_s(t) - \bar{P}_m)} \tag{4.7}$$

There is a side-effect to the encryption method presented in Eq. (4.6). When $P_m(t) = \bar{P}_m$, no message is encrypted into the transmitted signal. A similar problem appears in the denominator of Eq. (4.7). No message can be recovered when $P_s(t) = \bar{P}_m$. These problems can be compensated for at the receiver side by neglecting the data points, in the recovery process, that are close to the mean of the emitter laser. Specifically, a data point will be neglected if $|P_s(t)/\bar{P}_m - 1| > K$, where K is an arbitrary number larger than 0.

In order to recover the message, the authorized receiver neglects the data points that are close to the mean of the incoming signal, which would result in a slightly worse recovery. However, the recovery of a message is possible and the eye diagrams for this method are presented in Figures 4.4(a.2) and 4.4(b.2) for $\epsilon = 0.04$ and $\epsilon = 0.1$, respectively. In these figures, we have taken $K = 0.1$,

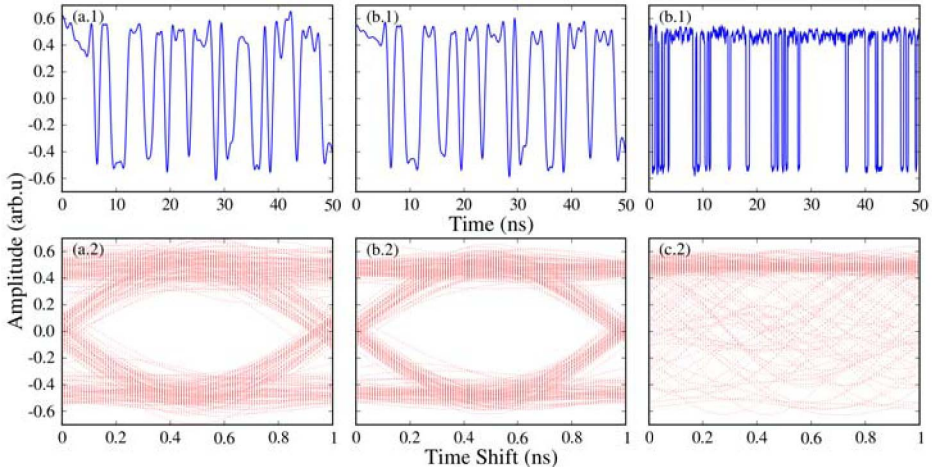

Figure 4.4: Recovered messages (top) and eye diagrams (bottom) of an ensemble of 256 transmitted bits encoded with MPCM. From left to right: (a) authorized receiver ($\kappa_r = 100$ ns ^{1} and $\epsilon = 0.04$), (b) authorized receiver ($\kappa_r = 100$ ns ^{1} and $\epsilon = 0.1$), and (c) GLE second pass ($d = 1$, $r = 0.5$ and $\epsilon = 0.1$).

meaning that a 16% of the points are neglected (values of K between 0.05 and 0.15 give similar results). The eye diagrams shown in Figs. 4.4(a.2) and 4.4(b.2) are still open ($Q = 5.66$ and $Q = 6.32$), even though they have degraded compared to the one shown in Fig. 4.2(a.2). The eye diagrams are obtained with the same synchronization degree between the emitter and receiver lasers. With the encryption method we suggest in Eq. (4.6), it is possible to keep the same mean for "1" and "0" transmitted bits at the expense of sacrificing part of the quality of the transmission. In Fig. 4.5 we show the Quality factor of the recovered message by an authorized receiver for different values of ϵ. We can see that while the quality of the recovered message is lower compared to Fig.4.3 the message is still perfectly recovered.

Now we apply the GLE method to a message encoded using this scheme. The result of the decoding operation (after the 2nd pass) is shown in Figure 4.4(c.2) for $\epsilon = 0.1$. As can be seen, nothing can be recovered from the encoded message but random bits ($Q = 1.80$). If we compare this result with the one obtained for $\epsilon = 0.04$ in 4.2(c.2) we see the effectiveness of this scheme against attacks with the GLE filter: using a message modulation amplitude five times bigger we obtain half the quality factor for the recovered message.

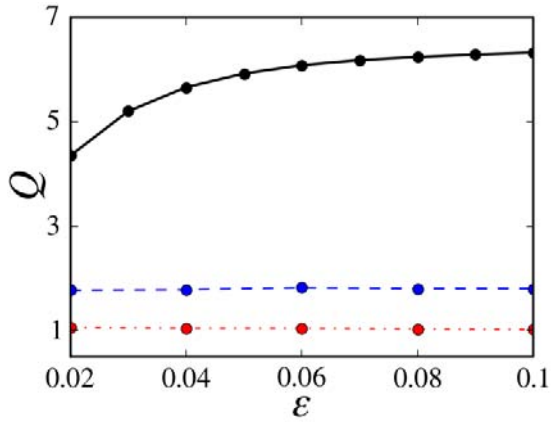

Figure 4.5: Quality factor Q as a function of the encrypted message modulation amplitude ϵ using the Mean-Preserving Chaos Modulation (MPCM) scheme. The solid line corresponds to the authorized receiver, the dotted dashed line to the GLE first pass, and dashed line to the GLE second pass.

Furthermore, in Fig.4.3(b) we can see that the quality factor for messages decoded with GLE (first and second passes) remains constant for all considered values of ϵ. This suggests that we are recovering now only random bits without correlation with the original message. Finally it is important to notice that, using this new encryption method, while the Quality factor increases with ϵ for the authorized receiver it remains almost constant for the GLE decoding, this means that even for large values of the modulation the GLE filter is unable to recover the message.

4.4 Conclusions

In this chapter we applied the filtering method developed in Chapter 3. Since this method is able to detect changes on the mean value of a data series, by properly tuning the parameters of the Ginzburg Landau Equation we where able to decode messages encrypted by Chaos Modulation. Because of the way on which this method works, it is possible to apply it to other encryption methods that do not preserve the mean value of the chaotic signal.

The characteristics of the filtered signal provide, in this case, a better way of testing the obtained results than in the previous chapter. We can measure the Q

factor of the recovered message and tune the parameters in order to minimize it. This gives the best possible recovered message with this method.

We have also shown how this nonlinear filtering method outperforms the linear filter. This is due to the fact that besides filtering the fast frequencies of the chaotic signal as the linear filter does, the nonlinear one enhances the contrast of the bits "1" and "0", improving the Quality factor of the recovered message.

Finally, we have shown how this method is rendered useless if the message is encoded by means an encryption scheme that preserves the mean value of the signal. Despite that is not the aim of this text make a thorough study of the subject of security in chaos encoded communications, we present this chapter as an example of how commonly used encryption schemes can be broken, and how the security of the transmission can be recovered by using the Mean-Preserving Chaos Modulation encoding scheme.

Part II

Dynamics of Localized Structures in Kerr Cavities

Chapter 5

Localized Structures in Kerr Cavities with Homogeneous Pump

In Chapter 2 we have studied the image and data processing possibilities in a cavity filled with a second order nonlinear material. As we previously stated the χ^2 coefficient is nonzero only in noncentrosymmetric materials, i.e. that do not display inversion symmetry. Since liquids, gases, and many kind of solids are symmetric under inversion, χ^2 vanishes identically allowing for third order effects (given by a χ^3 coefficient) to become evident [130]. In this part we will study the model derived in Chapter 1 for a cavity filled with a third order medium, pumped with an homogeneous beam. Studies of this model [98, 98] showed that this equation exhibits Localized Structures (LS) that arise as a consequence of a modulational (namely a pattern-forming) instability of a homogeneous solution. In particular, they exist in the parameter range where the homogeneous solution coexists with stable subcritical (hexagonal) patterns. Here we consider the dynamics this structures (also known as Kerr cavity solitons). This LS share some properties with propagating spatial (conservative) solitons in a Kerr medium, but there are interesting differences. For conservative solitons there is a family of solutions and the solution amplitude depends on the initial energy. On the contrary, in a dissipative system, LS are unique once the parameters of the system has been fixed. Conservative Kerr spatial solitons are stable in one transverse dimension (1D), but, it is well known that their 2D counterparts are unstable against self-focusing collapse [170]. The stability and dynamics of 2D Kerr cavity solitons are thus of particular interest, and their existence and stability has been studied in several papers [78, 99, 171].

In what follows of this chapter we will first study the overall dynamical behavior exhibited by the system in parameter space in Section 5.1. Next, Section 5.2 presents the case for the instability exhibited by LS through a saddle-loop bifurcation, discussing the main evidences to support this conclusion. Section 5.3 goes a step further in this direction, presenting a more detailed study of how the dynamics of the system can be understood through a simplified analysis, by performing an analysis in terms of modes. Then, in Section 5.4 we study the excitable regime that arises in the saddle-loop bifurcation. Finally, in Section 5.6 we show how this saddle-loop bifurcation appears in the system arising from a Takens-Bogdanov point.

5.1 Overview of the behavior of the system

If we consider an homogeneous pumping field $E_i = E_0$, Eq. (1.87) becomes,

$$\frac{\partial E}{\partial t} = -(1 + \imath\theta)E + \imath\nabla^2 E + E_0 + \imath|E^2|E \tag{5.1}$$

this equation has a homogeneous steady state solution $E_s = E_0/(1 + (i(\theta - I_s))$, where $I_s = |E_s|^2$ [137]. Fig. 5.1 shows the dependence of I_s on the pump intensity $I_0 = |E_0|^2$. The homogeneous solution is bistable for values of the detuning $\theta > \sqrt{3}$. In the following we use I_s, together with θ, as our control parameters. Notice that a value of I_s always corresponds to a single value of I_0, while the opposite is not true. Therefore, is more suitable to use the value of I_s to characterize the homogeneous stationary solution.

Notice that in the absence of losses and an input field, the field can be rescaled to $E \to Ee^{i\theta t}$ to remove the detuning term and Eq. (5.1) becomes the Nonlinear Schrödinger Equation (NLSE). It is well documented that in the NLSE in two spatial dimensions an initial condition with enough energy collapses, namely energy accumulates at a point of space leading to the divergence of the solution at a finite time [172]. Cavity losses prevent this collapse, although in the parameter region in which localized structures are stable their dynamics are closely related to the collapse regime.

A linear stability analysis of the homogeneous solution, with respect to a spatially periodic perturbation, leads to the dispersion relation

$$\lambda(\vec{k}) = -1 \pm \sqrt{-(\theta + k^2 - 3I_s)(\theta + k^2 - I_s)} \tag{5.2}$$

where $\lambda(\vec{k})$ is the linear growth rate of the perturbation with wavevector $\vec{k}$ and $k = |\vec{k}|$. In this work we consider only detunings smaller than 2. * For $\theta < 2$ a pattern forming instability (modulational instability) takes place at $I_s = 1$ with a critical wave number $k_c = \sqrt{2-\theta}$. For $I_s > 1$ the homogeneous solution continues to exist, although it is unstable and the maximum linear growth rate is for wavevectors with modulus $k_u = \sqrt{2I_s - \theta}$. This selected wavenumber is such that the diffraction phase modulation k_u^2 balances the nonlinear phase modulation $2I_s$ and the cavity detuning θ. The modulational instability leads to the formation of hexagonal patterns [86, 137] (see Fig. 1.8). These hexagonal patterns are subcritical, namely through a S-shape branch and, thus, they coexist with the stable homogeneous solution for a certain parameter range.

In fact, the patterns arising at the modulational instability are typically oscillatory and increasing the pump they undergo further instabilities which eventually lead to optical turbulence [173, 174]. Static hexagonal patterns can be found sub-

*For $\theta > 2$ the lower branch homogeneous solution is stable (see Fig. 5.1 d)), but the upper branch is always unstable with respect to finite transverse wave numbers perturbations.

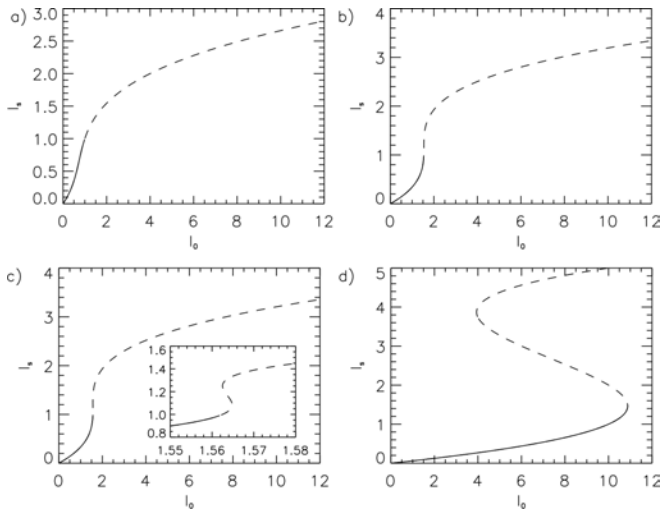

Figure 5.1: Intensity of the homogeneous solution I_s as a function of the input intensity I_0 for Eq. (5.1). a) $\theta = 1.0$, b)$\theta = \sqrt{3}$, c)$\theta = 1.75$ (the inset shows a close up of the bistable region), d) $\theta = 4.0$. Solid (dashed) lines indicate stable (unstable) solutions.

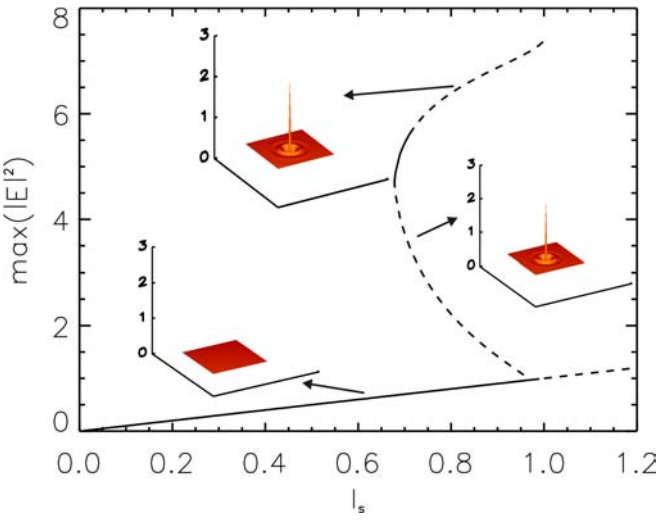

Figure 5.2: Bifurcation diagram of stationary localized structures in the Kerr cavity: $\max(|E|^2)$ vs I_s for $\theta = 1.34$. Solid lines represent stable solutions and dashed lines unstable ones. The lowest branch corresponds to the homogeneous solution that becomes unstable at $I_s = 1.0$. The upper and middle branches correspond to the stable and unstable LS, respectively, and are originated at a saddle-node bifurcation. The upper branch becomes Hopf unstable for larger values of I_s. The 3D plots show from top to bottom the profile of the upper branch LS, the middle branch LS and the homogenous solution.

critically, that is, decreasing the pump value below the modulational instability point.

The bistability of the pattern and the homogeneous solution is at the origin of the existence of stable LS that appear when suitable (localized) transient perturbations are applied. The LS can be seen as a solution which connects a cell of the pattern with the homogeneous solution. The LS are rotationally symmetric around their center (see Fig. 1.8). While the existence of LS in this bistable regime is quite generic in extended systems, its stability strongly depends on the particular system. The mechanism by which LS appear is a saddle-node bifurcation, as can be seen in Fig. 5.2 for $\theta = 1.34$ and $I_s \sim 0.655$ ($|E_0|^2 \sim 4.5$) in which a pair of stable-unstable LS are created [92, 175]. As shown in the Appendix B, using a numerical method with arbitrary precision it is possible to determine the stability of the LS solutions. The LS with larger amplitude (upper-

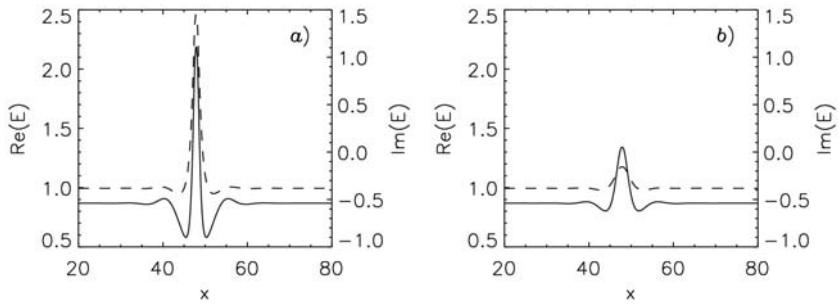

Figure 5.3: Transverse cut of two LS, one from the upper (stable) branch a) and one from the middle (unstable) branch b) in Fig. 5.2 ($I_s = 0.9$). The solid (dashed) line corresponds to Re[E] (Im[E]).

branch LS) is stable at least for some parameter range, while the one with smaller amplitude (middle-branch LS) is always unstable. Fig. 5.3 shows a transverse cut of typical middle and upper branch LS. The spectrum of eigenvalues (of matrix **U**, Eq. (B.7)) for a middle branch LS is shown in Fig. 5.4. There is only one positive eigenvalue so this structure has a single unstable direction in the full phase space, is a saddle. Once it is created, the middle branch LS does not undergo any bifurcation for the parameter values explored in this chapter and, so, remains a saddle point in phase space. The middle branch LS acts as a barrier: if a initial condition is somehow above the middle branch in phase space, it will evolve to the upper branch (so that the LS is created), while it it is below it will decay to the homogeneous solution. This role of the middle branch LS as a separatrix in phase space is quite general, and has been identified in a semiconductor model [176] and experimentally observed for LS in a sodium cell with feedback [177–179] and in a semiconductor cavity [180].

Early studies already identified that the upper branch LS may undergo a Hopf bifurcation leading to a oscillatory behavior [98]. Thus, in these conditions a LS is an autonomous oscillon. An interesting connection to the conservative case is that the growth of the LS during the oscillations resembles the collapse regime observed for the $2D$ (or $2+1$) NLSE. In this case, however, after some value is attained for the electric field, E, dissipation arrests this growth.

The oscillatory instabilities [181], as well as azimuthal instabilities, were fully characterized later [99]. In Fig. 5.5 we show the region in parameter space where LS are static or oscillate. As one moves in parameter space away from the Hopf bifurcation, the LS oscillation amplitude grows, and finally the limit

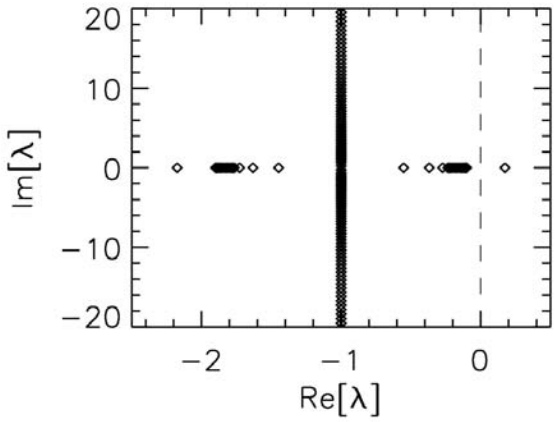

Figure 5.4: Spectrum of the unstable (middle branch) LS for $\theta = 1.30478592$ and $I_s = 0.9$.

cycle touches the middle-branch LS in a saddle-loop bifurcation which leads to a regime of excitable dissipative structures [182, 183].

In the rest of the chapter we will analyze in detail the main features of the dynamical behavior exhibited by the LS. The saddle-loop bifurcation is discussed in Section 5.2 and the excitability regime in Section 5.4. In Section 5.6 we discuss the presence of a Takens-Bogdanov codimension-2 point which organizes the phase space.

5.2 Saddle-loop bifurcation

A saddle-loop bifurcation (described in Chapter 1) is a global bifurcation in which a limit cycle becomes biasymptotic to a (real) saddle point, or, in other terms, becomes the homoclinic orbit of a saddle point, i.e., at criticality a trajectory leaving the saddle point through the unstable manifold returns to it through the stable manifold. Thus, at one side of this bifurcation one finds a detached limit cycle (stable or unstable), while at the other side the cycle does not exist any more, only its *ghost*, as the bifurcation creates an exit slit that makes the system dynamics

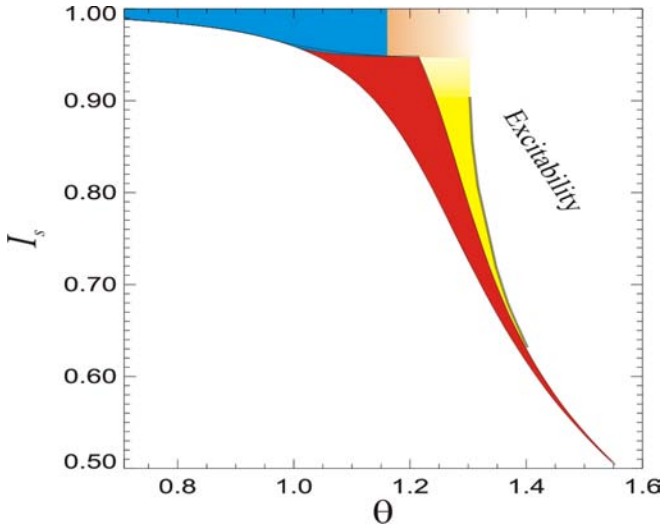

Figure 5.5: Phase diagram of localized structures in the Kerr cavity. LS are stable in the red region and oscillate in the yelow one (the line between these two regions indicates a Hopf bifurcation). In the lower part, below the saddle-node bifurcation (solid line), there are no LS, while in the upper part, above the saddle-loop bifurcation (dashed line), the system exhibits excitability. When crossing from the red region to the blue (brown) one LS develops azimuthal instabilities with azimuthal number m=6 (m=5) which lead to an extended pattern.

to leave the region in phase space previously occupied by the cycle. Therefore, after the bifurcation the system dynamics jumps to another available attractor. In the present case this alternative attractor is the homogeneous solution.

Let us take θ as the control parameter and assume that the saddle-loop bifurcation occurs for $\theta = \theta_{SL}$, and, for convenience, and without lack of generality, let us assume that $\theta < \theta_{SL}$ corresponds to the oscillatory side, where the limit cycle is detached of the saddle point, while, in turn, $\theta > \theta_{SL}$ corresponds to the side where one only has a fixed point solution. The fact that the bifurcation is global, implies that it cannot be detected locally (a local eigenvalue passing through zero), but one can still resort to the Poincaré map technique * to analyze it, and, interestingly, the main features of the bifurcation can be understood from the knowledge of the linear eigenvalues of the saddle.

The case studied here is the simplest, and it is analog to the normal form shown in Chapter 1: a saddle point with real eigenvalues, say $\lambda_s < 0$ and $\lambda_u > 0$, in a 2-dimensional phase space. Strictly speaking, in our case the saddle has an infinite number of eigenvalues (Fig. 5.4), but only two eigenmodes take part in the dynamics close to the saddle. This will be studied in more detail in Sec. 5.3. It is convenient to define the so called *saddle index* $\nu = -\lambda_s/\lambda_u$ and *saddle quantity* $\sigma = \lambda_s + \lambda_u$. It can be shown † that for $\sigma < 0$, or $\nu > 1$, at the side of the saddle-loop bifurcation where one has a detached cycle, this cycle is stable, while for $\sigma > 0$ ($\nu < 1$), the cycle is unstable. Analogously, one can study the period of the cycle close to this bifurcation, and to leading order it is given by [184],

$$T \propto -\frac{1}{\lambda_u} \ln|\theta - \theta_{SL}| \,. \tag{5.3}$$

This expression is accurate for θ close enough to θ_{SL}. Interestingly, the transient times spent by a trajectory in the ghost region after the cycle has ceased to exist, close enough to the bifurcation point, also show this scaling.

From a numerical point of view, we will characterize the occurrence of a saddle-loop bifurcation in the system by studying the scaling of the period of the oscil-

* The Poincaré map can be constructed through two cross sections, i.e., two planes that are transversal to the limit cycle, and that are placed slightly before and after the closest approach of the cycle to the saddle point. From these two planes one can construct two maps: the so-called local (or linear or singular) map, T_0, that takes the flow from the plane before the saddle point to the plane after the saddle point, and it is dominated by the saddle point, and the global (or nonlinear) map, T_1, that takes the flow all the way from the plane past the saddle point through all the limit cycle back to the plane before the saddle point. The complete Poincaré map is the composition of these two maps. It has to be remarked that the T_0 map is unbounded, as the return time is infinity at the onset of the global bifurcation.

† For the details refer, e.g., to Sec. 12.3 of Ref. [102]

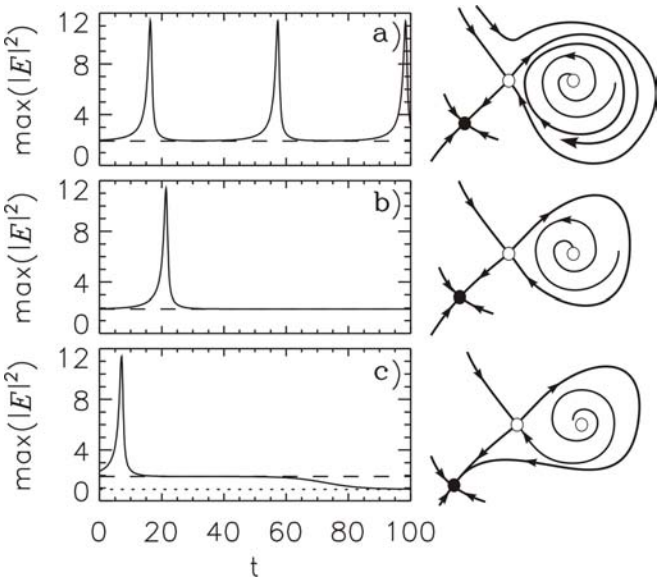

Figure 5.6: Left: LS maximum intensity as a function of time for increasing values of the detuning parameter θ. From top to bottom θ=1.3047, 1.30478592, 1.304788. Is = 0.9. Right: Sketch of the phase space for each parameter value, similar to the Fig. 1.24 for the normal form of the saddle-loop bifurcation.

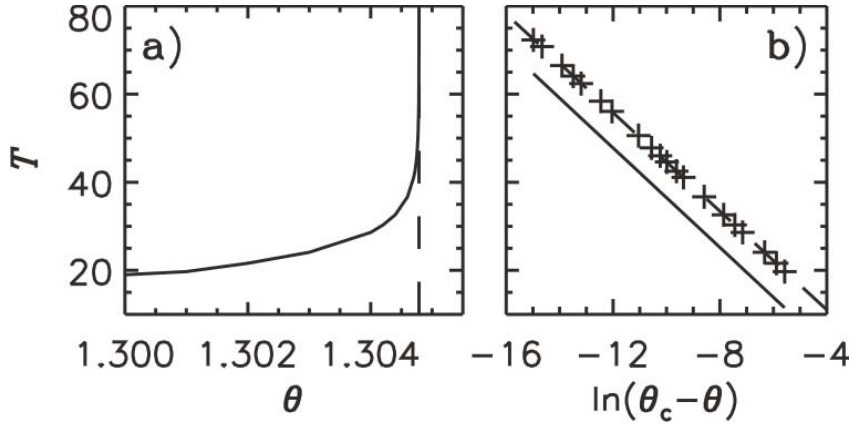

Figure 5.7: (a) Period of the limit cycle T as a function of the detuning θ for $Is = 0.9$. The vertical dashed line indicates the threshold of the saddle-loop bifurcation $\theta_{SL} = 1.30478592$. (b) Period T as a function of $ln(\theta_{SL} - \theta)$. Crosses correspond to numerical simulations while the solid line, arbitrarily positioned, has a slope $1/\lambda_u$ with $\lambda_u = 0.177$ obtained from the stability analysis of the unstable LS.

lations. The bifurcation point will be characterized by the fact that approaching from the oscillatory side the period diverges to infinity, and also because past this bifurcation point the LS disappears and the system relaxes to the homogeneous solution as shown in Fig. 5.6 for $I_s = 0.9$. For this value of I_s the saddle-loop takes place at $\theta_{SL} = 1.30478592$. In the figure the time evolution of the maximum of the LS is plotted for three different values of the detuning differing slightly, one just above, one at the saddle-loop bifurcation and the other just below θ_{SL}. Figure 5.7 contains a logarithmic-linear plot of the period versus a control parameter, that exhibits, as expected, a linear slope. Furthermore, one can confront the value of the slope obtained form the simulations with its theoretical prediction, Eq. (5.3), namely $1/\lambda_u$. The full spectrum of the middle branch soliton for $\theta = \theta_{SL}$ (calculated as described in the Appendix B) is shown in Fig. 5.4. The agreement between the simulations and theoretical slopes is within 1%.

A comment is in place here regarding the spectrum shown in Fig. 5.4. The spectrum is formed by a stable continuous (although numerically discretized) and a discrete spectrum with a positive ($\lambda_u = 0.177$) and a negative ($\lambda_s = -2.177$) eigenvalue. Having this spectrum in mind is perhaps surprising that one can describe the bifurcation route very well qualitatively, and to some extent quantitatively (eg. the observed scaling law, Fig. 5.7), resorting to a planar dynamical

system when many modes could be, in principle, involved. The first mode of the planar theory univocally corresponds to the positive (unstable) eigenvalue, $\lambda_u = 0.177$, while, in first approximation, the second mode should correspond to the second, closest to zero, eigenvalue. This eigenvalue belongs however to a continuum band and the arbitrarily close eigenvalues of its band could play a role in the dynamics, modifying the planar theory. Moreover, considering this mode $\lambda \sim -0.10$ the saddle-index $\nu = -\lambda/\lambda_u < 1$ indicating that the cycle emerging from the saddle-loop should be unstable, although we observe otherwise. The analysis of the modes of the unstable LS and dimensionality of the phase space is addressed in detail in the next section.

5.3 Mode Analysis

In this section we analyze the dynamics in terms of the modes obtained by performing the stability analysis of the middle branch LS in a parameter region close to the saddle-loop bifurcation, as described in Appendix B. By plotting the spatial profile of the modes one obtains a clue to identify the relevant modes for the dynamics. It turns out that most of the modes of the stable spectrum are delocalized. Figure 5.8 contains a representation of two such delocalized modes. The bands of extended modes correspond to modes of the homogeneous background, and are, except for a radial dependence coming from the fact that we are using radial instead of Cartesian coordinates, basically Fourier modes. The main difference between these modes is the wavenumber of their oscillations (see Fig. 5.8). There are however two exceptions: two localized modes which are the one corresponding to the unstable direction and the most stable mode, namely that with eigenvalue $\lambda_s = -2.177$. The spatial profile of these two modes is shown in Figure 5.9. Since the dynamics of the LS remains localized in the space, this is an indication that only these two localized modes take part in the dynamics. To check this hypothesis we have projected the two trajectories shown in Fig. 5.6 for parameters close to the saddle-loop bifurcation onto all the eigenmodes of the unstable LS and observed that only the two localized modes have a significant amplitude.

From the knowledge of the spectrum and the relevant eigenmodes, we can now explain the stability of the orbits emerging out of the bifurcation, namely through the saddle index introduced above. Computing this index for the two modes that participate in the saddle-loop bifurcation one obtains $\nu = 2.177/0.177 > 1$, what fits perfectly with the fact that the cycle that detaches at one side of the bifurcation point is stable. Thus, one may understand that all the dynamical

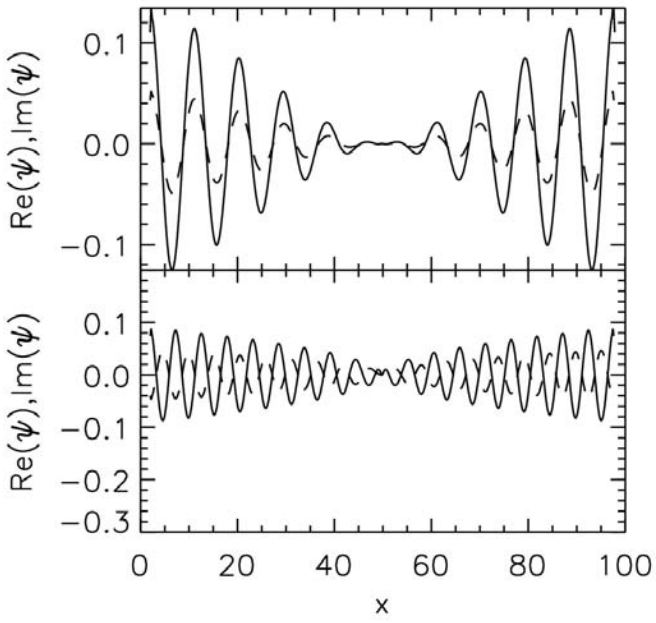

Figure 5.8: Stable extended modes from the continuous band. The top (bottom) panel shows the transverse cut of the mode associated to the eigenvalue $\lambda = -0.1$ ($\lambda = -1 + i0.24$) of Figure 5.4.The solid (dashed) line indicates the real (imaginary) parts of the eigenmode.

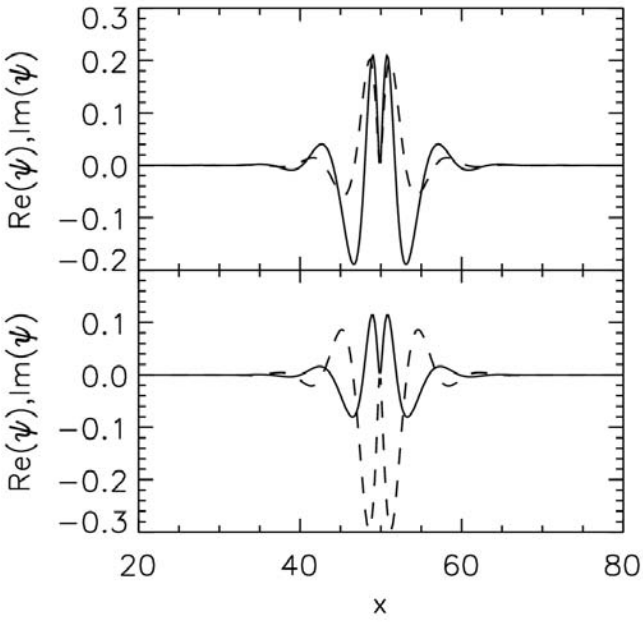

Figure 5.9: Transverse cut of the unstable (top) and the most stable (bottom) modes of the unstable LS. These modes are associated to the eigenvalues $\lambda_u = 0.177$ and $\lambda_s = -2.177$ of Fig. 5.4 respectively. The solid (dashed) line indicates the real (imaginary) parts of the eigenmode.

instability scenario of the LS can be analyzed qualitatively in a planar dynamical system.

A better understanding of the dynamical route, and a justification of the role of the two participating localized modes, stable and unstable, can be obtained through a closer scrutiny of the *linear* region, namely the region close to the saddle point (or alternatively, the region defined by the singular map, or close to it). Figure 5.6(a) contains a time trace of one such trajectory in the region in which the limit cycle is stable, but close to the saddle-loop bifurcation. Following Appendix B we project the deviation of the trajectory from the unstable LS (saddle point) onto the most stable and the unstable eigenvectors of the adjoint Jacobian matrix of the unstable LS. These projections are the amplitudes of the unstable (β_1) and the most stable (β_2) modes of the unstable LS (modes whose profile is shown in Fig. 8). The trajectory enters the linear region through the stable mode and leaves the region through the unstable one. This behavior is clear in the insets of Figure 5.10. Next, we reconstruct the qualitative sketch of the bifurcation shown in Fig. 5.6 from the knowledge of the projections onto the modes, i.e. we represent the trajectories before and after the saddle-loop bifurcation in mode space. Thus, Figure 5.10 contains a quantitative, reconstructed, 2-dimensional phase space from the two localized modes involved in the transition for a set of parameter values in the a) oscillatory and b) excitable side of the transition. Close to the saddle, the linear dynamics takes place on a plane, but away from this point the nonlinear dynamics bends the trajectory out of the plane into the higher dimensional space, hence, the apparent crossing of the trajectory in Fig. 5.10.

This is the final numerical confirmation that the infinite-dimensional dynamical system on which LS live can be reduced to an excellent degree of precision to a 2-dimensional dynamical system, and that the picture is fully consistent with a saddle-loop bifurcation.

5.4 Excitable behavior

As in our case the saddle-loop bifurcation involves a fixed point (the homogeneous solution), on one side of the bifurcation, and an oscillation, on the other, the system is a candidate to exhibit excitability [110]. It must be stressed that excitable behavior is not guaranteed *per se* after a saddle-loop bifurcation, and, in particular one needs a fixed point attractor that is close enough to the saddle point that destroys the oscillation. The excitability threshold in this type of sys-

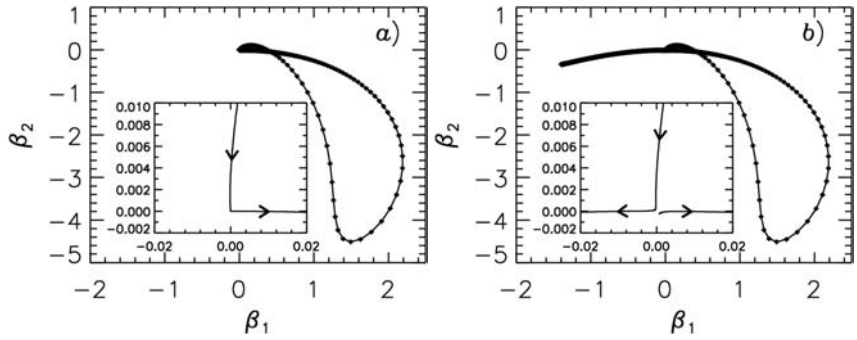

Figure 5.10: Reconstructed phase space by finding the amplitude of the deviation of the trajectory from the unstable LS in the unstable (β_1) and the most stable (β_2) modes of the unstable LS. Panel a) corresponds to an oscillatory trajectory while panel b) to an excitable one. The symbols are equispaced in time along the trajectory, so sparse symbols indicate fast dynamics while dense symbols indicate slow dynamics. The saddle point is at $(0, 0)$. The inset is a close up of the linear region around the saddle.

tem is the stable manifold of the saddle point, what implies that the observed behavior is formally Class I Excitability [110], i.e., the excitability is characterized by response times that can be infinite (if a perturbation hits exactly the stable manifold of the fixed point), or, conversely, frequencies starting from zero. In our system, the excitable threshold reduces by increasing I_s (Fig. 5.2), since the middle branch LS (the saddle point) gets progressively closer to the homogeneous solution (fixed point).

This excitability scenario was first shown in Ref. [182], and in parameter space it is found in the region above the dashed line corresponding to the saddle-loop bifurcation shown in Fig. 5.5. Fig. 5.11 shows the resulting trajectories after applying a localized perturbation in the direction of the unstable LS with three different amplitudes: one below the excitability threshold (a), and two above: one very close to threshold (b) and the other well above (c). For the below-threshold perturbation the system decays exponentially to the homogeneous solution, while for the above-threshold perturbations a long excursion in phase space is performed before returning to the stable fixed point. The refractory period for the perturbation just above the excitability threshold is appreciably longer due to the effect of the saddle. The spatio-temporal dynamics of the excitable localized structure is shown in Fig. 5.12. After an initial localized excitation is applied, the peak grows to a large value until the losses stop it.

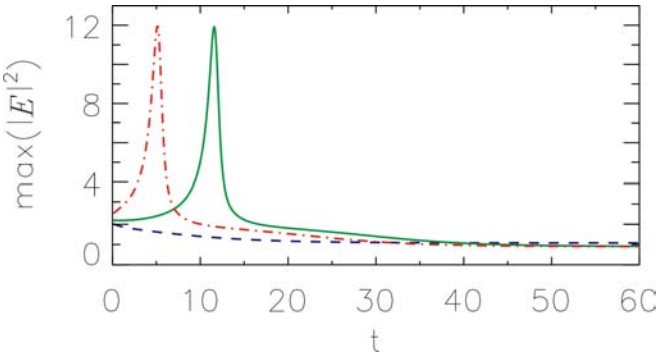

Figure 5.11: Time evolution of the maximum intensity starting from the homogeneous solution (I_s = 0.9) plus a localized perturbation of the form of the unstable LS multiplied by a factor 0.8 (blue dashed line), 1.01 (green solid line) and 1.2 (red dotted line).

Then it decays exponentially until it disappears. A remnant wave is emitted out of the center dissipating the remaining energy.

At this point it is worth noting that neglecting the spatial dependence Eq. (5.1) does not present any kind of excitability. The excitable behavior is an emergent property of the spatial dependence and it is strictly related to the dynamics of the 2D LS. Without spatial dependence, excitability as a result of a saddle-loop bifurcation has been observed in different systems [109, 110, 128].

Finally, it is interesting to remark that the excitable region in parameter space is quite large (Fig. 5.5) and, therefore, potentially easy to observe experimentally. While this excitable behavior belongs to Class I (the period diverges to infinity when a perturbation hits the saddle), due to the logarithmic scaling law for the period (Eq. 5.3), the parameter range over which the period increases dramatically is extremely narrow (Fig. 5.7(a)). Therefore, from an operational point of view, systems exhibiting this scenario might not be classified as Class I excitable, as the large period responses may be easily missed [108].

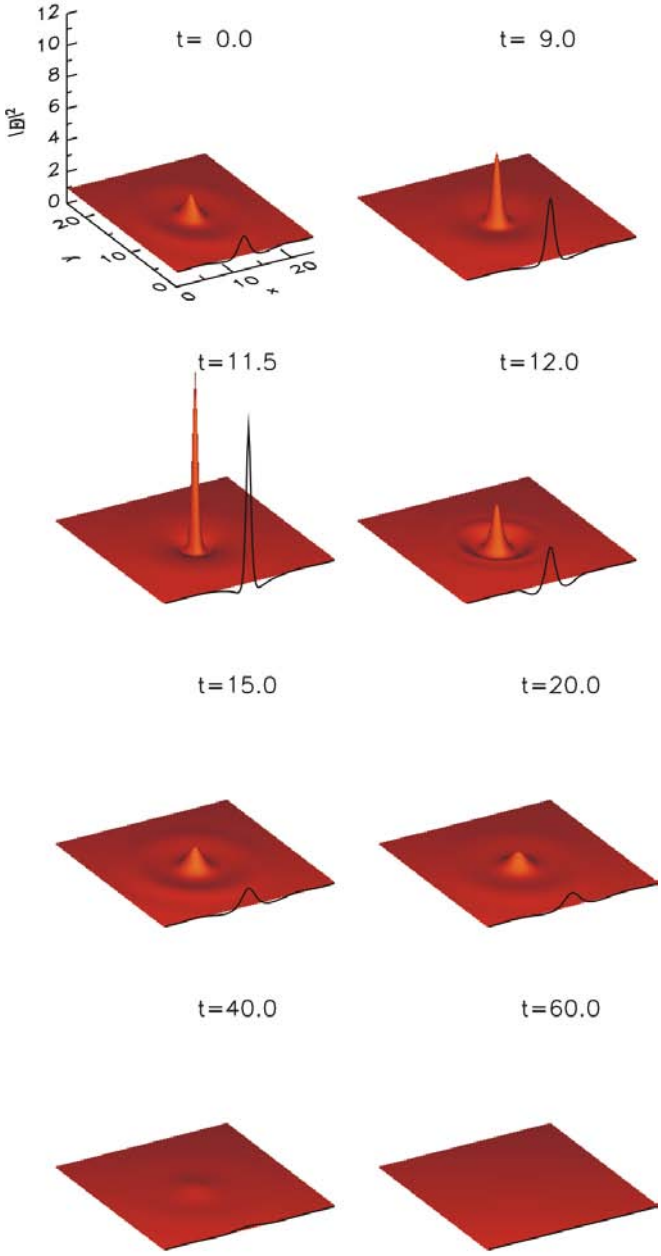

Figure 5.12: *3D* plots showing the transverse intensity profile at different times for the trajectory shown in Fig. 5.11(b). The solid lines show a cut of the structure through the center.

5.5 Coherence Resonance

Coherence resonance [185] (also called *stochastic resonance without periodic forcing* [186, 187]) is a phenomenon characterized by the appearance of oscillations in the presence of added (e.g. white) noise in a system that in the absence of noise exhibits excitable behavior. The distinctive feature of this phenomenon compared to stochastic resonance is that it is not necessary to introduce externally a time scale: the added noise *activates* the characteristic scale (of oscillation) *hidden* of the system (due to its excitable character). Coherence resonance in excitable systems, and also in a more generic sense in systems in which noise can excite a more or less hidden time scale, has been shown for a large class of systems [188].

Typically, coherence resonance is quantified in terms of the parameter R defined as [185]:

$$R = \frac{\sqrt{Var(t)}}{< t >} \tag{5.4}$$

where t is the time between excitable excursions.

One important difference between the systems considered in these references and our excitable LS is the fact that our system is spatial, i.e., infinite-dimensional, what implies that the application of external noise has the effect of exciting a large number of degrees of freedom in the system.

We have added a complex Gaussian white noise ξ of zero mean and variance

$$\left\langle \xi(\vec{x},t)\xi(\vec{x'},t')\right\rangle = \chi\delta(\vec{x}-\vec{x'})\delta(t-t') \tag{5.5}$$

to the right hand side of Eq. (1.87). Fig. 5.13 shows the value of the coherence resonance indicator R as a function of the noise amplitude. Insets show typical time traces of the maxima of the localized structure, for different values of the noise amplitude. For very weak noise, excitable structures are weakly excited and the intervals between excitable excursions are very irregular. Since the variance is large R takes a large value. For very large χ the trajectory is extremely noisy, and again R takes large value. The value of R goes through a minimum for intermediate values of the noise, indicating that localized structures indeed show coherence resonance in the presence of uncorrelated spatial noise.

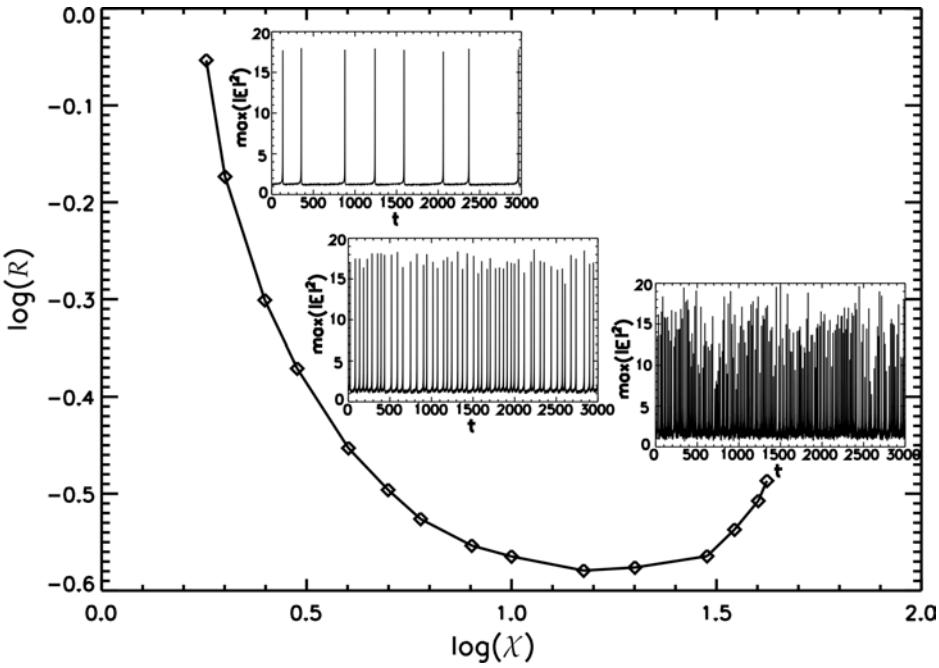

Figure 5.13: Logarithm of the coherence resonance indicator R as a function of logarithm of the noise amplitude. From left to right, the insets show typical time traces of the maxima of the LS for $\chi = 4$, 15 and 40 respectively.

5.6

Takens-Bogdanov Point

The saddle-loop (or homoclinic) bifurcation is, in some sense, not *generic*. Namely, that a tangency between a limit cycle and a saddle point occurs exactly such that it happens simultaneously at both the sides of the stable and unstable manifolds is, in principle, not to be expected generically. In fact, also due to the fact that global bifurcations are not always easy to detect, showing that a dynamical system exhibits a certain type of codimension-2 point is the most convincing argument for the existence of such bifurcations.

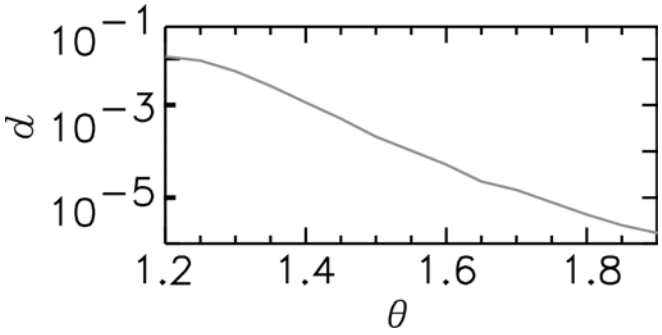

Figure 5.14: Distance between the saddle node and Hopf lines of Fig. 5.5 as a function of θ.

An scenario in which the unfolding of a codimension-2 point yields a saddle-loop (or homoclinic) bifurcation is a Takens-Bogdanov (TB) point [103, 105]. Namely, a double-zero bifurcation point in which a saddle-node bifurcation line and the zero-frequency limit of a Hopf bifurcation line (thus, no longer a Hopf line in the crossing point) meet in a two-parameter plane. The particular feature that, at the TB point, the Hopf line has zero frequency allows this codimension-2 bifurcation to occur in a two-dimensional phase space. This bifurcation has to be distinguished from the occurrence of a crossing between a saddle-node and a Hopf lines at non-zero frequency, known as Gavrilov-Guckenheimer (saddle node-Hopf point), that requires a three-dimensional phase space to take place. As was described in Chapter 1 (Fig. 1.25), from the unfolding of a TB point a saddle-loop line, apart from the saddle-node and Hopf lines, emerges [103, 105] from the TB point.

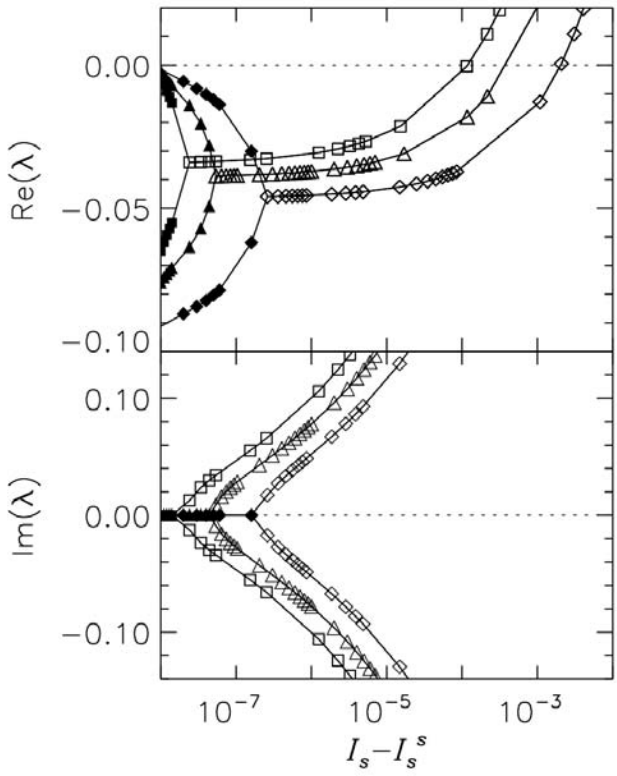

Figure 5.15: Real part (upper panel) and imaginary part (lower panel) of the eigenvalues of the upper branch LS for three vertical cuts in Fig. 5.5 corresponding to three different values θ: squares, 1.7; triangles, 1.5; rhombs, 1.4 versus the difference between I_s and its value at the saddle-node bifurcation, $I_s^s(\theta)$.

This can be also checked in Fig. 5.5, in which a two-parameter bifurcation plot is presented as a function of the two parameters of the system: I_s and θ. The problem here is that the saddle-node and Hopf lines tend to meet only asymptotically, namely when $\theta \to \infty$. In Fig. 5.14 [182] it can be seen how distance between the saddle-node and the Hopf lines decreases as one increases θ (the same happens with the saddle-loop line). By calculating the eigenvalues, it can be seen that, indeed the frequency (viz. their imaginary part) goes to zero as one approaches the TB point. Fig. 5.15 displays the two eigenvalues with largest real part of

the upper branch LS for parameter values corresponding to three vertical cuts of Fig. 5.5. Open symbols correspond to eigenvalues with a non-zero imaginary part while filled symbols are associated to real eigenvalues. Where the open symbols cross zero in the upper panel of Fig. 5.15 signals the Hopf bifurcation while where the filled symbols cross zero signals the saddle-node bifurcation. The origin for the three plots is taken at the saddle-node bifurcation. At some point along the branch of the two complex conjugate eigenvalues associated to the Hopf bifurcation the imaginary part vanishes leading to two branches of real eigenvalues, the largest of which is precisely the responsible of the saddle-node bifurcation. As detuning increases the Hopf and saddle-node bifurcation points gets closer and closer but the structure of eigenvalues remains unchanged so that when the Hopf and saddle-node bifurcation will finally meet the Hopf bifurcation will have zero frequency, signaling a TB point.

The TB point takes place asymptotically in the limit of large detuning θ and small pump E_0. In this limit Eq. (5.1) becomes the conservative NLSE [78]. The Hopf instability in this limit was studied in [181], where evidence of the double-zero bifurcation point was given, however the unfolding leading to the scenario presented here was not analyzed.

5.7 Conclusions

In this chapter a detailed study of the instabilities of LS solutions in homogeneously pumped nonlinear Kerr cavities and the associated excitability route first reported in Ref. [182] was carried out. Excitability arises as an emergent property of the LS, since the local dynamics of the system is not excitable. The instability that leads to the destruction of oscillatory LS found in this system can be characterized by a saddle-loop (homoclinic) bifurcation, in which (in phase space), the oscillation (a limit cycle) becomes the homoclinic orbit of a saddle point. This scheme is able to explain accurately quantitative aspects of the transition, like scaling law for the divergence of the period of the oscillation at the bifurcation point.

After a close scrutiny there is at least one aspect that may sound puzzling in this picture: the system under study is described by a 2-D nonlinear Partial Differential Equation, with an infinite-dimensional phase space. Instead, the reported saddle-loop bifurcation minimally needs a 2-D dimensional system with a limit cycle and a saddle point, what is coherent with the fact that the bifurcation *is born* at a Takens-Bogdanov codimension-2 point. One can devise a kind of

slaving principle, in which the slowest modes (with the closest eigenvalues to zero) dominate the slow dynamics. However, the two leading eigenvalues of the saddle point close to bifurcation do not explain the scenario (give the wrong stability for the limit cycle). For all this, we have engaged in showing the reason why such a 2-dimensional reduction is successful in explaining the dynamics, and, in particular, what happens with the stability of the emerging limit cycle.

The main result of this chapter is that it is possible to recover quantitatively, from the full system, the qualitative 2-dimensional sketch of the saddle-loop bifurcation, in which two modes participate: the single unstable mode, and a kind of conjugate stable mode (buried in the sea of stable modes), with the property that both modes are the only two localized modes of the system.

Apart from this kind of fundamental result, the main interest of these results is to prove excitability in an extended system as an emerging property, i.e., not present locally in the spatio-temporal system, but emerging through one of its solutions. Excitability is possible in classes of systems in which an oscillation is destroyed at a bifurcation yielding, at the other side, a fixed point solution. In the present scenario, mediated by a saddle-loop bifurcation, excitability is not generic, and requires the availability of a close enough fixed point solution: the homogeneous solution, in the present case.

Chapter 6

Effect of a Localized Beam on the Dynamics of Excitable LS

In the previous chapter we studied the dynamics of localized structures (LS) in a Kerr cavity pumped homogeneously. This LS become excitable by a saddle-loop bifurcation, and it is characterized by a large excitability threshold and by occurring at any point of space that is properly excited. Since LS excitability emerges from the spatial dependence, it is important to study the effect of breaking the translational symmetry on the excitable dynamics. In optical systems this can be easily done by applying a (small amplitude) localized beam on top of the homogeneous pump. Addressing beams are typically used already to create LS by applying a transient perturbation.

In this chapter we will study the dynamics of LS when a permanent localized addressing beam is introduced, that is, the cavity is pumped with a localized beam on top of the homogeneous pump. The localized beam breaks the translational symmetry of the system and allows on the one hand to control the place where the LS appear, and on the other hand introduces a new route to excitability, that allows a better control of the excitability threshold.

This chapter is organized as follows: In Sec. 6.1 we will introduce the localized addressing beam, and we will study the overall behavior of the system. Then in Sect. 6.2 we will study the instability exhibited by the LS through a SNIC bifurcation. Sect. 6.3 discusses the excitable routes found in this system. Sect. 6.4 and 6.5 discuss the codimension-2 points that organize the overall scenario.

6.1

Overview of the behavior of the system

In this chapter we will consider a pump beam of the form

$$E_I(r) = E_0 + H \exp(-r^2/r_0^2) \tag{6.1}$$

where E_0 is a homogeneous field, assumed real, H the height of the localized Gaussian perturbation, $r^2 = x^2 + y^2$ and r_0 is the width of the Gaussian. For convenience, we write the height of the Gaussian beam as,

$$H = \sqrt{(I_s + I_{sh})\left[1 + (\theta - I_s - I_{sh})^2\right]} - E_0, \tag{6.2}$$

where I_s is the background intracavity intensity (due to E_0) and I_s+I_{sh} corresponds to the intracavity field intensity of a cavity driven by an homogeneous field with a amplitude equal to one at the top of the Gaussian beam, $E_I = E_0 + H$. This directly relates the height of the Gaussian beam H with the equivalent intracavity intensity for a homogeneous pump. Notice that for $I_{sh} = 0$ the pump beam becomes homogeneous, $H(I_{sh} = 0) = 0$, With the inclusion of the localized pump beam the system has now three independent control parameters which for convenience take as the background intensity, I_s, the detuning θ and I_{sh}.

We will consider $r_0 = 1$, this produces a Gaussian perturbation with a size smaller than the typical LS size. Localized pumps of width larger than that of a LS may lead to the presence of multiple structures or azimuth instabilities which will eventually evolve to an extended pattern. For localized pumps of width smaller than the LS, we have observed that a small change in the beam width leads to similar results than the ones shown here for $r_0 = 1$; in fact changing r_0 is similar to change I_{sh}. The most relevant parameter is not the width or the height but its total energy. Thus, for a fixed r_0, I_{sh} is the energy of the Gaussian perturbation.

One of the main consequences of the application of a localized pump is the breaking of the translational symmetry of Eq. (1.87). Solutions are now pinned in the region in which the Gaussian pump is applied. This also affects the transverse profile of the solutions, in particular the fundamental solution is no longer spatially homogeneous but it exhibits a bump as illustrated by the lower inset in Fig. 6.1.

To understand better the effects of the application of a localized pump, a diagram like the one shown in Fig. 5.2, that represents the maximum intensity of the transverse field as a function of I_s is shown in Fig. 6.1, namely for $I_{sh} = 0.3$ and $\theta = 1.25$. The diagram, with three branches, looks qualitatively equivalent to the case of a homogeneous pump and operations such as switching on and off

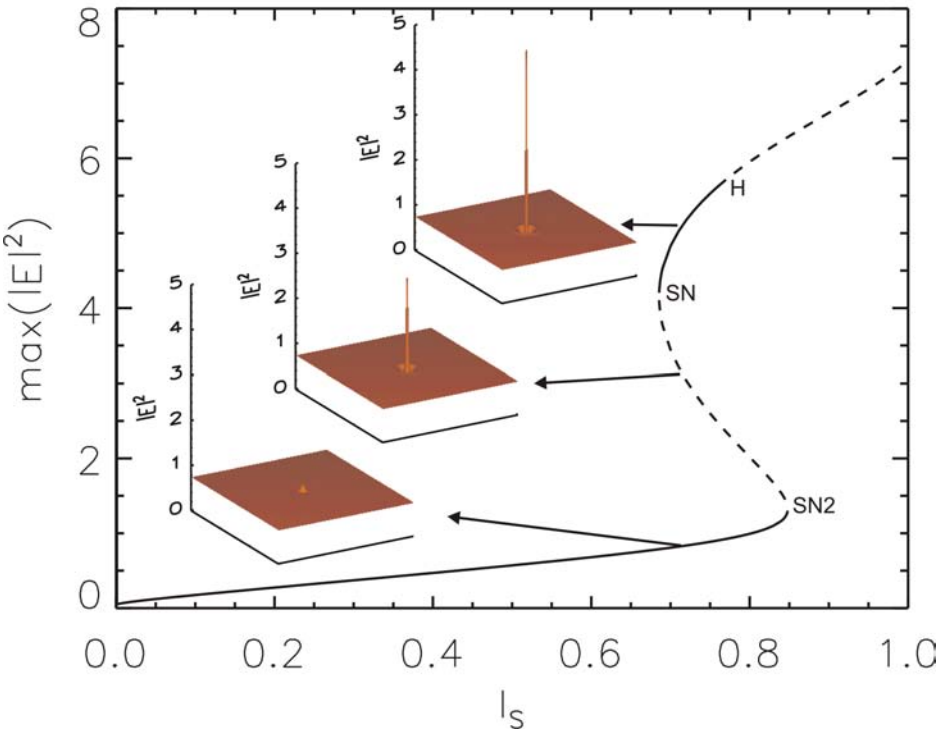

Figure 6.1: Bifurcation diagram, $max(I)$ vs I_s, for a LS for $I_{sh} = 0.3$, $\theta = 1.25$. Solid lines represent stable solutions and dashed lines unstable ones. The insets show the transverse profile of the solutions. All the quantities plotted in this figure as well as in the other figures of this manuscript are dimensionless.

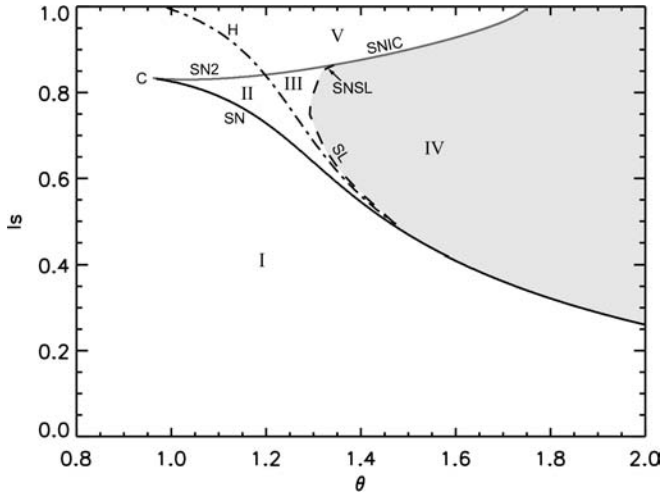

Figure 6.2: Two-parameter I_s vs. θ phase diagram for $I_{sh} = 0.3$. Bifurcation lines are: SN (Saddle-Node); H (Hopf); SL (Saddle-Loop); SNIC (Saddle-Node on the Invariant Circle); SN2 (Saddle-Node off invariant cycle). Regions delimited by bifurcation lines are as follows. I: only the fundamental solution is stable; II: stationary stable LS coexisting with the fundamental one; III: oscillating LS (or oscillons), coexisting with the fundamental solution; IV: excitable region; V: oscillating LS (with no other coexisting solution).

the LS can be performed in a similar way. For example, with the system at the fundamental solution, the upper branch LS can be switched on by applying an additional transient localized beam or equivalently by temporarily increasing I_{sh}

A relevant difference is that for an homogeneous pump the lowest branch (homogeneous solution) extends until the MI at $I_s = 1$, while in the case considered here the fundamental solution merges with the middle branch LS before the MI, in a saddle-node bifurcation (that happens at $I_s = 0.8479$, SN2 point in Fig. 6.1). To understand qualitatively this phenomenon one has to take into account that the homogeneous pump case has many symmetries, some of which are broken when a localized pump is applied. In technical parlance one says that the bifurcation has become imperfect (see, e.g., [101]), with the consequence that a gap in I_s appears making the lower branch disconnected in two branches (the right part of the branch is not plotted in Fig. 6.1 and correspond to solutions unstable to extended patterns).

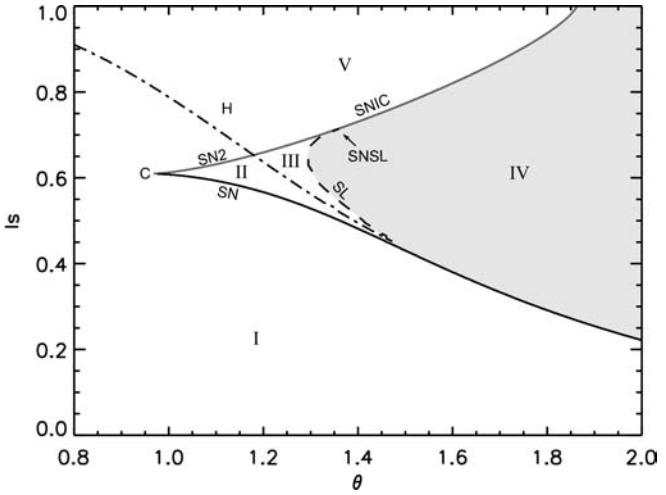

Figure 6.3: Two-parameter I_s vs. θ phase diagram for $I_{sh} = 0.7$. Line and region labeling as in Fig. 6.2.

Exploring now the upper branches, in Fig. 6.1 past the saddle-node bifurcation at $I_s = 0.6857$ (SN point), a pair of stationary (stable, upper branch, and unstable, middle branch) localized solutions in the form of LS are found. In this parameter region, these structures are not essentially different to the solutions found in the homogeneous case [183]. Increasing I_s the stable high-amplitude LS undergoes a Hopf bifurcation.

Overall the scenario found for a localized pump displays a richer variety of dynamical behaviors than in the case of homogeneous pump studied in the previous chapter. Fig. 6.2 shows a phase diagram for a fixed value of the localized pump $I_{sh} = 0.3$. One can compare this figure with Fig. 5.5, corresponding to $I_{sh} = 0$. The effect of breaking the translational symmetry would be to unfold some of the lines at $I_s = 1$ (not visible in Fig. 5.5), that are degenerate with the MI line, and also make the SN line end at $I_s < 1$ (point C in Fig. 6.2). Thus, the effect of a localized pump is to *push* down the SN2-SNIC line (to be explained later), as is clear from Fig. 6.3, that provides a similar plot for $I_{sh} = 0.7$.

Some of the most prominent features of these figures, comparing with the homogeneous pump case, associated to the appearance of the SNIC line (to be discussed in more detail in Sec. 6.2) are that the excitable region, IV in Figs. 6.2-6.3, can have two types of excitable behavior (see Sec. 6.3), both of Class I, as two different transitions to oscillatory behavior are possible, saddle-loop (SL) and

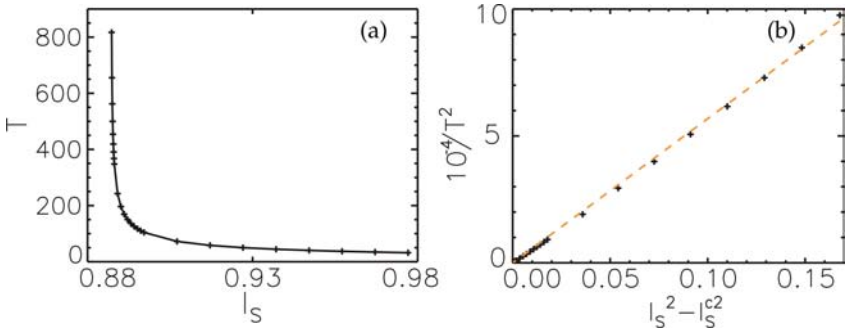

Figure 6.4: (a) Period of the limit cycle T as a function of I_s for $I_{sh} = 0.3$ and $\theta = 1.45$. (b) $1/T^2$ vs. I_s close to the bifurcation point.

SNIC. In addition, one has a new region, V, in which one has a single attractor in the system, that is oscillatory, to be distinguished from region III, in which the system exhibits bistability *, between the (stationary) fundamental solution and an oscillatory upper branch LS. These behaviors, and how they are organized by three codimension-2 points will the subject of Sections 6.4-6.5.

6.2 Saddle-node on the invariant circle bifurcation

A saddle-node on the invariant circle bifurcation (SNIC), that we described in Chapter 1, is a special case of a saddle-node bifurcation that occurs inside a limit cycle. Although this bifurcation is local in (one-dimensional) flows on the circle, it has global features in higher-dimensional dynamical systems [101], so it is also termed local-global or semilocal. In particular, the (stable) manifolds of the saddle and node fixed points transverse to the center manifold are organized by an unstable focus inside the limit cycle. At one side of the bifurcation the system exhibits oscillatory behavior, while at the other side the dynamics of the system is excitable. This mechanism leading to excitability has been found in several (zero dimensional) optical systems [124, 189, 190].

*When speaking about mono and bistability we refer to localized solutions. In general, several extended solutions (patterns) may also be coexisting

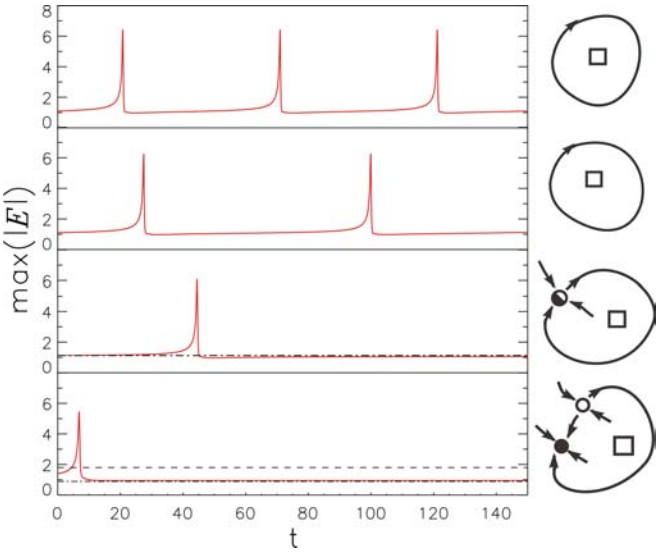

Figure 6.5: Time evolution of the LS amplitude for $I_{sh} = 0.3$, $\theta = 1.45$ and decreasing values of I_s . From top to bottom, $I_s = 0.927, 0.907, 0.8871, 0.8$. In the bottom panel the dashed line corresponds to the amplitude of the unstable LS (saddle) while dot-dashed line corresponds to the stable fundamental solution. These two solutions coincide when the SNIC bifurcation takes place (third panel). The sketches on the right illustrate the phase space dynamics.

When approaching the bifurcation from the oscillatory side the period lengthens and becomes infinite. Quantitatively the period as a function of a parameter exhibits a inverse square root singular law [101],

$$T \quad \propto \quad [I_s^2 - (I_s^c)^2]^{-1/2} \, . \tag{6.3}$$

This can be used to distinguish the SNIC from other bifurcations leading to oscillatory behavior (e.g. from the saddle-loop bifurcation with a logarithmic singular law [101, 182, 183]). Fig. 6.4 shows the period of the oscillations as a function of I_s obtained by numerical simulations of Eq. (1.87). In the inset of Fig. 6.4 we plot $1/T^2$ vs. I_s^2 close to the bifurcation point. The linear dependence obtained corroborates the scaling law and that the transition takes place through a SNIC bifurcation.

The overall route exhibited by the system along a vertical cut in Fig. 6.2 at $\theta = 1.45$ is illustrated in Fig. 6.5, as the parameter I_s is decreased from the top to the bottom of the figure. Thus, the figure shows the transition from oscillatory behavior (top panel) to stationary (fourth panel) through the occurrence of a SNIC bifurcation (third panel). Lengthening of the period can be seen in the second panel. The sketches shown in the right column of Fig. 6.5 illustrate the structure of the phase space. The validity of this scenario is further reinforced with the quantitative analysis presented in Section 6.5.

6.3 Excitability

An interesting aspect of this scenario is that in region IV one can have excitable behavior through two different mechanisms. On the one hand, and similarly to the behavior analyzed in Chapter 5 and Refs. [182, 183], close enough to the SL line one has excitability if the fundamental solution is appropriately excited such that the oscillatory behavior existing beyond the SL is transiently recreated. The second mechanism takes place close to the SNIC line, where the oscillatory behavior that is transiently recreated is that of the oscillations in region V. Both excitable behaviors exhibit a response starting at zero frequency (or infinite period), as both bifurcations are mediated by a saddle, whose stable manifold is the threshold beyond which perturbations must be applied to excite the system. In neuroscience terminology, both excitable behaviors are class (or type) I [107, 108], although there are important differences between them. The SNIC mediated excitability is easier to observe than the one associated to a saddle-loop bifurcation for two reasons. First, it occurs in a broader parameter range due to its square-root scaling law (6.3), with respect to the SL excitability *. Second the excitable threshold can be controlled by the intensity of the localized Gaussian beam, that effectively approaches the fixed point and the saddle in phase space, allowing to reduce the threshold as much as desired (by approaching the SNIC line). Within region IV one can find a typical crossover behavior for the threshold, as it increases from zero (at the SNIC line) to the (finite) value characteristic of the SL bifurcation as one approaches this line.

Fig. 6.6 shows the dynamics of the excitable fundamental solution in region IV, namely for the parameters corresponding to the fourth panel in Fig. 6.5, upon the application of different localized perturbations, one below the excitable threshold

*For saddle-loop mediated excitability the scaling law is logarithmic, implying that the frequency increases very fast from zero in a very narrow range, and, thus, its class I features can be easily missed experimentally [108].

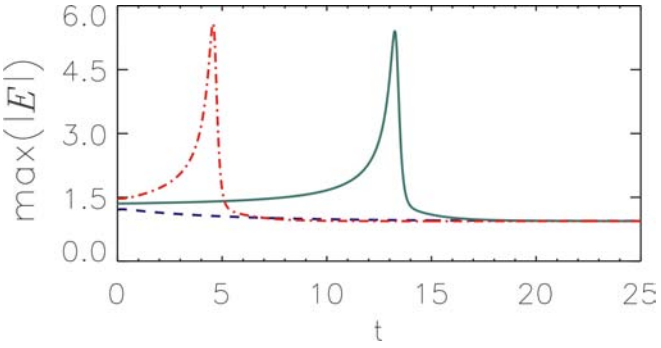

Figure 6.6: Evolution of the maximum of the field amplitude after applying a localized perturbation to the fundamental solution. The perturbation has the shape of the unstable stationary LS (saddle), that is scaled by 0.95 (blue dashed line); 1.01 (green solid line) and 1.1 (red dotted line). Here $I_{sh} = 0.3$, $I_s = 0.8$, and $\theta = 1.45$.

and two above. As expected, the perturbation below threshold relaxes directly to the fundamental solution while the above threshold perturbations elicit first a large response of the system in the form of an excitable soliton which finally relaxes to the fundamental solution. The excitable excursion takes place at a later time as the smaller is the distance to the threshold (a signature of Class I excitability). Finally, the shape of an excitable excursion in two-dimensional space is shown in Fig. 6.7.

6.4 Cusp codimension-2 point

In the two-parameter phase diagrams in Figs. 6.2-6.3 one can see a point marked with a 'C' that was not found in the homogeneous case [*]. This point represents a Cusp codimension-2 bifurcation point [105], namely a point in which two saddle-node curves merge (see Chapter 1 for details). This cusp point, that involves only stationary (saddle-node) bifurcations, is also known as the Cusp Catastrophe [191]. For parameter values just at the left of the Cusp the bump of the fundamental solution exhibits a rapid increase. Fig. 6.8 shows the sharp, but

[*]The Cusp coordinates are $I_s = 0.834$, $\theta = 0.961$ for $I_{sh} = 0.3$ (Fig. 6.2), and $I_s = 0.61$, $\theta = 0.968$ for $I_{sh} = 0.7$ (Fig. 6.3)

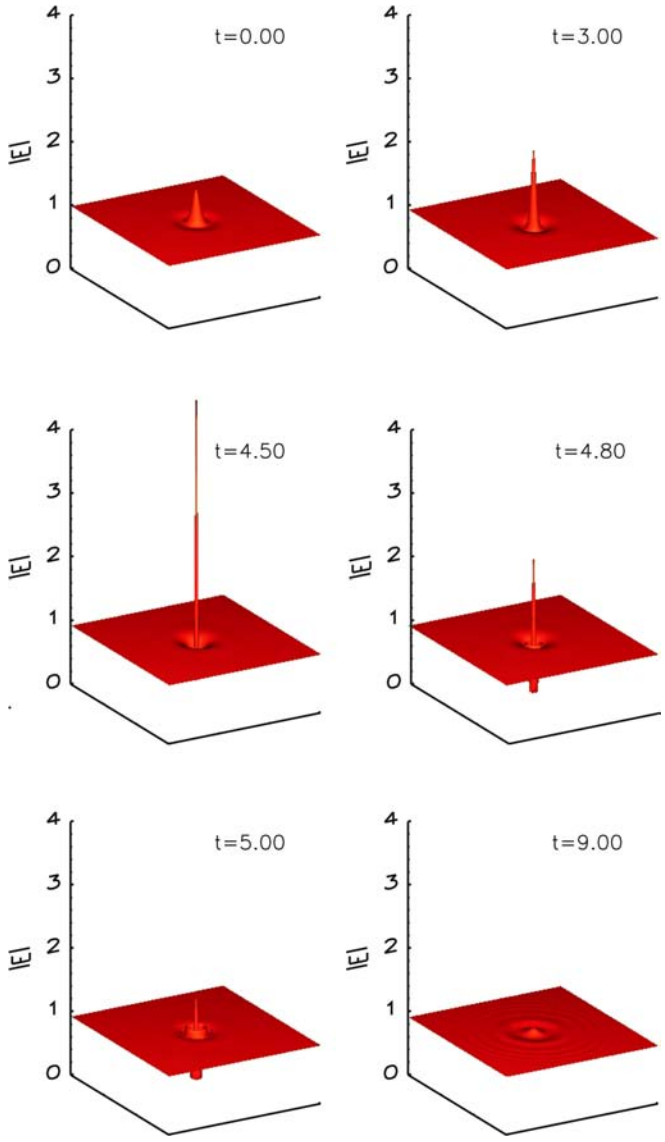

Figure 6.7: Transverse profile of $|E|$ at different times of the dotted line in Fig. 6.6.

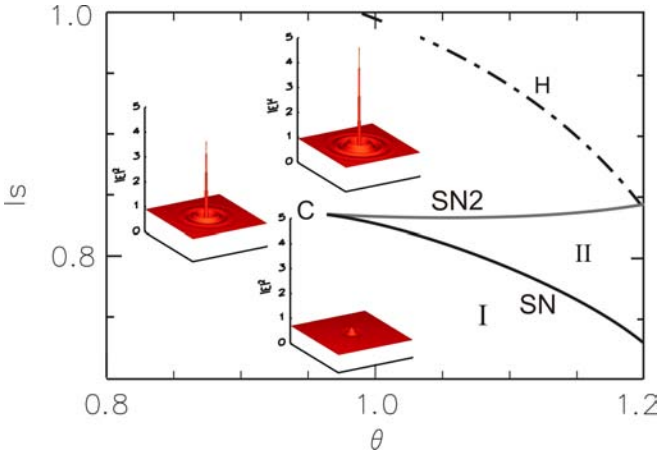

Figure 6.8: The fundamental solution for three points in the (I_s, θ) parameter space, for $I_{sh} = 0.3$, around the Cusp codimension-2 point. The coordinates are (bottom to top): $I_{sh} = 0.7, \theta = 0.9$; $I_{sh} = 0.85, \theta = 0.85$, $I_{sh} = 0.95, \theta = 0.95$.

smooth, change in the shape of the fundamental solution for three parameter values around the cusp point within region I. Instead, if one is to the right of the 'C' point this increase cannot be accommodated smoothly and a double fold occurs, such that three branches appear: two stable, upper and lower branches, and one unstable, middle branch, and thus bistability makes its appearance. The two folds, codim-1, merge critically at the cusp point, codim-2. Decreasing I_{sh} the Cusp moves up towards $I_s = 1$, so in the limit of homogeneous pump it can not be seen due to the presence of the MI instability. The smooth connection between the fundamental branch and the upper branch exhibiting LS is an outcome of the symmetry breaking induced by the localized pump which has made the MI bifurcation to become imperfect.

6.5 Saddle-node separatrix-loop codimension-2 point

The subject of the present section is to discuss the Saddle-Node Separatrix Loop bifurcation point designated with 'SNSL' in Figs. 6.2-6.3. A SNSL is a local-global codimension-2 point in which a saddle-node bifurcation takes place simultane-

ously to a saddle-loop, such that the orbit enters through the noncentral (stable) manifold (see Chapter 1). The unfolding of a SNSL point leads to the scenario depicted in Fig. 6.9 *. There is a line of saddle-node bifurcations (in which a pair of stable/unstable fixed points are created) that at one side of the SNSL is a saddle-node bifurcation off limit cycle (SN2) while at the other side is a SNIC bifurcation (the saddle-node occurs inside the limit cycle). A saddle-loop (SL) bifurcation also unfolds from the SNSL point, tangent to the SN2 line. From the other side, a special curve depicted with a dotted line in Fig. 6.9 should appear (cf. Fig. 22 in Ref. [107]). It is not a bifurcation line, but instead it is a special line in which the approach to the node point is through the most stable direction, namely the direction transverse to the central manifold at the SNIC/SN2 (and SNSL) bifurcations (for these reasons we also call this dotted line the 'pseudo-bifurcation' line). This, in principle nongeneric, curve, that emerges in the unfolding of the SNSL point, is necessary for consistency on the excursions around the SNSL codimension-2 point. At the pseudo-bifurcation the topological cycle is reconstructed, namely the stable fundamental solution and the middle branch LS (saddle), become points belonging to the circle that latter will become the limit cycle. Before the pseudo-bifurcation the unstable manifold of the saddle enters towards the stable solution from the same side than the saddle, while after the pseudo-bifurcation it enters from the opposite side.

The SNSL point separates two possible ways in which the system can go from oscillatory region III (where the limit cycle coexists with the stable fundamental solution) to oscillatory region V (where the fundamental solution does not exist).

For $\theta > \theta_{\mathrm{SNSL}}$ the scenario is as described in Section 6.2, namely the middle and lower branches coalesce in a SNIC bifurcation. The main feature of this bifurcation is that it occurs *on* the limit cycle, leading to the excitable behavior of region IV. This scenario can be confirmed using the mode projection technique described in the Appendix B (as we did in Chapter 5), that allows to obtain in quantitative form the phase space of an extended system (described, e.g., by a PDE), that strictly has an infinite dimension, but whose relevant dynamics is low-dimensional. In this case, like in the case of a saddle-loop bifurcation studied in the previous chapter, we will argue that there are just two modes that are relevant, at least in the region close to the SNSL codimension-2 point. Fig. 6.10 shows the spectrum of eigenvalues (linear stability analysis for the fundamental solution) at the SNIC bifurcation and close to the SNSL. The spectrum has a continuous part with eigenvalues lying along the line $\mathrm{Re}(\lambda) = -1$, and also a discrete part which is symmetric with the respect to this line. It turns out that

*Note that the same qualitative behavior of this unfolding is reproduced by the one in Fig. 1.22, where we considered the normal form in one dimension with a reset condition.

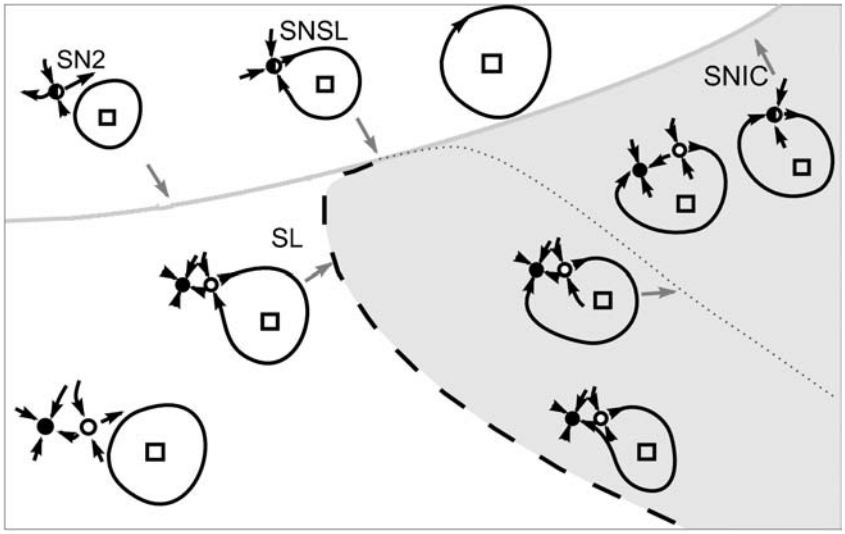

Figure 6.9: Sketch of the parameter space near the SNSL point, showing the unfolding of bifurcation lines, and adapted to the geometry in Figs. 6.2-6.3.

there are only two eigenmodes which are localized in space, while all the other eigenmodes are spatially extended. The two localized eigenmodes correspond to the most stable mode and to the one that becomes unstable. These two modes, shown in Fig. 6.11, are the only relevant for the dynamics of the LS close to the stable fixed point, since the projection of a localized solution onto any of the extended modes is negligible.

Fig. 6.12 shows a quantitative reconstruction of the phase space. β_1 (β_2) corresponds to the amplitude of the projection of the trajectory along the unstable (most stable) eigenmode. Panel (a) represents a trajectory in the excitable region IV, close to the SNSL and below the pseudo-bifurcation line. Panel (b) shows a zoom of the trajectory close to the saddle (open circle) and the stable fundamental solution (filled circle). The excitable trajectory departs form the saddle and after long excursion in phase space arrives to the fundamental solution from below (that is, from the side of the saddle). Notice that while close to the fixed points the dynamics fits very well in a 2-dimensional picture, away from them the lines crosses, indicating that the full LS dynamics in phase space is not confined to a plane. Panel (c) corresponds to the pseudo-bifurcation, so that the trajectory arrives at the fundamental solution along the most stable direction. Panel (d) is just after the pseudo-bifurcation with the trajectory arriving from the other

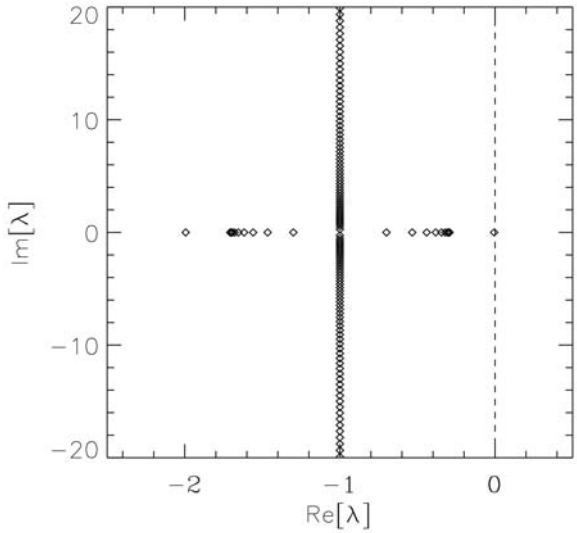

Figure 6.10: Spectrum of the fundamental solution at the SNIC bifurcation for $I_{sh} = 0.7$, $I_s = 0.707$, and $\theta = 1.34$ (close to the SNSL).

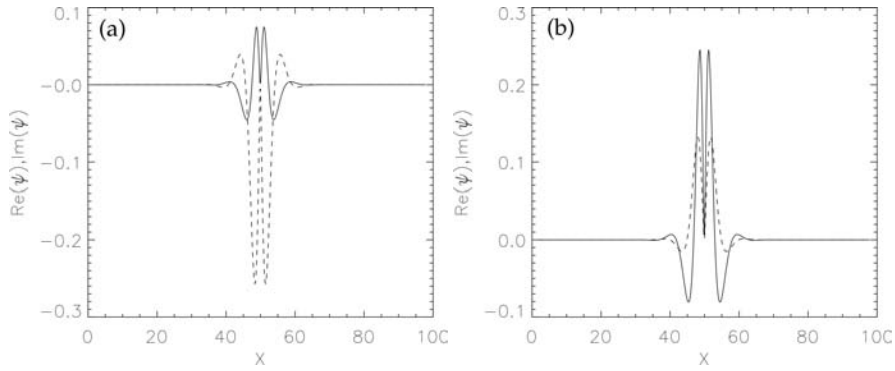

Figure 6.11: Transverse cut of the most stable (left) and unstable (right) eigenmodes of the linear spectrum shown in Fig.6.10. The solid (dashed) line indicates the real (imaginary) part of the eigenmode.

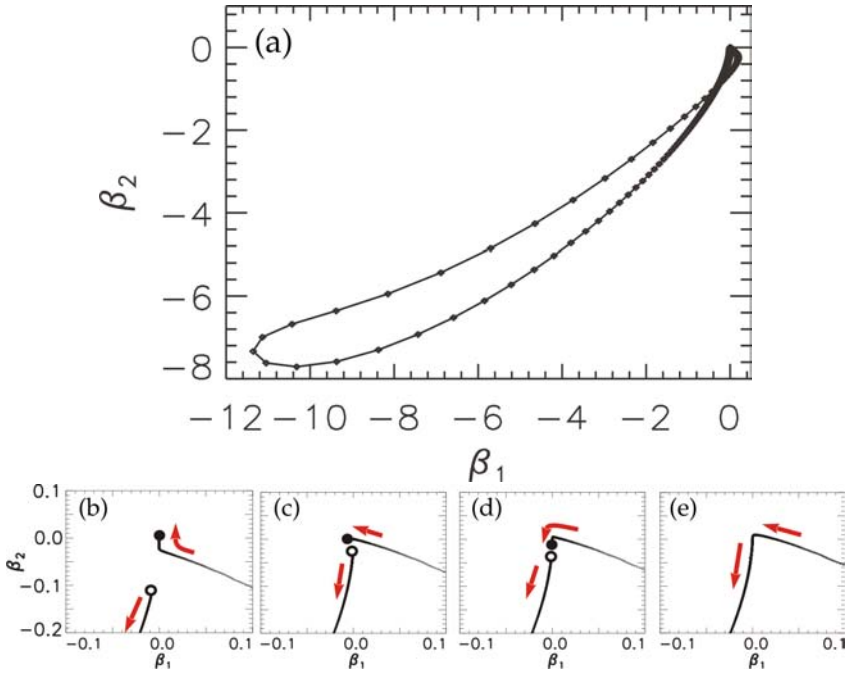

Figure 6.12: (a) Full trajectory in the phase space close to the SNIC (I_s = 0.863). The smaller panels show a zoom of the region in the phase space close to the fixed point. (b) I_s = 0.863, (c) I_s = 0.8634575, (d) I_s = 0.8635, and (e) I_s = 0.864. Here I_{sh} = 0.3 and θ = 1.34.

side. Finally panel (e) corresponds to parameters in the oscillatory region V just after the SNIC bifurcation. Notice that the pseudo-bifurcation line is very close to the SNIC bifurcation since we have taken parameters close to the SNSL and at the SNSL both lines originate tangentially. As expected, the quantitative picture agrees with the qualitative picture as one crosses the SNIC bifurcation in the right panels of Fig. 6.5.

For $\theta < \theta_{SNSL}$ the scenario is quite different, as the middle and lower branches now coalesce off the limit cycle, SN2, what implies that the behavior of the system is oscillatory on both sides of the SN2 line, not excitable [*] and instead one crosses

[*]Due to the bending of the SL line when approaching the SNSL there is a region in which in vertical paths in parameter space crosses the SL line twice. Qualitatively there is no difference between crossing twice or none the SL line, as one is in the oscillatory bistable region III when approaches the SN2 line.

the SN2 line. This means that one is in a bistable oscillatory regime, and in crossing the SN2 line a saddle-node off the invariant cycle bifurcation occurs. SN2 involves the middle and fundamental branches (while SN involves the upper and middle branches). So, in the end this is nothing else that another way of entering region V, of monostable oscillatory behavior, but instead of reconstructing the limit cycle, here the fundamental stationary solution is destroyed.

Therefore, and having in mind the behavior for $\theta \to \infty$ discussed in previous chapter, the overall scenario depicted in Figs. 6.2-6.3 is organized by three codimension-2 points: a Cusp point, from which two saddle-node bifurcations emerge (SN and SN2); a SNSL point from which a SNIC line emerges, and that organizes the SN2 and SL lines around; and a Takens-Bodgdanov point, occurring apparently at infinite detuning, where the SN, Hopf and SL are tangent, and that can be seen as the birth of both the Hopf and SL lines. The Takens-Bogdanov point was numerically shown to be present in the homogeneous case (Sec. 5.6). It is reassuring that the saddle-loop bifurcation line connects two of the codimension-2 points, as it is not in some sense generic, * and one does not expect that it emerges *out of the blue sky*. The scenario composed by these three codimension-2 bifurcations has been reported in other systems [192], and from a theoretical point of view, it can be shown that it appears in the unfolding in 2-dimensional parameter space of a codimension-3 degenerate Takens-Bogdanov point [193].

In the limit of homogeneous pump the SN2 and SNIC lines approach the MI line at $I_s = 1$, which, therefore, also contains the Cusp and the SNSL codimension-2 points. At the Cusp the SN (responsible for the existence of LS) originates while at the SNSL the SL (originated at the Takens-Bogdanov and responsible of the LS excitability observed for homogeneous pump) ends. Notice that for homogeneous pump close to $I_s = 1$ azimuthal instabilities renders the LS unstable to a pattern so it is difficult to study the SN and specially the SL lines in that region. Using a localized pump and then taking the limit to homogeneous pump circumvents these limitations.

*Because it implies that the a limit cycle has a tangency simultaneously with the stable and unstable manifolds of a saddle point.

6.6 Conclusions

In this chapter we have presented a detailed study of the instabilities of localized structures in under the application of a localized Gaussian beam. Since experimentally LS are typically switched on by applying a transient addressing beam the situation discussed here can be realized just applying it on a permanent basis. The LS are sustained by a balance between nonlinearity and dissipation, as in the case of a homogeneous pump, although now these effects interact with the localized pump. The localized pump helps to spatially fix the LS and to control some of its dynamical properties. After the saddle-node bifurcation that creates the LS, it starts oscillating and overall exhibit a plethora of bifurcations that are shown to be organized by three codimension-2 points: a Takens-Bogdanov point, (which is also present for homogeneous pump as discussed already in Chapter 5), a Cusp, and a Saddle-Node Separatrix Loop (SNSL) points. In this scenario a saddle-loop bifurcation connects the Takens-Bogdanov and the SNSL and the Cusp is connected to the other codimension-2 bifurcations by two saddle-node lines. A line of SNIC bifurcations originates at the SNSL while at the Takens-Bogdanov a Hopf bifurcation line meets tangentially a saddle-node and the saddle-loop lines. Compared with the homogeneous case studied in Chapter 5 we can see how the presence of a localized Gaussian beam introduces new bifurcations (the SNIC and the SNSL bifurcations) that change the behavior of the system.

The simultaneous presence in the system of two bifurcations that are associated to excitable behavior (saddle-loop and SNIC) enriches and completes the picture discussed for the case of a homogeneous pump. In fact the region for which excitable behavior is reported, in which the only attractor in the system is the fundamental solution, leads to two different Class I behaviors (starting at infinite period). In the excitable region one goes smoothly from no threshold at the onset of the SNIC line to a finite threshold at the onset of the saddle-loop line. In fact, the excitable behavior mediated by a SNIC, and reported in this chapter, should be easier to observe both numerically and experimentally, and present some practical features that make it more suitable for practical applications. In particular, the excitable threshold can be controlled by the intensity of the localized beam. With an array of properly engineered beams, created for instance with a spatial light modulator, one could create reconfigurable arrays of coupled excitable units to all-optically process information. This is the subject of the next chapter.

Chapter 7

Logical Operations Using Localized Structures

In this chapter we explore the possibility of using excitable localized structures to perform logical operations. Computational properties of waves in chemical excitable media (e.g. the Belousov-Zhabotinsky reaction) have been used to solve mazes [194], to perform image computation [195], and also logic gates have been constructed from these (chemical)systems [196–198]. After all, excitability is a property exhibitted by neurons, and used by them to perform useful computations [199], in a way that is different than the more usual attractor neural networks [200, 201].

Optical computing, via photons instead of electrons, has long appealed researchers as a way of achieving ultrafast performance. Photons travel faster than electrons and do not radiate energy, even at fast frequencies. Despite the constant advances and miniaturization of electronic computers, optical computing remains a strongly studied subject. Probably the strategy to follow is not to seek to imitate electronic computers, but rather to try to fully utilize the Physics of these systems, e.g., their intrinsic parallelism.

Most of the systems studied in optical computing applications imply light propagation, for example optical correlators, already commercially used in optical processing applications [202]. Instead, with the goal of designing more compact optical schemes, localized structures have emerged as a potentially useful strategy for information storage, where a bit of information is represented by a LS. In this chapter we will take this idea a step further and discuss the potential of LS, for carrying out computations, i.e., not just for information storage. In particular, we will show how logic gates can be designed using localized structures, namely

	Input 1	Input 2	Output
OR	0	0	0
	1	0	1
	0	1	1
	1	1	1
AND	0	0	0
	1	1	0
	0	1	0
	1	1	1
NOT	0	1	
	1	0	

Table 7.1: Logic gates

the AND, OR and NOT gates, as by combination of them one can construct any logical operation, in particular the NAND gates used in silicon electronics.

In Sect. 7.1 we discuss how to implement the AND and OR gates, which involve two inputs and one output. In Sect. 7.2, we discuss the implementation of a NOT gate involving only one input and one output.

7.1 AND and OR gates

From now on, we consider $Is = 0.85$ and $\theta = 1.45$, fixed in all computations, using I_{sh} and the distance between the excitable LS as free parameters. Similar results would be obtained for different values of I_s and θ.

In this section we will consider the localized structures in the excitable regime studied in the previous chapter. This means that the position and the excitability threshold of the LS are controlled by the Gaussian beam. As we will show in Chapter 8, when several of these excitable localized structures are coupled, a transition to an oscillatory behavior is possible. In this chapter we will work in a regime in which the LS remains stationary in time unless perturbed, just bellow the oscillatory threshold. In particular we consider three excitable LS in a linear arrangement, with a separation d between them. Three permanent Gaussian localized beams are then applied I_{sh}^{I1} and I_{sh}^{I2} for the input LS and I_{sh}^{O} for the output LS. The Gaussian beams fix the spatial position of input and output LS. The two outer LS will act as the inputs of the gate, while the central one will

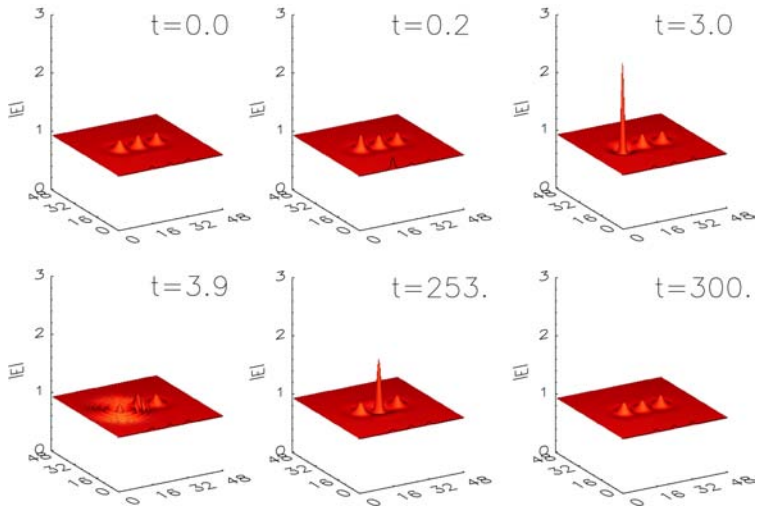

Figure 7.1: OR logic gate with 1-0 input. $I_{sh}^{I1} = I_{sh}^{I2} = 0.41$, $I_{sh}^{O} = 0.4075$. $d = 8.25$

be the output. If there is a excitable excursion in the central localized structure it is interpreted as a "1" and if there is no excitable response as a "0".

Superthreshold perturbations (i.e. causing an excitable excursion) will be considered as bit "1", while subthreshold (or the absence of) perturbations will be considered as bit "0". If there is a excitable excursion in the central localized structure the output of the gate is considered as a "1" and if there is no response as a "0". Physically, the interaction is mediated by the tails of the structures and the ripples that radiate from the LS, dissipating energy to the surroundings, during the excitable excursion.

To better understand the way in which the logical gates work, we will first analyze the OR gate (Table 7.1). We have built these gate by using a distance between structures of $d = 8.25$, and the following values for the intensity of the localized beams: $I_{sh}^{I1} = I_{sh}^{I2} = 0.41$ for the two input LS and $I_{sh}^{O} = 0.4157$ for the output LS. The perturbation corresponding to a "1" in an input localized structure is applied by suitably modulating I_{sh}^{I} such that the LS crosses the excitability threshold, exhibiting an excitable excursion. In Fig. 7.1 we show the dynamics when one of this perturbations is applied. In this case we increase I_{sh}^{I1} by one half for one unit of time (this corresponds to a ("1", "0") input). For this input the output of this gate is an excitable excursion of the central LS, namely a "1". Applying a similar perturbation to I_{sh}^{I2} (corresponding to ("0",

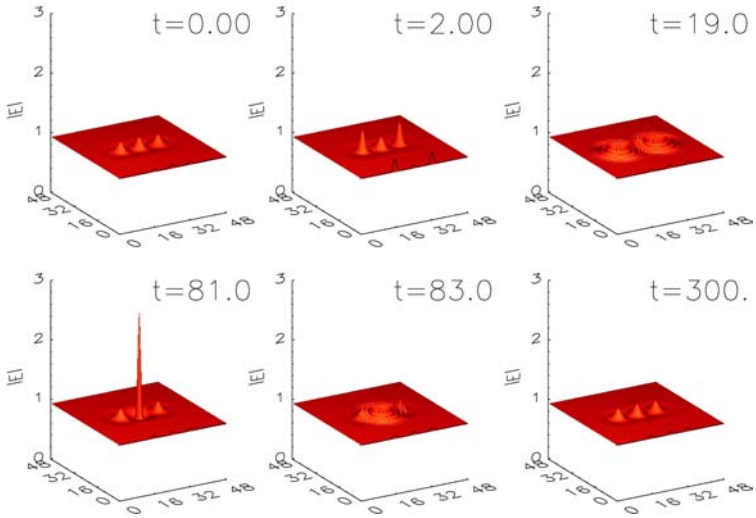

Figure 7.2: OR logic gate with 1-1 input. Parameters as in Fig. 7.1

"1")), the same result is obtained. Finally, if we simultaneously apply the same perturbation to both I_{sh}^{I1} and I_{sh}^{I2} (corresponding to ("1", "1")), a similar excitable excursion is obtained for the central (output) LS, as shown in Fig. 7.2.

An AND (Table 7.1) logic gate built from excitable localized structures can be designed by placing three excitable structures in line a bit further away, so that now, due to the larger distance between two structures, one pulse of the input LS is not enough to excite a response in the output one. In particular we take $d = 9$, and the same localized beam amplitude for the three LS $I_{sh}^{I1} = I_{sh}^{I2} = I_{sh}^{O} = 0.4075$. Increasing I_{sh}^{I1} by one half for one unit of time (corresponding to a ("1", "0") input) there is no excitable excursion at the output LS, as shown in Fig. 7.3. Instead, if one excites the two inputs at the same time (corresponding to a ("1", "1") input), an excitable response is generated at the output LS (Fig. 7.4).

7.2 NOT gate

The NOT operation has a single input (Table 7.1), instead of two as in the previous cases. Moreover, this gate should produce an output when no input is given, so a different approach is needed now. Thus, a single structure in the oscillatory

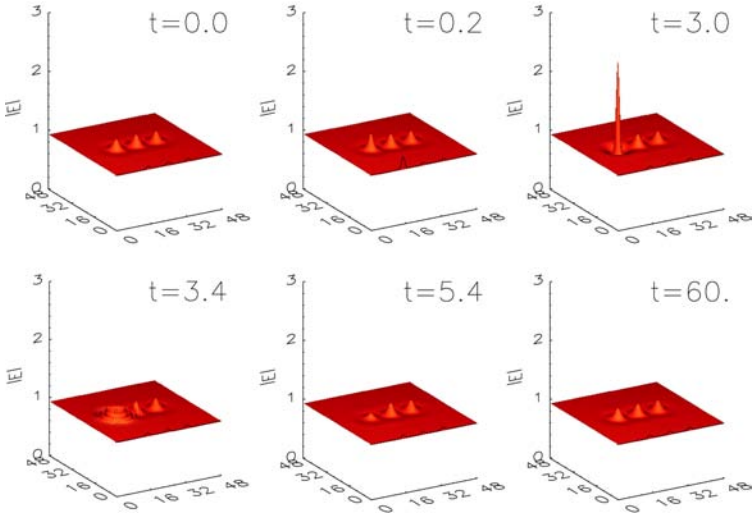

Figure 7.3: AND logic gate with 1-0 input. For all the LS $I_{sh}^{I1} = I_{sh}^{I2} = I_{sh}^{O} = 0.4075$. $d = 9$

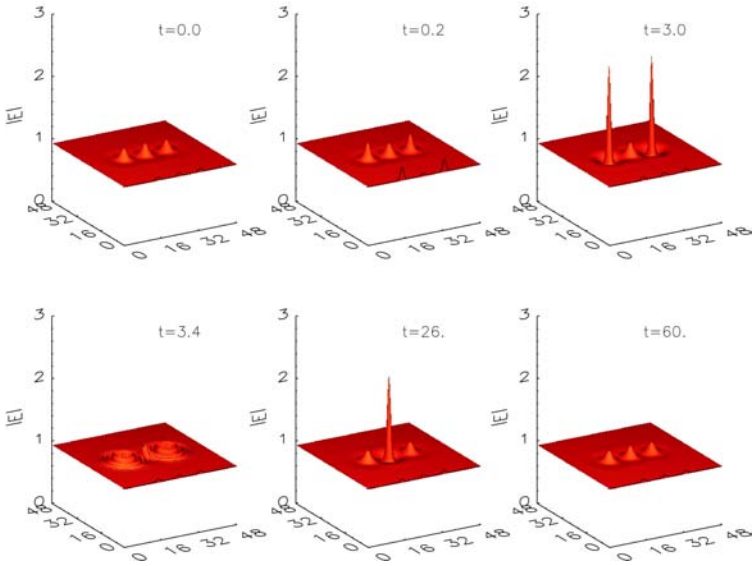

Figure 7.4: AND logic gate with 1-1 input. For all the LS $I_{sh} = 0.4075$. $d = 9$

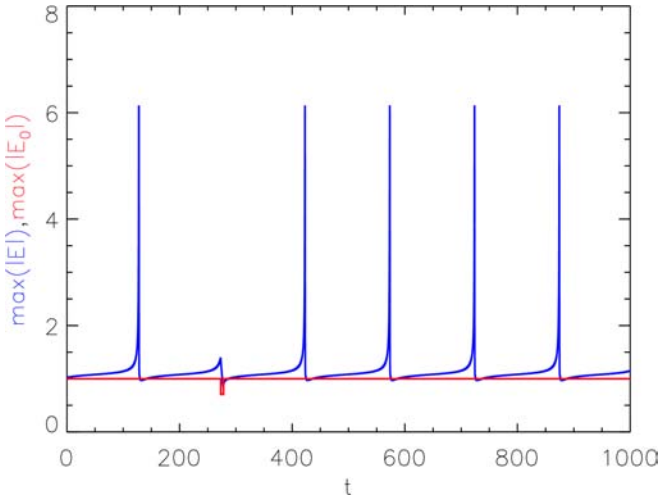

Figure 7.5: NOT logic gate. $I_{sh} = 0.3$, $I_s = 0.8921$

regime will be used, and the input and output takes place at the same LS. When there is no input, since the LS is oscillating, a continuous train of pulses is produced. These pulses are similar to the previous excitable excursions, therefore, the gate is producing a continuous train of "1"'s for "0" input. The frequency of the oscillations can be used as an intrinsic clock setting the pace at which successive logical operations are performed.

The input will be a perturbation with the opposite phase of I_{sh}, decreasing the addressing beam for a short period of time and setting the system bellow the oscillatory threshold. In Fig 7.5 a perturbation (corresponding to a "1" input) is applied at time $t = 270$ by decreasing I_{sh}^{I1} by one half during 5 time units, then one cycle of the oscillations is suppressed and the output is "0". The duration and intensity of the perturbation has been chosen arbitrarily just to demonstrate the operation mechanism of the logic gates, but this gates would work with any temporal shape of the perturbation by properly tuning its intensity. This point becomes relevant when we think on doing a series of operations, which will imply coupling several of this gates by injecting the output of one of them into the other. Therefore the shape of the perturbation will be given by the temporal evolution of the output LS

7.3 Conclusions

In this chapter we analyzed the possibility of creating logic gates by using the dynamics of localized structures. In particular, by appropriately coupling three excitable structures we were able to construct both an AND and an OR gate. Then we have shown how a NOT gate can be constructed using an oscillatory LS.

It is important to stress that, these results are independent of the Kerr cavity model that we studied, and that they could be realized in any system with localized structures that present oscillatory and excitable dynamics. The advantages of this computational method are its intrinsic parallelism (several logic gates can be operated in the same cavity at the same time) and the fact that different logic gates can be realized in the same system by changing only the position and intensity of the localized beams. This constitutes an easily reconfigurable system where a logic circuit could be implemented as a "mask" of localized beams.

Besides the possible difficulties of its experimental realization, a drawback of this method is the intrinsic slowness of the excitable behavior. Due to the bottleneck that exist near the saddle (see Chapter 6) the time that takes to the trajectory to leave this zone of the phase space is large compared with the other time scales of the system. This could constitute a speed limit for the operations. In principle all computation using Class I excitable systems (including neurons) suffer from this limitation.

Chapter 8

Interaction of Oscillatory Localized Structures

In the previous chapters we focused on the study of one aspect of the dynamics of localized structures, namely, excitability. We have shown the existence of excitable LS, how the properties of the excitability can be controlled introducing a localized addressing beam and, furthermore, how this LS can be used to process information. It was also shown that near the excitable regime there is a region where the LS oscillate (in fact, this the existence of this region is a necessary condition for excitability). In this chapter we will focus on the study of such oscillating localized structures, more specifically we will study how two oscillating LS interact, and the dynamical regimes that emerge from the interaction.

The oscillating LS are an example of *non-punctual oscillators*, i.e. oscillators with an internal structure. The interaction between such oscillatory structures through the tails can not be, in general, reduced to a simple coupling term between oscillators, but it modifies the internal structure of the oscillations itself, affecting the dynamics in a nontrivial way. The interplay between the coupling and the internal structure of non-punctual oscillators is a general phenomenon not well understood, and this chapter aims to be an approach to the subject by means of the study of these oscillating LS.

We will focus in the case of the homogeneously pumped Kerr cavity, described by Eq. (5.1). In this case it has been shown, both theoretically and experimentally, that stationary LS interact through their tails in such a way that only a discrete set of equilibrium distance is possible between two LS.

We will start in Sec. 8.1 by studying how the neutral modes of the system change due to the interaction, then in Sec. 8.2 we will show how a similar change occurs in the Hopf unstable modes and how new oscillatory regimes arise from this change.

8.1 Equilibrium distances and Goldstone modes

Throughout this chapter we will set $I_s > 0.83$, and $\theta = 1.27$. This corresponds to a region of oscillatory structures [182, 183]. This value of I_s is close to the modulational instability that occurs at $I_s = 1$ [182], and because of this the LS have large tails. As the interaction between the structures is mediated by these tails, working in this region has the advantage that the interaction is strong and its effects are more evident.

Localized structures in this system have an intrinsic intensity profile with spatially oscillatory tails and, since the system is translationally invariant, the structures are free to move once created. When two structures are placed close to each other, the presence of an adjacent structure breaks the translational invariance setting only a discrete set of positions at which the structures can anchor, given by the intensity profile of the tails [*]. Then if the structures are placed at arbitrary positions they will move until they sit at the zeros of the gradient of this intensity profile. This locking has been mainly studied both from theoretical and experimental [177, 178, 203, 204] point of view for stationary localized structures only.

Similarly to what happens with stationary LS, when two oscillatory localized structures are placed close to each other they move until they get locked by tail the interaction. For the selected parameters this interaction produces three equilibrium distances that are $d_1 = 7.816, d_2 = 15.82$ and $d_3 = 19.93$. Beyond d_3 the interaction is so weak that the structures can be considered as independent.

The movement of the structures from an arbitrary position towards the equilibrium distances is very slow compared with the oscillation period, and increases as the initial distance between the structures increases. Therefore we will restrict ourselves to study the behavior of the system when the structures are at the equilibrium distances, to avoid the transient time and complex effects introduced by the movement of the LS.

[*]It is important to notice that the intensity profile of the tails of each structure is modified by the presence of the other. Therefore, the intensity profile sensed by one structure is not just the one given by the tails of the other but an effective profile emerging from the interaction.

As was previously stated, when only one structure is present it is translationally invariant, i.e. is free to move in an arbitrary direction. Therefore the solution has two Goldstone modes (i.e. with zero eigenvalue) associated to the translational invariance in two orthogonal directions (due to the radial symmetry of the LS these two directions are orthogonal but arbitrary). As expected, the shape of these modes correspond to the derivative of the field along the respective direction [205], as can be seen in Fig.8.1. These modes and its stability have been computed following the procedure detailed in Appendix C.

If we now place two structures at a distance where the interaction is negligible the system will have two pairs of Goldstone modes corresponding to the translations of each LS independently. Instead, if the LS are placed at one of the equilibrium distances the structures are no longer free to move arbitrarily, in particular the movement of one structure in the direction of the other is strongly damped because of the interaction. The other three collective correspond to the rigid motion and rotation of the two structures complex (in this case the two orthogonal directions of motion are given by the symmetry axes of the structures complex). This is reflected in the spectra of the LS: the mode inducing translations of the structures in the direction of each other stops being neutral, meaning that its correspondent eigenvalue becomes negative ($\lambda = -0.0131$). This can be seen in Fig. 8.2 where we plot the modes with their respective eigenvalues for a pair of interacting structures.

This degeneracy breaking mechanism is crucial to understand the interaction of this LS, since it also appears for other modes and determines the dynamics in the linear regime close to bifurcations.

8.2 Oscillations of interacting LS

A single LS undergoes a Hopf bifurcation at $I_s = 0.83$ and starts to oscillate. At the bifurcation point this solution has then two complex conjugate eigenvalues whose real part becomes positive with an imaginary part different from zero. If we now consider two very far apart (non interacting) structures the system has globally two degenerate pairs of Hopf unstable eigenvalues. Since in this case the structures are independent from each other, they become simultaneously unstable at $I_s = 0.83$ and the LS can oscillate at any relative phase.

If the two LS are now placed closer together, at one of the equilibrium positions, the structures are no longer independent. Now the interaction breaks the degeneracy of the spectrum splitting the eigenvalues, as happens with the Goldstone

modes. The eigenvalues split in two different pairs of complex conjugates: a pair corresponding to in-phase oscillations and other to anti-phase oscillations (Fig. 8.3). Since the eigenvalues of these modes are no longer degenerate, increasing the driving one of these two pairs will cross the Hopf bifurcation first (see Fig. 8.4). Although the splitting takes place mainly in the direction of the real axis, the imaginary part is also slightly modified, so the two new cycles have different frequencies.

For $d = d_3$ the interaction is very weak, and the degeneracy is merely broken. The real part of the eigenvalues corresponding to the in-phase and anti-phase oscillations become positive with a difference in I_s of only 5×10^{-5}.

For $d = d_2$ the difference between the two pairs of eigenvalues is still very small and the anti-phase mode cross the hopf bifurcation just before the in-phase one. Finally for $d = d_1$ the degeneration is completely broken, but the anti-phase mode crosses the hopf much before than the in-phase one, as shown in Fig. 8.4.

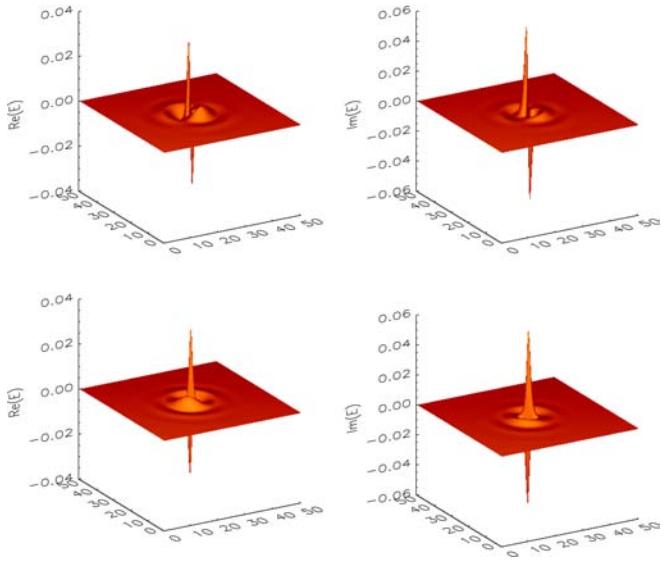

Figure 8.1: Spatial profile of the real (left) and imaginary (right) part of the Goldstone modes for a single localized structure. This two modes are associated to translations in two orthogonal directions (each direction corresponding to one mode). $I_s = 0.9$.

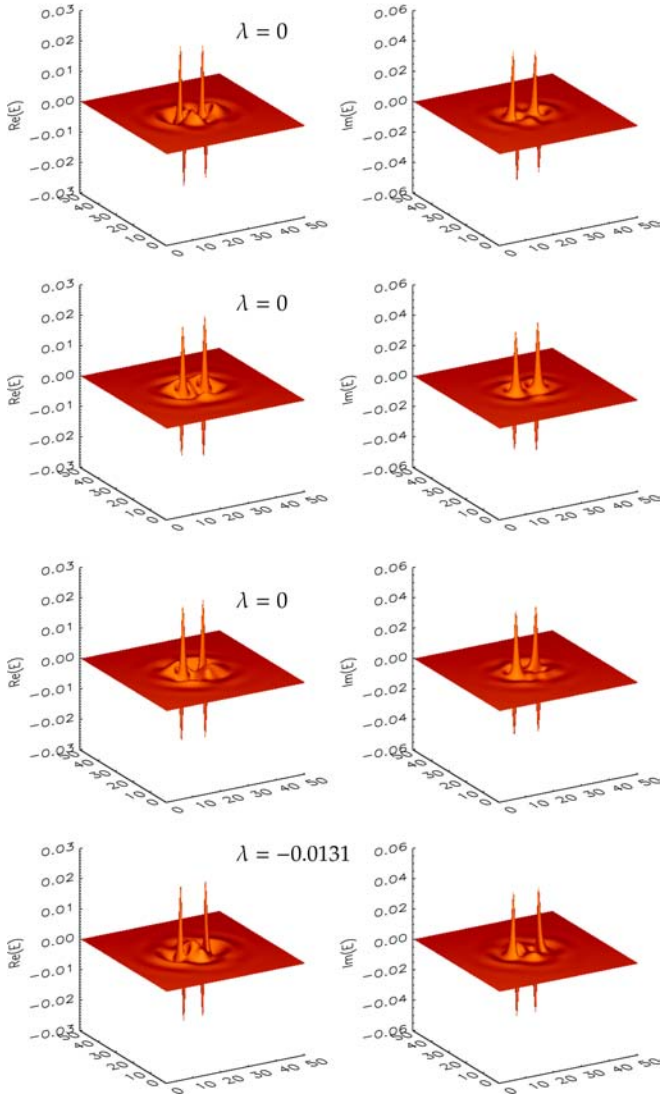

Figure 8.2: Spatial profile of the real (left) and imaginary (right) part of the three Goldstone modes and the less damped mode ($\lambda = -0.0131$) for two structures ($d = 7.816$). $I_s = 0.9$. From top to bottom, the first two modes induce translations in two orthogonal directions (determined in this case by the symmetry axis of the two structure complex). The third mode induce rotations of the two structure complex around its center.

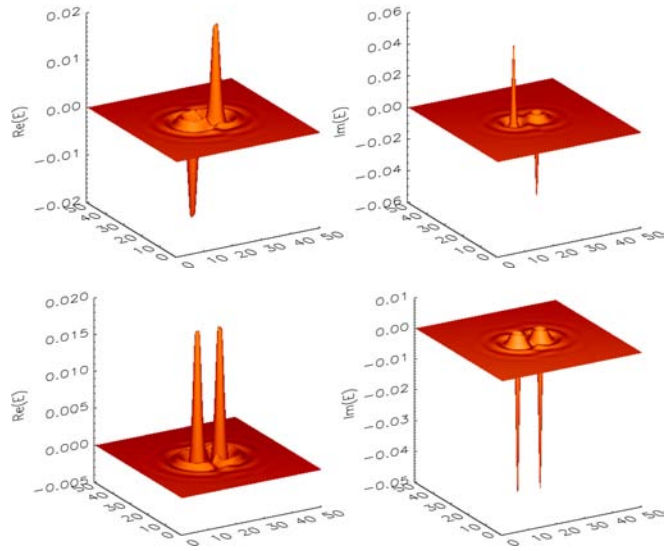

Figure 8.3: Anti-phase (top) and in-phase (bottom) modes for $I_s = 0.86$ and $d = d_1 = 7.816$.

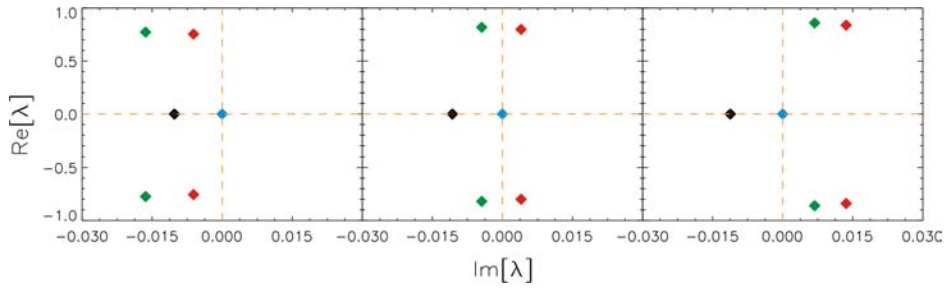

Figure 8.4: Hopf bifurcation for two coupled LS at $d = d_1$. From left to right, Is=0.81,0.82,0.83. Red and green dots are the eigenvalues corresponding to the anti-phase and in-phase modes respectively. The blue dots are the three zero eigenvalues of the Goldstone modes, and the black dot is the eigenvalue of the damped mode.

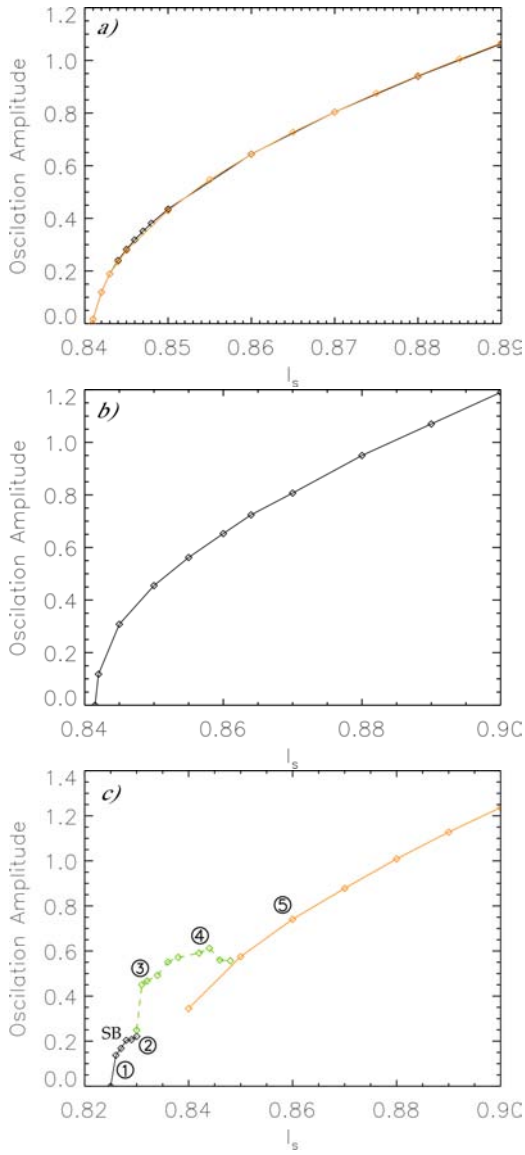

Figure 8.5: Amplitude of the in-phase (orange), anti-phase (black) and mixed (green) oscillations as a function of I_s for the first three equilibrium distances. From top to bottom: $d_3 = 19.93$, $d_2 = 15.82$ and $d_1 = 7.816$. Throughout this chapter we take $\theta = 1.27$.

Fig. 8.5 shows the bifurcation diagram of the in-phase and anti-phase cycles for the first three equilibrium distances $d_1 = 7.816$, $d_2 = 15.82$ and $d_3 = 19.93$. The amplitude of the oscillations close to the Hopf bifurcation grows as the square root of the distance to the threshold as expected (Fig. 8.5). For $d = d_3$ the amplitude of the in-phase and anti-phase are almost equal. We observe that the anti-phase cycle appears first and is stable for all the range of plotted parameters. For this distance the in-phase cycle is created just after the anti-phase cycle (within a 10^{-5} parameter difference) and is also always stable. Therefore, for this distance, we observe then coexistence of in-phase and anti-phase oscillations, and one reaches one or the other cycle depending on the initial condition *.

For d_2 the anti-phase cycle is also created first, and remains stable from there on. The in-phase cycle, appears later and it is unstable for all the range of parameters considered. Therefore, in this case, initial conditions at arbitrary phases will evolve to anti-phase oscillations (Fig. 8.5 b).

For d_1 the situation is more complicated: first the stable anti-phase limit cycle is created at $I_s \simeq 0.825$. Initially, both structures have the same oscillation amplitude. At $I_s \simeq 0.828$ (SB in Fig. 8.5) there is a symmetry breaking bifurcation and the oscillation amplitude of the two structures becomes different, i.e. the two structures oscillate around the same mean value in anti-phase and with different amplitudes. The difference in the oscillation amplitude between the two structures grows gradually with I_s. An interesting effect which is due to the fact that the LS are non punctual oscillators, and therefore have a spatial structure, is that in this region the structures complex moves due to the asymmetry. The centers of the two structures drift along the x axis in the direction of the structure with larger oscillation amplitude. For larger I_s the unstable in-phase limit cycle is created and it becomes stable at $I_s = 0.84$. An interesting phenomenon appearing in this case is a third branch connecting the in-phase and anti-phase cycles corresponding to a mixed mode. Since the two cycles have a slightly different frequency, this mode presents a beating at the frequency difference of the in-phase and anti-phase modes.

This situation is illustrated in detail in Fig. 8.6. Each of the panels in the figure corresponds to one of the tags in Fig. 8.5 (c), showing a time trace in each dynamical regime. Fig. 8.6 ① shows anti-phase oscillations. Increasing I_s, the amplitude increases differently for each LS, and therefore we reach a regime where the anti-phase oscillations are asymmetric (Fig. 8.6 ②). Further increasing I_s this anti-phase cycle is unstable and the amplitude of oscillations becomes modulated by a slow frequency. Close to the anti-phase cycle the fast

*Strictly speaking, there has to be a very narrow parameter region where the anti-phase cycle is stable while the in-phase is not, but this region is so narrow that is not observed in practise when numerically integrating the equations.

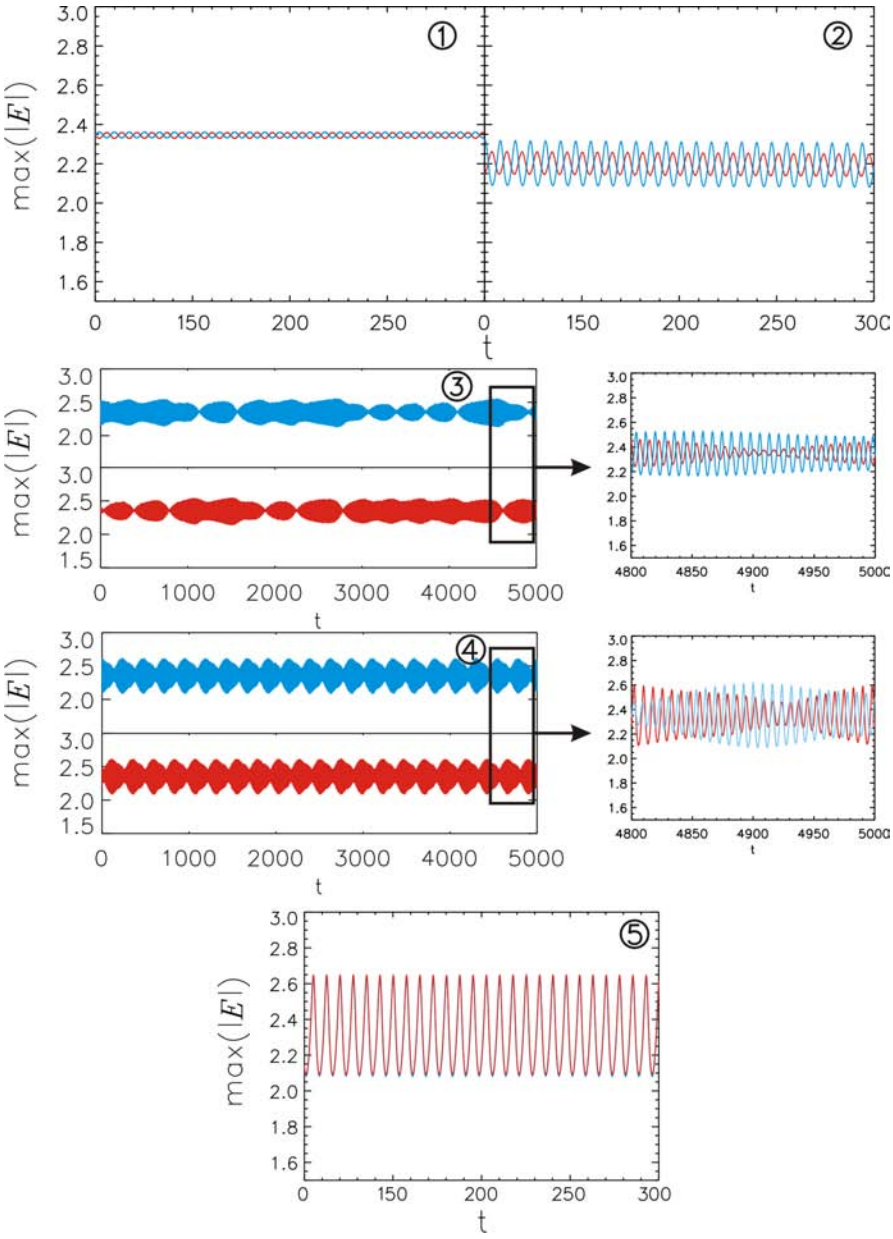

Figure 8.6: Time traces of the maximum of the two LS for different values of I_s. Each panel corresponds to one of the tags of Fig. 8.5.

oscillations of this modulated cycle are almost in anti-phase (Fig. 8.6 ③). Near the end of this branch the fast oscillations are almost in phase (Fig. 8.6 ④). Finally, the amplitude of the modulations decreases until we reach a regime of in-phase oscillations (Fig. 8.6 ⑤).

8.3 Conclusions

In this chapter we have studied the interaction of oscillating localized structures. First we have studied how, for stationary localized structures, the interaction breaks the degeneracy of the two pairs of Goldstone modes of the independent LS. When considering oscillating localized structures the same mechanism appears also for the unstable Hopf modes, creating two limit cycles with slightly different frequencies, and that occur for different values of the parameter.

These two limit cycles correspond to in-phase and anti-phase oscillations. For the first three equilibrium distances the anti-phase cycle is created first. For d_3 the anti-phase cycle is stable for all the range of the parameter and the in-phase cycle is unstable when created, but it becomes rapidly stable and remains so. For d_2 the anti-phase cycle is also stable for the whole parameter range, and the in-phase limit cycle is created unstable, and remains unstable.

Finally, for d_1 the anti-phase cycle is created stable, later it becomes unstable and the oscillations become asymmetric, leading to the drift of the localized structures. Then a mixed mode appears, connecting the anti-phase branch with the in-phase branch. The oscillations of this mixed mode are a beating between the frequencies of the in-phase and anti-phase modes. The existence of the mixed mode and the drift of the localized structures when the oscillations are asymmetric is a nontrivial behavior that is a consequence of the spatial extension of the oscillators.

Chapter 9

Concluding Remarks

In this work we have explored the dynamics of nonlinear optical cavities and their possible applications to image and information processing.

In Part I we have shown how the Type II second harmonic generation can be used for all-optical image processing. In particular, in Chapter 2, we have shown that the system allows us to transfer an image in frequency from the fundamental to the second harmonic, to enhance the contrast and detect the contour of an image and also to filter the noise. All this procedures where first found for a cavity with planar mirrors, and then, we have shown that they are also possible for cavities with spherical mirrors, in a quasi-confocal configuration. This was done with the aim to show that this effects are realizable in a system which is easier to achieve experimentally than the plane mirror cavity. We hope that these results could encourage the realization of experiments in the subject.

Based on the idea of using the bistability and the diffraction of the second harmonic generation to filter noise and enhance the contrast of an image we developed, in Chapter 3, a technique to filter time series and detect change points in its mean value. We used the Ginzburg-Landau equation, which is a prototypic amplitude equation, as the filter. This equation presents the two required ingredients for the filter, spatial interaction (diffusion) and bistability, and it is also very well understood. We were able to filter both synthetic and real ecological data series and detect change points that were otherwise masked by noise. We also developed an heuristic method to determine the most likely change point and to test its validity. However, in spite of showing good results in the studied cases, this method lacks a rigorous mathematical background to test the validity of the detected changes, and this constitutes a disadvantage against well established methods as the t-test. Even though, the method is fast, easy to use

and implement, and does not require any assumption over the data. Therefore we consider that it can result in a very useful tool when combined with other methods.

Then, in Chapter 4, we applied this filtering method to the decoding of chaos encrypted messages. In this case we used the filter to detect the changes in a time series in which a binary message is masked so that the mean value of the transmitted signal for bits ″1″ and ″0″ is different. By detecting such changes we were able to reconstruct the original message. We propose an alternative encoding method that is able to avoid these attacks.

In Part II we studied the dynamics of Localized Structures (LS) in a Kerr cavity. In Chapter 5 we started by studding the dynamics of the localized structures when the system is pumped homogeneously. There we studied the bifurcations of the system and the dynamical regimes that arise from those bifurcations. In particular, we focused in the saddle-loop bifurcation and the excitable regime that arises from it. This excitable regime is a property of the localized structures and not of the system itself, given that its local dynamics does not show excitability. We were also able to recover a qualitative 2-dimensional sketch of the saddle-loop bifurcation by projecting the solution into its two only localized modes.

Then, in Chapter 6, we studied the effect of adding a localized Gaussian beam to the pump of the system. This allowed us to control the position of the localized structures, and it had an interesting impact on its dynamics. The introduction of the localized pump creates new bifurcations in the system and changes the way in which these bifurcations are organized. The main effect is the appearance of a saddle node on invariant circle bifurcation, which creates a new route to excitability. In this new route the threshold of excitability is controlled by the intensity of the Gaussian beam, and therefore it is easy to tune.

This ability to control the position of the LS and its excitability threshold was then used in Chapter 7 to create logic gates by coupling several localized structures. We shown how an AND and an OR gates can be used by placing three LS close together and properly tuning the distance between them and their thresholds. We have also shown how a NOT gate can be implemented using an oscillatory LS. These results are a proof of concept of the possibility of all-optical computing by means of the dynamical properties of localized structures. The Kerr cavity model, although interesting to understand basic mechanism of nonlinear optics is rather unrealistic, and therefore it would be interesting to search for this kind of excitable structures in more realistic models such as those for semiconductor lasers or VCSEL's. This would allow for this results to be explored experimentally.

Finally, in Chapter 8, we studied the interaction of oscillatory localized structures. This constitutes an example of interacting nonlocal oscillators and display some interesting nontrivial behavior. Similarly to what happens with stationary LS, when two oscillatory localized structures are placed close to each other they move until they get locked by tail interaction. Three equilibrium distances are found. We showed how the interaction breaks the degeneracy in the spectrum of the interacting LS and how in-phase and anti-phase oscillations appear. For weak interaction in-phase and anti-phase oscillation coexist. For intermediate interaction only anti-phase solutions are stable. For strong interaction there is a region of asymmetric amplitude anti-phase oscillations in which the LS drifts due to this asymmetry. Also for strong interaction there is a mixed oscillation mode created by a beating between the in-phase and anti-phase oscillations.

In short, in this work we explored some possible applications of nonlinear optics to image and information processing and we have also done an in depth study of the dynamics of Localized Structures in a Kerr cavity. We hope that our results trigger the realization of new experiments and new research in the areas.

Part III

Appendices

Appendix A

Numerical Integration of Partial Differential Equations

In this Appendix we describe with detail the numerical method used to integrate the Partial Differential Equations that appear through all this text.

All the equations that we studied in this thesis are of the form

$$\partial_t A(\vec{x},t) = aA(\vec{x},t) + b\nabla^2 A(\vec{x},t) + F(A(\vec{x},t)) \tag{A.1}$$

where $\vec{x} = (x, y)$ and $F(A(\vec{x},t))$ is a nonlinear function of the field A. For example, in the case of the Kerr cavity equations that we derived in Chapter 1 $F = |A|A + E_i$.

The time evolution of A subjected to periodic boundary conditions is obtained by numerically solving Eq. (A.1) in Fourier space. This method is pseudospectral and second order accurate in time.

We start by computing the Fourier transform of Eq. (A.1). Therefore each Fourier mode $\tilde{A}(\vec{q},t)$ evolves according to

$$\partial_t \tilde{A}(\vec{q},t) = -\alpha_{\vec{q}}\tilde{A}(\vec{q},t) + \tilde{F}(\tilde{A}(\vec{q},t)) \tag{A.2}$$

where $\alpha_{\vec{q}} = -(a + b\vec{q}^2)$. At any time, the amplitude $\tilde{F}(\tilde{A}(\vec{q},t))$ is calculated by taking the inverse Fourier transform of $\tilde{A}(\vec{q},t)$, computing the nonlinear term in real space and then calculating the Fourier transform of this term. A standard FFT subroutine is used for this purpose.

APPENDIX A. NUMERICAL INTEGRATION OF PARTIAL DIFFERENTIAL EQUATIONS

Eq. (A.2) is integrated numerically in time with a two-step method. For convenience we define the time step in such a way that the time is increased by $2\delta t$ at each iteration.

Since the system is solved numerically A needs to be discretized and, to achieve a sufficient spatial resolution, the spatial step size needs to be small enough. This means that the range of values of $|\vec{q}|$ is large, and therefore the linear time scales $\alpha_{\vec{q}}$ can take a wide range of values. A way to circumvent this stiffness problem is to treat exactly the linear terms by using the formal solution:

$$\partial_t \tilde{A}(t) = e^{-\alpha_{\vec{q}} t}\left(\tilde{A}(t_0)e^{\alpha_{\vec{q}} t_0} + \int_{t_0}^{t} \tilde{F}(\tilde{A}(s))e^{\alpha_{\vec{q}} s} ds\right) \tag{A.3}$$

where we avoided writing explicitly the dependence on $\vec{q}$ of the fields for simplicity.

From Eq. (A.3) we find the following relation:

$$\frac{\tilde{A}(t+\delta t)}{e^{-\alpha_{\vec{q}}\delta t}} - \frac{\tilde{A}(t-\delta t)}{e^{\alpha_{\vec{q}}\delta t}} = e^{-\alpha_{\vec{q}} t}\int_{t-\delta t}^{t+\delta t} \tilde{F}(\tilde{A}(s))e^{\alpha_{\vec{q}} s} ds \tag{A.4}$$

A Taylor expansion of $\tilde{F}(\tilde{A}(s))$ around $s = t$ for small δt gives an expression for the right hand side of Eq. (A.4)

$$\tilde{F}(\tilde{A}(s)) = \frac{e^{\alpha_{\vec{q}}\delta t} - e^{-\alpha_{\vec{q}}\delta t}}{\alpha_{\vec{q}}} + O(\delta t^3) \tag{A.5}$$

Substituting this result into Eq. (A.4) we get:

$$\tilde{A}(n+1) = e^{-2\alpha_{\vec{q}}\delta t}\tilde{A}(n-1) + \frac{1 - e^{-2\alpha_{\vec{q}}\delta t}}{\alpha_{\vec{q}}}\tilde{F}(\tilde{A}(n)) + O(\delta t^3) \tag{A.6}$$

where, for simplicity we used n as a shortcut of $n\delta t$. This expression is called the *salved leap frog* [206]. For this scheme to be stable we need to apply a corrective algorithm to Eq. (A.6). Following steps analogous to those already taken we obtain the following expression:

$$\tilde{A}(n) = e^{\alpha_{\vec{q}}\delta t}\tilde{A}(n-1) + \frac{1 - e^{\alpha_{\vec{q}}\delta t}}{\alpha_{\vec{q}}}\tilde{F}(\tilde{A}(n-1)) + O(\delta t^2) \tag{A.7}$$

Then, we use the following method, called the *two step method*, to compute the evolution of the field

1. We compute $\tilde{F}(\tilde{A}(n-1))$ by going to real space.
2. Then, Eq. (A.7) is used to obtain an approximation to $\tilde{A}(n)$
3. From this approximation, the nonlinear term $\tilde{F}(\tilde{A}(n))$ is now calculated, by going back to the real space.
4. Finally, $\tilde{A}(n+1)$ is computed using Eq. (A.6).

At each iteration $\tilde{A}(n+1)$ is obtained from $\tilde{A}(n-1)$ and the time advances by $2\delta t$. The total error is $O(\delta t^3)$ despite the fact that the intermediate step is accurate to $O(\delta t^2)$. Trough all this thesis a square lattice of size 512×512 points was used. The space discretization was taken $dx = 0.1875$ while the time step was $dt = 10^{-3}$.

Appendix B

Linear Stability Analysis of Radially Symmetric Solutions

In Chapters 5 and 6 we studied the stability of the stationary Localized Structures solutions of Eq. (1.87). Those solutions are radially symmetric, and we describe here the method used to obtain them and compute its stability.

We start by setting $E = E_s\,(1+A)$, where E_s is the value of the homogeneous steady state solution (see Chapter 5) so that $A(x, y)$ describes the solution without the homogeneous background,

$$\partial_t A = -(1 + i\theta)A + i\nabla^2 A + iI_s\left(2A + A^\star + A^2 + 2|A|^2 + |A|^2\,A\right) \tag{B.1}$$

where Eq. (B.1) is obtained directly from Eq. (1.87), without any approximation. To obtain the stationary solutions one may numerically solve the rhs of Eq. (B.1) equated to zero. However, since we have 2 spatial dimensions and the self-focusing dynamics involve very large wavenumbers with very fast dynamics, this is a difficult and time consuming task (a method to obtain the solutions in two dimensions will be shown in Appendix C. Instead, we can take advantage of the fact that the LS structures are rotationally symmetric with respect to their center, so that they can be described in terms of the 1D radial equation for $A(r)$

$$\partial_t A = -(1 + i\theta)A + i\left(\partial_r^2 + \frac{1}{r}\partial_r\right)A + iI_s\left(2A + A^\star + A^2 + 2|A|^2 + |A|^2\,A\right) \tag{B.2}$$

The boundary conditions for this problem are such that the derivatives are zero at the boundaries, i.e., $\partial_r A(r = 0) = \partial_r A(r = L) = 0$, where the system size L is large

enough to ensure that the electric field approaches smoothly the homogeneous solution ($A(r) \to 0$) before reaching the boundary.

Steady state LS solutions for this system, both stable and unstable, are found by equating to zero the left hand side of Eq. (B.2). This is done using a Newton-Raphson method [207], we want to solve the equation

$$F(A(r)) = 0 \tag{B.3}$$

Where F is the left hand side of Eq.(B.2). Starting from an estimate $A_{old}(r)$, we find a new estimate for the solution

$$A_{new}(r) = A_{old} + A_{inc}(r) \tag{B.4}$$

where A_{inc} is given by

$$\begin{pmatrix} A_{inc} \\ A^*_{inc} \end{pmatrix} = -\mathbf{U^{-1}} \cdot \begin{pmatrix} F \\ F^* \end{pmatrix} \tag{B.5}$$

Here **U** is the Jacobian matrix, obtained by differentiating F and F^* with respect to A and A^* (since A is a complex field A and A^* are independent variables). Therefore **U** yields

$$\mathbf{U} = \begin{pmatrix} U_{11} & U_{12} \\ U_{21} & U_{22} \end{pmatrix} \tag{B.6}$$

where

$$\begin{aligned} U_{11} &= \frac{\delta F}{\delta A} = -(1 + i\theta) + i\left(\partial_r^2 + \frac{1}{r}\partial_r - \frac{m^2}{r^2}\right) + i2I_s\left(1 + A + A^* + |A|^2\right) \\ U_{12} &= \frac{\delta F^*}{\delta A} = iI_s\left(1 + 2A + A^2\right) \\ U_{21} &= \frac{\delta F}{\delta A^*} = U_{12}^* \\ U_{22} &= \frac{\delta F^*}{\delta A^*} = U_{11}^* \end{aligned} \tag{B.7}$$

To solve this system numerically we start by discretizing $A(r)$. The derivatives in the Jacobian and $F(A(r))$ are computed in the Fourier space in an analogous

way to Appendix A. Then, Eq. (B.5) becomes a linear system of equations that is solved by standard techniques. The obtained estimate for $A(r)$ is used to repeat the process again, until the desired accuracy is achieved, i.e. until $F(A_{new}(r))$ is equal to zero within the desired error.

This method is very sensitive to the initial condition that is used, and in many parameter values more than one solution exists. Numerical continuation of a particular solution can be achieved, except at bifurcation points, by using the solution corresponding to a set of parameter values as the initial condition for a nearby point when one of the parameters is slightly perturbed. A comment to this procedure is that this approach, although numerical in nature,is virtually exact, as a numerical approximation as accurate as desired to the stationary LS can be obtained.

Now that we have numerically computed the stationary solution $A_{LS}(r)$, its stability against radial and azimuthal perturbations can be obtained by linearizing Eq. (B.1) around this point [208]. This yields a linearized equation for the time evolution of the perturbations $\delta A(r,\phi,t) = A(r,\phi,t) - A_{LS}(r)$. The solutions of the linear problem can be written as

$$\delta A = [R_+(r)\, e^{im\phi} + R_-(r)\, e^{-im\phi}] \exp(\lambda\, t) \tag{B.8}$$

where m is the wavenumber of the azimuthal perturbation. This yields the eigenvalue problem

$$\mathbf{U}\Psi = \lambda\Psi \tag{B.9}$$

where $\Psi = (R_+, R_-^\star)^\top$ and $\mathbf{U}$ is evaluated at A_{LS}. For purely radial perturbations ($m = 0$) $R_- = R_+$. The matrix $\mathbf{U}$ is time-independent as it is evaluated at the stationary LS (stable or unstable) under study.

The problem reduces to finding the eigenvalues, λ, and eigenvectors, Ψ, where it is important to mention that $\mathbf{U}$ is a complex matrix and, thus, the eigenvectors are complex quantities in general. Due to the symmetry of $\mathbf{U}$ the eigenvalues are either real or pairs of complex conjugates. This last property stems from the fact that, considering the real and imaginary parts of A, $\mathbf{U}$ can be rewritten as a real matrix (see Appendix C for details). We note also that, due to the discretization of the space, $\mathbf{\Psi}$ becomes a vector whose dimension is $2N$. The set of eigenvectors Ψ_i ($i = 1, 2N$) form a basis, and their amplitudes define a natural phase space where studying the dynamics of LS.

However, $\mathbf{U}$ is not a self-adjoint operator so, the set of eigenmodes does not form an orthogonal basis. To find the components of a field profile on a mode Ψ_i one has to project it onto the corresponding eigenmode Φ_i of the adjoint Jacobian matrix $\mathbf{U}^\dagger$. In Section 5.3 we where interested in the deviation of the field profile from the unstable LS (saddle point) $\delta\mathbf{A} = (\delta A, \delta A^\star)^\top$. In particular

we calculate the components of this deviation on the unstable and the most stable eigenmodes of the Jacobian matrix of the unstable LS. These amplitudes are given by $\beta_i = \int \mathbf{\Phi}_i^{\top\star} \cdot \delta\mathbf{A} dr$ $(i = 1, 2)$, where Φ_1 is the unstable and Φ_2 the most stable eigenmodes of the adjoint Jacobian matrix.

We should note that in the work reported here the LS are always inside the region in which they are stable versus azimuthal perturbations [99], so all the instabilities described in the text are obtained for $m = 0$. As a final comment, the stability problem of stationary LS, that in principle live in an infinite-dimensional phase space, is reduced numerically to a stability problem in a finite-dimensional, albeit large, phase space.

Appendix C

Linear Stability Analysis of Two Dimensional Solutions

In Appendix B we have shown how to compute the radially symmetric stationary solutions of (B.1). In the study interacting localized structures (Chapters 7 and 8) the solutions are no longer radially symmetric and therefore can not be computed from the radial equation (B.2). Instead we have to use the two dimensional equation (B.1), for the field without the homogeneous background.

Steady state LS solutions for this system are found by equating to zero the lhs of Eq. (B.1). This and the computation of the stability of the solutions is done in an analogous way to Appendix B. The main difference between this case and the radially symmetric one is the shape of the Jacobian and how it is computed numerically.

In Appendix B, we considered A and A^* as the independent variables. In this case, is more convenient to take the real and imaginary parts of A as the independent variables. Therefore in this case, Eq. (B.5) becomes

$$\begin{pmatrix} \mathrm{Re}\,(A_{inc}) \\ \mathrm{Im}\,(A_{inc}) \end{pmatrix} = -\mathbf{U^{-1}} \cdot \begin{pmatrix} \mathrm{Re}\,(F) \\ \mathrm{Im}\,(F) \end{pmatrix} \tag{C.1}$$

where the Jacobian is computed from Eq.(B.1) and yields

$$\mathbf{U} = \begin{pmatrix} U_{11} & U_{12} \\ U_{21} & U_{22} \end{pmatrix} \tag{C.2}$$

with

$$
\begin{aligned}
U_{11} &= \frac{\delta \mathrm{Re}\,(F)}{\delta \mathrm{Re}\,(A)} = -1 - 2\mathrm{Im}\,(A)I_s - 2\mathrm{Re}\,(A)\mathrm{Im}\,(A)I_s \\
U_{12} &= \frac{\delta \mathrm{Re}\,(F)}{\delta \mathrm{Im}\,(A)} = -I_s - 2\mathrm{Re}\,(A)I_s - \mathrm{Re}\,(A)^2 I_s - 2\mathrm{Im}\,(A)^3 I_s + \theta - \nabla^2 \\
U_{21} &= \frac{\delta \mathrm{Im}\,(F)}{\delta \mathrm{Re}\,(A)} = -1 + 2\mathrm{Im}\,(A)I_s + 2\mathrm{Re}\,(A)\mathrm{Im}\,(A)I_s \\
U_{22} &= \frac{\delta \mathrm{Im}\,(F)}{\delta \mathrm{Im}\,(A)} = 3I_s + 6\mathrm{Re}\,(A)I_s + 3\mathrm{Re}\,(A)^2 I_s + \mathrm{Im}\,(A)^2 I_s - \theta + \nabla^2
\end{aligned}
$$

The next step is to discretize A to solve Eq. (C.1) numerically. For the radial case, $A(r)$ becomes a vector of N components, since it is one dimmensional. Therefore, the Jacobian is a $N \times N$ matrix (in the case considered, of complex numbers). As in Appendix B we computed the derivatives in Fourier space, a large number of nondiagonal components of the Jacobian will be, in general, nonzero [*]. In the two dimensional case, when $A(x, y)$ is discretized it becomes a vector of N^2 complex numbers (that come from a matrix of $N \times N$), that become a matrix of $2N^2$ real numbers when we consider $\mathrm{Re}\,(A)$ and $\mathrm{Im}\,(A)$ as our independent variables. Hence, the Jacobian will be in this case a matrix of $4N^4$ elements. If we compute the derivatives using the same method as before (i.e. using the Fourier transform), there will be also a lot of this $4N^4$ elements that will be, in general, nonzero (in fact, there will be $2(N^4 + N^2)$ nonzero elements). Therefore, the number of nonzero elements become rapidly larger than what can be dealt with using reasonable amount of memory in a reasonable time. For example, for $N = 256$ more than 32Gb of memory are needed to allocate the Jacobian matrix.

A way to circumvent this problem is to change the way in which the derivatives are computed. By using a finite difference scheme to compute them, the Jacobian matrix becomes sparse with $O(N^2)$ nonzero elements instead of the $O(N^4)$ of the Fourier method. In what follows of this Appendix we will show how to construct this sparse Jacobian.

First we want to compute the finite difference representation of the transverse Laplacian term in $\mathbf{U}$. To do so, we start by computing the representation of the second derivative for a one dimensional field

[*]This is because computing derivative of $A(x_i, y_j)$ in Fourier space involves the values of $A(x_l, y_m)$ for all l and m. Another way to say this is that the derivative operator constructed from the Fourier transform is dense [209].

$$\partial_x^2 A(x) \to \mathbf{D_2} \cdot A = \frac{1}{h^2} \begin{pmatrix} -1 & 1 & 0 & 0 & & & \dots & 0 \\ 0 & 1 & -2 & 1 & 0 & & \dots & 0 \\ 0 & 0 & 1 & -2 & 1 & 0 & \dots & 0 \\ 0 & 0 & \ddots & \ddots & \ddots & & & 0 \\ 0 & & & & 1 & -2 & 1 & 0 \\ 0 & & \dots & & & 0 & 1 & -1 \end{pmatrix} \cdot \begin{pmatrix} A_1 \\ A_2 \\ A_3 \\ \\ \vdots \\ A_N \end{pmatrix} \tag{C.3}$$

where A_i is a shortcut for $A(x_i)$ and h is the discretization step.

If now consider the field in two dimensions, then $A(x, y)$ becomes the matrix $A(x_i, y_j)$, that can be rewritten as a vector A_k. The two dimensional version of the second derivative can be written as [209]

$$\partial_x^2 A(x, y) \to (\mathbf{D_2} \otimes \mathbf{I}) \cdot A \tag{C.4}$$

where $\otimes$ denotes the Kronecker product ($C_{pq} = A_{ij} B_{kl}$ with $p = i * N + k$ and $q = j * N + l$) and I is the $N \times N$ identity matrix. Therefore, the numerical representation of the transverse Laplacian is

$$\nabla^2 A(x, y) \to (\mathbf{D_2} \otimes \mathbf{I} + \mathbf{I} \otimes \mathbf{D_2}) \cdot A = \mathbf{L} \cdot A \tag{C.5}$$

Now that we have computed the numerical representation of the Laplacian, we can compute the numerical representation of the Jacobian matrix $\mathbf{U}$. This matrix is composed by four blocks U_{ij}, the blocks U_{11} and U_{22} which are diagonal and the blocks U_{21} and U_{12} which have a diagonal part plus the nondiagonal terms of the Laplacian.

As we stated previously the purpose of using finite differences was to obtain a sparse representation of the Laplacian and therefore a sparse Jacobian, and the most efficient way of writing a sparse matrix is to write only the nonzero elements. This is done by representing the matrix as three vectors, containing the row, the column and the value of the nonzero elements respectively.

The easiest way to write the Jacobian in this notation is to first write the diagonal elements of the four blocks (i.e all the elements except those corresponding to the Laplacian). Then we write the matrix $\mathbf{L}$ starting from the sparse representation of $\mathbf{D_2}$ and computing the Kronecker products with the identity matrix. Finally,

we add the matrix **L** to the blocks U_{12} and U_{21} by properly shifting the columns or rows of **L**.

Once we compute the sparse Jacobian matrix, Eq. (C.1) can be solved using one of the many available libraries to solve sparse linear systems. Then, the eigenvectors and eigenvalues of the sparse Jacobian are computed using the SLEPC and PETSC libraries [210–212], to analyze the stability of the solutions.

List of Figures

References

[1] http://www.corel.com.

[2] J. Teuber, *Digital Image Processing*, Prentice Hall, 1993.

[3] http://www.adobe.com/es/products/photoshop/photoshop/.

[4] http://www.vips.ecs.soton.ac.uk.

[5] http://www.gimp.org/.

[6] http://www.imagemagick.org.

[7] http://www.tjut.edu.cn/CISP2008.

[8] http://www.icip2007.org/.

[9] http://eccv2008.inrialpes.fr/.

[10] http://www.icpr2008.org/.

[11] http://www.cvpr.org/.

[12] http://www.sintef.no/upload/IKT/9011/geometri/lsseg/doc/html/page_HowSmoothingWorks.h

[13] L. Moisan, F. Guichard, and J. Morel *Journal de Physique IV* **2002**, pp. 137–154, 2002.

[14] P. Perona and J. Malik *IEEE Trans. Patt. Anal. Mach. Intell.* **12**, pp. 629–639, 1990.

[15] G. Cottet and M. E. Ayyadi *IEE Trans. Imag. Proc.* **20**, p. 100, 1998.

[16] F. Catté, P. Lions, J. Morel, and T. Coll *SIAM Journal on Numerical Analysis* **29**(1), pp. 182–193, 1992.

[17] L. Alvarez, P. Lions, and J. Morel *SIAM Journal on Numerical Analysis* **29**(3), pp. 845–866, 1992.

[18] B. S. Wherrett, *Optical Computing*, CRC Press, 1989.

[19] A. V. Lugt *Optical Engineering* **23-6**, p. 688, 1984.

[20] L. J. Cutrona, E. N. Leith, C. J. Palermo, and L. J. Porcello *IRE Trans. Inform. Theory* **6**, pp. 386–400, 1960.

[21] H. J. Caulfield, J. Kinser, and S. K. Rogers *Proceedings of the IEEE* **77**, pp. 1573–1583, 1989.

[22] H. M. Gibbs, *Optical Bistability: Controlling Light with Light*, Academic Press, 1985.

[23] P. Günther and J. P. Huignard, eds., *Photorefractive Materials and Their Applications II*, vol. Topics in Applied Physics Vol.62, Springer-Verlag, 1989.

[24] J. Feinberg *Opt. Lett.* **5**, p. 330, 1980.

[25] J. P. Huignard and J. P. Herriau *Appl. Opt.* **17**, p. 2671, 1978.

[26] B. Liang, Z. Wang, J. Guang, G. Mu, and C. M. Cartwright *Opt. Lett.* **25**, p. 1086, 2000.

[27] E. Ochoa, L. Hesselink, and W. Goodman *Appl. Opt.* **24**, p. 1826, 1985.

[28] Y. H. Ja *Opt. Comm.* **44**, p. 24, 1982.

[29] Y. H. Ja *Opt. Quant. Electron.* **15**, p. 457, 1983.

[30] Y. H. Ja *Appl. Phys. B* **36**, p. 21, 1985.

[31] H. Rajbenbach, A. Delboubl, and J. P. Huignard *Opt. Lett.* **28**, p. 1275, 1989.

[32] M. D. Rahn, D. P. West, and J. D. Shakos *J. Appl. Phys.* **87**, p. 127, 2000.

[33] J. D. Scargle *Astrophys. Journ.* **263**(2), p. 835, 1982.

[34] N. Beck, J. N. Katz, and R. Tucker *Amer. Journ.Pol. Sci.* **42**(4), p. 1260, 1998.

[35] J. D. Hamilton *Econometrica* **57**(2), p. 357, 1989.

[36] C. A. Pope, D. W. Dockery, J. Spengler, and et al. *Amer. Rev. Resp. Disease* **144**(3), p. 668, 1991.

[37] J. F. Ducré-Robitallie, L. A. Vincent, and G. Boulet *Int. J. Climat.* **23**(9), p. 1087, 2003.

[38] J. K. Petersen, J. W. Hansen, M. B. Laursen, P. Clausen, J. Cartensen, and D. J. Conley *Ecol. Appl.* **18**(2), p. 479, 2008.

[39] M. Scheffer, S. Carpenter, J. A. Foley, C. Folke, and B. Walker *Nature* **413**, p. 591, 2001.

[40] http://www.thresholds eu.org, "Thresholds integrated project under the european unionś fp6 contract no. 003933)."

[41] http://www.beringclimate.noaa.gov/regimes/Regime_shift_methods_list.htm.

[42] E. S. Epstein *J. Appl. Meteorol* **21**, p. 1172, 1982.

[43] S. Rodionov *Geophys. Res. Lett.* **31**, p. L09204, 2004.

[44] S. A. Mauget *J. Climate* **16**, p. 3905, 2003.

[45] T. R. Karl and C. W. W. Jr. *J. Clim. Appl. Meteorol.* **26**, p. 1744, 1987.

[46] C. Goossens and A. Berger, *How to recognize an abrupt climatic change? Abrupt Climatic Change: Evidence and Implications*, Kluwer Academic Publisher, Dordrecht, 1987.

[47] F. W. W. Gerstengarbe *Clim. Research.* **11**, p. 97, 1999.

[48] L. Perreault, J. Bernier, and E. Parent *J.Hydrol* **235**, p. 221, 2000.

[49] P. S. Chu and X. Zhao *J. Climate* **17**, p. 4893, 2004.

[50] J. B. Elsner, X. Niu, and T. Jagger *J. Climate* **4**, p. 2652, 2004.

[51] A. R. Solow *J. Clim. Appl. Meteorol.* **26**, p. 1401, 1987.

[52] D. R. Easterling and T. C. Peterson *Int. J. Climat.* **15**, p. 369, 1995.

[53] J. B. Elsner, T. Jagger, and X. Niu *Geophys. Res. Lett.* **27**, p. 1743, 2000.

[54] R. Lund and J. Reeves *J. Climate* **15**, p. 2547, 2002.

[55] T. A. Buishand *J. Hydrol.* **58**, p. 11, 1982.

[56] G. A. Rebstock *Global Change Biol.* **8**, p. 71, 2002.

[57] T. Andersen, J. Cartensen, E. Hernández-García, and J. M. Z. Comenges, "Performance testing of threshold identification methods." Thresholds Project Deliverable, 2007.

[58] S. Koga and Y. Kuramoto *Prog. Theor. Phys.* **392**, pp. 106–121, 1980.

[59] B. S. Kerner and V. V. Osipov, *Autosolitons: A new approach to problems of self-organization and Turbulence*, Kluwer, Dordrecht, 1994.

[60] V. K. Vanag and I. R. Epstein *Chaos* **17**, p. 037110, 2007.

[61] F. J. Niedernostheide, B. S. Kerner, and H. G. Purwins *Phys. Rev. B* **46**, pp. 7559–7570, 1992.

[62] P. B. Umbanhowar, F. Melo, and H. L. Swinney *Nature* **382**, p. 793, 1996.

[63] J. J. Niemela, G. Ahlers, and D. S. Cannell *Phys. Rev. Lett.* **64**, p. 1395, 1990.

[64] O. Batiste and E. Knobloch *Phys. Rev. Lett.* **95**, p. 244501, 2005.

[65] O. Lejeune, M. Tlidi, and P. Couteron *Phys. Rev. E* **66**, p. 010901(R), 2002.

[66] W. J. Firth and C. O. Weiss *Opt. Photon. News* **13**(2), p. 55, 2002.

[67] L. A. Lugiato *IEEE J. Quant. Elect.* **39**, pp. 193–19, 2003.

[68] N. N. Rosanov, *Spatial Hysteresis and Optical Patterns*, Springer series in synergetics, Springer, Berlin, 2002.

[69] S. Barland and et al. *Nature (London)* **419**, p. 699, 2002.

[70] Y. Tanguy, T. Ackemann, W. J. Firth, and R. Jager *Physical Review Letters* **100**(1), p. 013907, 2008.

[71] T. Ackemann and W. Lange *Appl. Phys. B* **72**(1), p. 21, 2001.

[72] N. Akhmediev and A. Ankiewicz, eds., *Dissipative Solitons*, vol. 661 of *Lecture Notes in Physics*, Springer, Berlin, 2005.

[73] M. Tlidi, M. Taki, and T. Kolokolnikov *Chaos* **17**, p. 037101, 2007.

[74] N. Akhmediev and A. Ankiewicz, eds., *Dissipative Solitons: From Optics to Biology and Medicine*, vol. 751 of *Lecture Notes in Physics*, Springer, Berlin, 2008.

[75] P. Coullet, C. Riera, and C. Tresser *Chaos* **14**, p. 193, 2004.

[76] F. Pedaci, S. Barland, E. Caboche, P. Genevet, M. Giudici, J. R. Tredicce, T. Ackemann, A. J. Scroggie, W. J. Firth, G.-L. Oppo, G. Tissoni, and R. Jäger *Applied Physics Letters* **92**(1), p. 011101, 2008.

[77] F. Pedaci, G. Tissoni, S. Barland, M. Giudici, and J. Tredicce *Applied Physics Letters* **93**(11), p. 111104, 2008.

[78] W. J. Firth and A. Lord *Journal of Modern Optics* **43**, p. 1071, 1996.

[79] S. Fauve and O. Thual *Phys. Rev. Lett.* **64**, pp. 282–284, 1990.

[80] M. Tlidi, P. Mandel, and R. Lefever *Phys. Rev. Lett.* **73**, pp. 640–643, Aug 1994.

[81] M. Tlidi, P. Mandel, and R. Lefever *Phys. Rev. Lett.* **73**, p. 640, 1994.

[82] M. Tlidi and P. Mandel *Phys. Rev. A* **59**, pp. R2575–R2578, Apr 1999.

[83] S. Longhi *Phys. Scr.* **56**(6), p. 611, 1997.

[84] K. Staliunas and V. J. Sánchez-Morcillo *Opt. Comm.* **139**(4), p. 306, 1997.

[85] S. Longhi *Opt. Comm.* **149**(4), p. 335, 1998.

[86] A. J. Scroggie, W. J. Firth, G. S. McDonald, M. Tlidi, R. Lefever, and L. A. Lugiato *Chaos, Solitons, and Fractals* **4**, p. 1323, 1994.

[87] K. A. Gorshkov, L. N. Korzinov, M. I. Rabinovich, and L. S. Tsimring *J. Stat. Phys.* **74**(5), p. 1033, 2005.

[88] L. S. Tsimring and I. S. Aranson *Phys. Rev. Lett.* **79**, pp. 213–216, Jul 1997.

[89] O. Thual and S. Fauve *J. Phys. (France)* **49**, p. 1829, 1988.

[90] L. Y. Glebsky and L. M. Lerman *Chaos: An Interdisciplinary Journal of Nonlinear Science* **5**(2), pp. 424–431, 1995.

[91] D. Gomila, *Dynamics of Spatial Structures in Nonlinear Optics*. PhD thesis, Universitat de les Illes Balears, March 2003.

[92] P. Coullet, C. Riera, and C. Tresser *Phys. Rev. Lett.* **84**, p. 3069, 2000.

[93] P. Coullet, C. Elphick, and D. Repaux *Phys. Rev. Lett.* **58**, pp. 431–434, Feb 1987.

[94] G. L. Oppo, A. J. Scroggie, and W. J. Firth *J. Opt. B: Quantum Semiclass. Opt.* **1**, pp. 133–138, 1999.

[95] G. L. Oppo, A. J. Scroggie, S. Scott, and M. Brambilla *J. Mod. Opt.* **47**(11), p. 2005, 2000.

[96] P. Coullet *Int. J. Bif. Chaos* **12**(11), p. 2445, 2002.

[97] D. Gomila, P. Colet, G.-L. Oppo, and M. San Miguel *Phys. Rev. Lett.* **87**, p. 194101, Oct 2001.

[98] W. J. Firth, A. Lord, and A. J. Scroggie *Phys. Scr.* **T67**, pp. 12–16, 1996.

[99] W. J. Firth, G. K. Harkness, A. Lord, J. M. McSloy, D. Gomila, and P. Colet *J. Opt. Soc. Am. B* **19**, pp. 747–752, 2002.

[100] V. K. Vanag and I. R. Epstein *Phys. Rev. Lett.* **92**, p. 128301, 2004.

[101] S. H. Strogatz, *Nonlinear Dynamics And Chaos*, Addison-Wesley, Reading, MA, 1994.

[102] P. Glendinning, *Stability, instability, and chaos*, Cambridge U. P., Cambridge, UK, 1994.

[103] J. Guckenheimer and P. Holmes, *Nonlinear Oscillations, Dynamical Systems, and Bifurcations of Vector Fields*, Springer, New York, 1983.

[104] S. Wiggins, *Global bifurcations and chaos: analytical methods*, Springer-Verlag, New York, UK, 1988.

[105] Y. A. Kuznetsov, *Elements of Applied Bifurcation Theory, 3rd ed.*, Springer-Verlag, Berlin, 2004.

[106] S. Schecter *SIAM J. Math. Anal.* **18**, pp. 1142–1156, 1987.

[107] E. M. Izhikevich *Int. J. Bifurcation Chaos Appl. Sci. Eng.* **10**, pp. 1171–1266, 2000.

[108] E. M. Izhikevich, *Dynamical Systems in Neuroscience*, MIT Press, Cambridge (MA), 2007.

[109] J. Rinzel and G. B. Ermentrout, "Analysis of neural excitability and oscillations," in *Methods in Neuronal Modeling*, C. Koch and I. Segev, eds., MIT Press, Cambridge, MA, 1989.

[110] E. M. Izhikevich *Int. J. Bif. Chaos* **10**, pp. 1171–1266, 2000.

[111] A. L. Hodgkin and A. F. Huxley *J Physiol* **117**(4), pp. 500–544, 1952.

[112] R. FitzHugh *Biophys. J.* **1**(6), pp. 445–466, 1961.

[113] C. M. Brooks, B. F. Hoffman, E. E. Suckling, and O. O. Orias, *Excitability of the Heart*, Grune & Stratton, New York, 1955.

[114] T. R. Chay and J. Keizer *Biophys. J.* **42**(2), pp. 181–190, 1983.

[115] V. K. Vanag, L. Yang, M. Dolnik, A. M. Zhabotinsky, and I. R. Epstein *Nature* **406**, p. 406, 2000.

[116] A. L. Hodgkin *J Physiol* **107**(2), pp. 165–181, 1948.

[117] E. Benoit *Astérisque* **2**(109-110), p. 159, 1983.

[118] C. Morris and H. Lecar *Biophys. J.* **35**(1), pp. 193–213, 1981.

[119] B. B. R. *Proc. Sbornik Referatov por Radiacioni Medicine* , p. 145, 1959.

[120] A. N. Zaikin and A. M. Zhabotinsky *Nature* **225**(5232), p. 535, 1970.

[121] W. Lu, D. Yu, and R. G. Harrison *Phys. Rev. A* **58**, p. R809, Aug 1998.

[122] S. Barland, O. Piro, M. Giudici, J. R. Tredicce, and S. Balle *Phys. Rev. E* **68**, p. 036209, Sep 2003.

[123] J. L. A. Dubbeldam, B. Krauskopf, and D. Lenstra *Phys. Rev. E* **60**, pp. 6580–6588, Dec 1999.

[124] M. Giudici, C. Green, G. Giacomelli, U. Nespolo, and J. R. Tredicce *Phys. Rev. E* **55**, pp. 6414–6418, 1997.

[125] A. M. Yacomotti, M. C. Eguia, J. Aliaga, O. E. Martinez, G. B. Mindlin, and A. Lipsich *Phys. Rev. Lett.* **83**, pp. 292–295, Jul 1999.

[126] P. Coullet, D. Daboussy, and J. R. Tredicce *Phys. Rev. E* **58**, pp. 5347–5350, Nov 1998.

[127] D. Goulding, S. P. Hegarty, O. Rasskazov, S. Melnik, M. Hartnett, G. Greene, J. G. McInerney, D. Rachinskii, and G. Huyet *Physical Review Letters* **98**(15), p. 153903, 2007.

[128] F. Plaza, M. G. Velarde, F. T. Arecchi, S. Boccaletti, M. Ciofini, and R. Meucci *Europhys. Lett.* **38**, pp. 85–90, 1997.

[129] P. A. Franken, A. E. Hill, C. W. Peters, and G. Weinreich *Phys. Rev. Lett.* **7**, pp. 118–119, 1961.

[130] R. W. Boyd, ed., *Nonlinear Optics*, 2003.

[131] E. Hetch, ed., *Optics*, 2002.

[132] C. C. Davis, ed., *Lasers and Electro-Optics, Fundamentals and Engieneering*, 1996.

[133] U. Peschel, C. Etrich, and F. Lederer *Opt. Lett* **23**, p. 500, 1998.

[134] U. Peschel, C. Etrich, and F. Lederer *Phys. Rev. E* **58**, p. 4005, 1998.

[135] S. Longhi *Opt. Lett* **23**, p. 346, 1998.

[136] S. Longhi *Phys. Rev. A* **59**, p. 346, 1999.

[137] L. A. Lugiato and R. Lefever *Phys. Rev. Lett.* **58**, pp. 2209–2211, 1987.

[138] A. J. Scroggie, *Spontaneous Optical Patterns in Two and Four Level Atomic Systems*. PhD thesis, University of Strathclyde, Glasgow, January 1995.

[139] M. Lax, W. H. Louisell, and W. B. McKnight *Phys. Rev. A* **11**(4), 1975.

[140] A. E. Siegman, *Laser*, University Science Books, Mill Valley, CA, 1st ed., 1986.

[141] M. Möller, L. M. Hoffer, G. L. Lippi, T. Ackemann, A. Gahl, and W. Lange *Journal of Modern Optics* **45**(9), pp. 1913–1926, 1998.

[142] Z. Y. Ou *Phys. Rev. A* **59**, p. 4021, 1999.

[143] P. Scotto, P. Colet, and M. S. Miguel *Opt. Lett.* **28**, pp. 1695–1679, 2003.

[144] J. Feinberg *Opt. Lett.* **5**, p. 330, 1980.

[145] J. P. Huignard and J. P. Herriau *Appl. Opt.* **17**, p. 2671, 1978.

[146] M. Marte, H. Ritsch, K. I. Petsas, A. Gatti, L. A. Lugiato, C. Fabre, and D. Leduc *Opt. Expr.* **3**, 1998.

[147] M. Bache, P-Lodahl, A. V. Mamaev, M. Marcus, and M. Saffman *Phys. Rev. A* **65**, p. 033811, 2002.

[148] http://www.ifisc.uib.es/thenhancer/.

[149] M. C. Cross and P. C. Hohenberg *Rev. Mod. Phys.* **65**, p. 851, Jul 1993.

[150] D. Walgraef, *Spatio-Temporal Pattern Formation, with examples in Physics, Chemistry and Materials Science*, Springer-Verlag, New York, 1996.

[151] S. R. Carpenter, J. F. Cole, J. F. Kitchell, and M. L. Pace *Limnol. Oceanogr.* **43**, p. 73, 1998.

[152] S. R. Carpenter, D. Ludwig, and W. A. Brock *Ecol. Appl.* **9**(3), p. 751, 1999.

[153] M. Basseville and I. V. Nikiforov, *Detection of Abrupt Changes: Theory and Application*, Prentice Hall, Englewood Cliffs, NJ, 1993.

[154] H. V. Storch and F. W. Zwiers, *Statistical analysis in climate research*, Cambridge University Press, 1999.

[155] W. W. S. Wei, *Time Series Analysis: Univariate and Multivariate Methods*, Addison-Wesley, Redwood City, CA, 1990.

[156] A. Argyris, D. Syvridis, L. Larger, V. Annovazzi-Lodi, P. Colet, I. Fischer, J. García-Ojalvo, C. R. Mirasso, L. Pesquera, and K. A. Shore *Nature* **438**, p. 343, 2005.

[157] A. Uchida, F. Rogister, J. García-Ojalvo, and R. Roy *Progress in Optics* **48**, pp. 203–341, 2005.

[158] C. Mirasso, P. Colet, and P. Garcia-Fernandez *Photonics Technology Letters, IEEE* **8**, pp. 299–301, Feb. 1996.

[159] G. D. VanWiggeren and R. Roy *Science* **279**(5354), pp. 1198–1200, 1998.

[160] G. D. VanWiggeren and R. Roy *Phys. Rev. Lett.* **81**, p. 3547, 1998.

[161] R. Lang and K. Kobayashi *IEEE J. of Quant. Electron.* **16**, pp. 347–355, 1980.

[162] R. Vicente, T. Pérez, and C. R. Mirasso *IEEE J. of Quant. Electron.* **38**, p. 1197, 2002.

[163] J. K. White and J. V. Moloney *Phys. Rev. A* **59**, pp. 2422–2426, Mar 1999.

[164] V. Annovazzi-Lodi, S. Donati, and A. Scire *Quantum Electronics, IEEE Journal of* **32**, pp. 953–959, Jun 1996.

[165] V. Annovazzi-Lodi, S. Donati, and A. Scire *Quantum Electronics, IEEE Journal of* **33**, pp. 1449–1454, Sep 1997.

[166] C. Mirasso, J. Mulet, and C. Masoller *Photonics Technology Letters, IEEE* **14**, pp. 456–458, Apr 2002.

[167] A. Sanchez-Diaz, C. Mirasso, P. Colet, and P. Garcia-Fernandez *Quantum Electronics, IEEE Journal of* **35**, pp. 292–297, Mar 1999.

[168] S. Sivaprakasam and K. A. Shore *Opt. Lett.* **24**, p. 1200, 1999.

[169] J. Ohtsubo *Quantum Electronics, IEEE Journal of* **38**, pp. 1141–1154, Sep 2002.

[170] C. Sulem and P. L. Sulem, *The Nonlinear Schrödinger Equation*, Springer, New York, 1999.

[171] W. J. Firth, A. Lord, and A. J. Scroggie *Physica Scripta* **67**, p. 12, 1996.

[172] J. J. Rasmussen and K. Rypdal *Phys. Scr.* **33**, p. 481, 1986.

[173] D. Gomila and P. Colet *Phys. Rev. A* **68**, p. 011801(R), 2003.

[174] D. Gomila and P. Colet *Phys. Rev. E* **76**, p. 016217, 2007.

[175] P. D. Woods and A. R. Champneys *Physica D* **129**, p. 147, 1999.

[176] T. Maggipinto, M. Brambilla, G. K. Harkness, and W. J. Firth *Phys. Rev. E* **62**, p. 8726, 2000.

[177] B. Schäpers, M. Feldmann, T. Ackemann, and W. Lange *Phys. Rev. Lett.* **85**, p. 784, 2000.

[178] B. Schäpers, T. Ackemann, and W. Lange *Proc. SPIE* (4271), p. 130, 2001.

[179] A. Schreiber, B. Thüering, M. Kreuzer, and T. Tschudi *Opt. Comm.* **136**, p. 415, 1997.

[180] V. B. Taranenko, I. Ganne, R. J. Kuszelewicz, and C. O. Weiss *Phys. Rev. A* **61**, p. 063818, 2000.

[181] D. V. Skryabin *J. Opt. Soc. Am. B* **19**, p. 529, 2002.

[182] D. Gomila, M. A. Matías, and P. Colet *Phys. Rev. Lett.* **94**, p. 063905, 2005.

[183] D. Gomila, A. Jacobo, M. A. Matías, and P. Colet *Phys. Rev. E* **75**, p. 026217, 2007.

[184] P. Gaspard *J. Phys. Chem.* **94**, pp. 1–3, 1990.

[185] A. S. Pikovsky and J. Kurths *Phys. Rev. Lett.* **78**, pp. 775–778, 1997.

[186] H. Gang, T. Ditzinger, C. Z. Ning, and H. Haken *Phys. Rev. Lett.* **71**, pp. 807–810, 1993.

[187] T. Ditzinger, C. Z. Ning, and G. Hu *Phys. Rev. E* **50**, pp. 3508–3516, 1994.

[188] B. Lindner, J. García-Ojalvo, A. Neiman, and L. Schimansky-Geier *Phys. Rep.* **392**, pp. 321–424, 2004.

[189] P. Coullet, D. Daboussy, and J. R. Tredicce *Phys. Rev. E* **58**, pp. 5347–5350, 1998.

[190] D. Goulding, S. P. Hegarty, O. Rasskazov, S. M. M. Hartnett, G. Greene, J. G. McInerney, D. Rachinskii, and G. Huyet *Phys. Rev. Lett.* **98**, p. 153903, 2007.

[191] T. Poston and I. Stewart, *Catastrophe Theory and its Applications*, Longman, Essex, 1979.

[192] E. Meca, I. Mercader, O. Batiste, and L. Ramírez-Piscina *Theor. Comput. Fluid. Dyn.* **18**, p. 231, 2004.

[193] F. Dumortier, R. Roussarie, J. Sotomayor, and H. Zoladek, *Bifurcations of Planar Vector Fields. Nilpotent Singularities and Abelian Integrals*, vol. 1480 of *Lecture Notes in Mathematics*, Springer-Verlag, Berlin, 1991.

[194] O. Steinbock, A. Tóth, and K. Showalter *Science* **267**, pp. 868–871, 1995.

[195] L. Kuhnert, K. I. Agladze, and V. I. Krinsky *Nature* **337**, pp. 244–247, 1989.

[196] A. Toth and K. Showalter *J. Chem. Phys.* **103**, pp. 2058–2066, 1995.

[197] O. Steinbock, P. Kettunen, and K. Showalter *J. Phys. Chem.* **100**, pp. 18970–18975, 1996.

[198] J. Gorecka and J. Gorecki *J. Chem. Phys.* **124**, p. 084101, 2006.

[199] C. Koch, *Biophysics of Computation*, Oxford U.P., Oxford, 1999.

[200] W. S. McCulloch and W. H. Pitts *Bull. Math. Biophys.* **5**, pp. 115–133, 1943.

[201] D. J. Amit, *Modeling brain function*, Cambridge U.P., Cambridge, 1989.

[202] E. J. Lerner *Laser Focus World* **1**, pp. 99–102, 2000.

[203] P. L. Ramazza, E. Benkler, U. Bortolozzo, S. Boccaletti, S. Ducci, and F. T. Arecchi *Phys. Rev. E* **65**, p. 066204, Jun 2002.

[204] P. L. Ramazza, U. Bortolozzo, S. Boccaletti, and F. T. Arecchi *Appl. Phys. B* **81**, p. 921, 2005.

[205] D. Foster, *Hydrodynamic Fluctuations, Broken Symmetry and Correlation Fluctuations*, Addison-Wesley, Redwood City, CA, 1983.

[206] U. Frisch, Z. S. She, and O. Thual *J. Fluid. Mech.* **168**, p. 221, 1986.

[207] W. H. Press, W. T. Vetterling, S. A. Teukolsky, and B. P. Flannery, *Numerical Recipes in Fortran*, Cambridge University Press, 1992.

[208] J. M. McSloy, W. J. Firth, G. K. Harkness, and G. L. Oppo *Phys. Rev. E* **66**, p. 046606, 2002.

[209] L. N. Trefethen, *Spectral Methods in Matlab*, SIAM, Philadelphia, 2000.

[210] V. Hernandez, J. E. Roman, and V. Vidal *ACM Trans. Math. Softw.* **31**(3), p. 351, 2005.

[211] S. Balay, K. Buschelman, W. D. Gropp, D. Kaushik, M. G. Knepley, L. C. McInnes, B. F. Smith, and H. Zhang, "PETSc Web page," 2001. http://www.mcs.anl.gov/petsc.

[212] S. Balay, W. D. Gropp, L. C. McInnes, and B. F. Smith, "Efficient management of parallelism in object oriented numerical software libraries," in *Modern Software Tools in Scientific Computing*, E. Arge, A. M. Bruaset, and H. P. Langtangen, eds., pp. 163–202, Birkhäuser Press, 1997.

"Technology is dominated by two types of people: those who understand what they do not manage, and those who manage what they do not understand." — Archibald Putt